INVESTIGATION OF THE NEAR SURFACE MECHANICAL PROPERTIES OF Au-Si THIN FILMS

By

BENJAMIN MICHAEL DVORAK

Bachelor of Science in Mechanical Engineering
Oklahoma State University
Stillwater, Oklahoma
2006

Submitted to the Faculty of the
Graduate College of the
Oklahoma State University
in partial fulfillment of
the requirements for
the Degree of
MASTER OF SCIENCE
July, 2008

COPYRIGHT

By

BENJAMIN MICHAEL DVORAK

July, 2008

INVESTIGATION OF THE NEAR SURFACE MECHANICAL PROPERTIES OF Au-Si THIN FILMS

Thesis Approved:

Don A. Lucca

Thesis Adviser

C. Eric Price

Committee Member

Honbing Lu

Committee Member

A. Gordon Emslie

Dean of the Graduate College

ACKNOWLEDGMENTS

I would like to thank my adviser Prof. D.A. Lucca, for his guidance, support, patience and for giving me the opportunity to conduct research in the Ultraprecision Surfaces Group. I would also like to thank my committee members, Prof. C.E. Price and Prof. H. Lu for taking the time to provide me with comments and suggestions. A special thank you is extended to Prof. D. Coker for his encouragement, mentoring and friendship. I would also like to thank Prof. A. Apblett for performing the XRD measurements and Prof. D. Grischkowsky for allowing the use of his four-point probe instrument. I extend my thanks to Dr. M. Nastasi of Los Alamos National Laboratory for his involvement with this work and express my appreciation to his colleagues, Mr. J.K. Baldwin for preparation of the Au-Si and Au films, Dr. A. Misra and his staff for performing the TEM measurements, Dr. J.K. Lee for performing the RBS measurements, and Dr. I. Usov for his comments and suggestions. I would like to thank Prof. A. Slocum and his students, particularly Dr. A. Weber, at the Massachusetts Institute of Technology for collaborating on this work and providing the Au films. I would also like to thank my colleagues Ms. G. Bassiri, Dr. R. Ghisleni, Mr. T. Harriman, Dr. M. Klopfstein and Mr. V. Doan for their help and support.

Most importantly, I would like to thank my wife and best friend Gena, for her love, patience, support, encouragement and for her understanding of the long hours and difficult schedule. I would also like to thank my parents, brother, my wife's family and the rest of my extended family for all of their love, support and encouragement.

This work is dedicated to my Father in Heaven, His Son, my Lord and Savior, Jesus Christ and the Holy Spirit. While I may be given the credit for this accomplishment, they receive the glory.

This material is based upon work supported by the National Science Foundation under Grant No. 0521989. Any opinions, findings, and conclusions or recommendations expressed in this material are those of the author and do not necessarily reflect the views of the National Science Foundation.

This work was performed, in part, at the Center for Integrated Nanotechnologies, a U.S. Department of Energy, Office of Basic Energy Sciences user facility at Los Alamos National Laboratory (Contract DE-AC52-06NA25396) and Sandia National Laboratories (Contract DE-AC04-94AL85000).

TABLE OF CONTENTS

1 Introduction **1**

1.1 Motivation 1

1.2 Objective 1

1.3 Research plan 2

2 Background **3**

2.1 Selected studies utilizing Au thin films 3

2.2 Improving Au film properties 5

2.2.1 Ion implantation and ion irradiation of Au films 5

2.2.2 The modification of Au films through the addition of alloying elements 9

2.2.3 Precipitation hardening of thin films 10

2.3 Dispersion hardening 12

2.3.1 Dislocation/particle interaction 12

2.3.2 Orowan strengthening 13

2.4 Hardening by reduction in grain size 16

2.5 Nanoindentation 16

2.5.1 Analysis of experimental data 16

2.6 Four-Point Probe 18

3 Experimental **20**

3.1 Specimen preparation 20

3.2 Nanoindentation and Atomic Force Microscopy 21

3.3 Four-Point Probe 23

3.4 Supporting characterization techniques 24

3.4.1 Transmission Electron Microscopy 24

3.4.2 X-ray Diffraction 25

4 Results and Discussion **28**

4.1 Polycrystalline Au film baseline studies 28

4.1.1 Variable deposition rate 28

4.1.2 The effect of the adhesion layer and heat treatment 31

4.2 Au-Si films 38

4.2.1 Initial shakedown experiments investigating the effect of Si addition and heat treatment 38

4.2.2 The effect of Si addition 42

5 Conclusions and Proposed Future Work **63**

5.1 Conclusions 63

5.2 Proposed Future Work 66

Bibliography **68**

A Procedure for measuring the surface topography using the Atomic Force Microscope **81**

A.1 Instrument and software set-up 81

A.1.1 SPM parameters 82

A.1.2 Initial scan parameters 82

A.1.3 Installing the cantilever, cantilever holder and AFM head 82

A.1.4 Aligning the laser 86

A.1.5 Specimen placement 87

A.1.6 Locating the tip in the Vision System 87

A.1.7 Focusing on the specimen surface 87

A.1.8 Auto tuning the cantilever 87

A.2 Performing a surface scan 88

A.3 Analyzing the AFM image 88

B Procedure for measuring the mechanical properties by Nanoindentation **90**

B.1 Background 90

B.2 Instrument and software set-up - Interfacing the TriboScope with the AFM system . 92

B.2.1 SPM parameters 92

B.2.2 Initial scan parameters 93

B.2.3 Cleaning and installing the indenter tip 93

B.2.4 Installing transducer and TriboScanner 95
B.2.5 Locating the indenter tip in the Vision System 96
B.2.6 Specimen placement 96
B.2.7 Manual approach 97
B.2.8 Thermal equilibration 97
B.3 Instrument and software set-up - Hysitron system 97
B.4 Performing the indentation 99
B.4.1 The air-indent 99
B.4.2 The preliminary surface scan 99
B.4.3 The indentation 100
B.4.4 Analysis of the results 100

C Procedure for measuring the thin film resistivity using the Four-Point Probe method 102

C.1 Initial setup 102
C.2 Performing the measurement 103

LIST OF TABLES

4.1 Average roughness values for pure Au films evaporated at varying deposition rates. . 29
4.2 Average roughness values for as-deposited and annealed pure Au films deposited on Ti or Cr adhesion layers. 32
4.3 Average resistivity values for as-deposited and heat treated pure Au films deposited on Ti or Cr adhesion layers. 38
4.4 Average roughness values for the pure Au and as-deposited and annealed Au-Si films. 41
4.5 Average roughness values for pure Au films and Au films co-evaporated with 2.5, 6, 13 or 21 at. % Si. 45
4.6 Average resistivity values for the pure Au and Au-Si films consisting of Au co-evaporated with 2.5, 6, 13, or 21 at. % of Si. 50
4.7 Comparison of the measured d-spacings for the Au/21 at. % Si film with those reported in the literature for a fcc β-Mn-type structure. 57

A.1 SPM parameters panel 82
A.2 Scan Controls panel 83
A.3 Feedback Controls panel 83
A.4 Other Controls panel 84
A.5 Channel 1 panel 84
A.6 Drive Feedback Controls panel 84

B.1 SPM parameters for proper nanoindenter operation 92
B.2 Scan Controls panel 93
B.3 Feedback Controls panel 93
B.4 Other Controls panel 94
B.5 Channel 1 panel 94
B.6 1-D transducer constants 98

LIST OF FIGURES

2.1 Schematic showing a dislocation interacting with a line of particles. 13

2.2 The various steps (1-5) of a dislocation line interacting with two particles due to an applied stress. 15

2.3 (a) Schematic of indenter and sample surface geometry for a Berkovich indenter. (b) Load versus displacement curve for the full loading and unloading. 17

2.4 Standard and alternate instrument layout for sheet resistance measurement using the four-point probe method. 19

3.1 Load pattern used for all indentation experiments. 22

3.2 Typical load-displacement curve for the load pattern shown in Figure 3.1, obtained for the Au/2 at. % Si film. 22

3.3 Load-displacement plot showing an example of the repeatability for 5 measurements conducted at a given load. 23

3.4 Schematic showing the main setup of the x-ray diffractometer for performing the $\theta-2\theta$ scan with the specimen mounted in a reflection geometry. 25

3.5 Schematic showing the diffraction of an incident x-ray beam with the upper two crystal lattice planes separated by an interplanar distance d. 26

4.1 AFM image (1 μm x 1 μm scan size) showing the topography of Au films deposited at a deposition rates of (a) 1.5 Å/s, (b) 3 Å/s, and (c) 4.5 Å/s. 29

4.2 Image of the profile of an indentation, conducted on the pure Au film deposited at 1.5 Å/s at a normalized contact depth of about 0.10, showing the lack of material pile-up. 30

4.3 The effect of deposition rate on the hardness of Au thin films. 31

4.4 The effect of deposition rate on the elastic modulus of Au thin films. 32

4.5 AFM images (1 μm x 1 μm scan size) showing the topography of (a) as-deposited and (b) annealed Au films deposited with Ti adhesion layers. 33

4.6 AFM images (1 μm x 1 μm scan size) showing the topography of (a) as-deposited and (b) annealed Au films deposited with Cr adhesion layers. 33

4.7 AFM image (10 μm x 10 μm scan size) showing cracks present on the surface of the annealed Au film deposited with a Cr adhesion layers. 34

4.8 Load versus displacement curve for the as-deposited Au film with a Cr adhesion layer. A pop-in event was observed at a load of about 20 μN. 35

4.9 Load versus displacement curve for the annealed Au film with a Ti adhesion layer. A pop-in event was observed at a load of about 20 μN. 36

4.10 The effect of heat treatment and adhesion layer on the hardness of Au thin films. . . 36

4.11 Evidence of the indentation size effect in annealed Au films with an underlying Cr adhesion layer. 37

4.12 The effect of heat treatment and adhesion layer on the elastic modulus of Au thin films. 37

4.13 AFM images (1 μm x 1 μm scan size) showing the topography of (a) as-deposited and (b) annealed Au films co-evaporated with 5 at. % Si. 39

4.14 AFM images (1 μm x 1 μm scan size) showing the topography of (a) as-deposited and (b) annealed Au films co-evaporated with 15 at. % Si. 39

4.15 AFM images (1 μm x 1 μm scan size) showing the topography of (a) as-deposited and (b) annealed Au films co-evaporated with 25 at. % Si. 40

4.16 AFM images (1 μm x 1 μm scan size) showing the topography of (a) pure Au and (b) Au co-evaporated with 2 at. % Si. 40

4.17 Optical images showing the overall surface roughness and contamination on the surface of the (a) Au/25 at. % Si and (b) Au/2 at. % Si films. AFM scans indicated that the asperities on the surface of the Au/2 at. % Si film had heights on the order of 2 - 3 μm. 42

4.18 The effect of Si content and heat treatment on the hardness of pure Au and Au-Si films. 43

4.19 The effect of Si content and heat treatment on the reduced elastic modulus of pure Au and Au-Si films. 43

4.20 AFM images (1 μm x 1 μm scan size) showing the topography of (a) the pure Au and Au films co-evaporated with (b) 2.5 at. % Si, (c) 6 at. % Si, (d) 13 at. % Si and (e) 21 at. % Si. 44

4.21 Image of the profile of an indentation, conducted on the Au/6 at. % Si film at a normalized contact depth of about 0.10, showing some material pile-up. 45

4.22 The effect of Si content on the hardness of pure Au and Au-Si films. Shown for comparison are the upper and lower bound rule of mixture predictions obtained from Eqns. (4.1) through (4.4). 47
4.23 The effect of Si content on the reduced elastic modulus of pure Au and Au-Si films. Shown for comparison are the upper and lower bound rule of mixture predictions (upper and lower bound overlap) obtained from Eqns. (4.1) through (4.4). 48
4.24 Comparison of the hardness of the contaminated versus non-contaminated pure Au and Au-Si films. 48
4.25 Comparison of the reduced elastic modulus of the contaminated versus non-contaminated pure Au and Au-Si films. 49
4.26 Optical image showing "telephone cord" buckling of the Au/13 at. % Si thin film. The line at the center of each "telephone cord" buckle is the apex of the delamination. 49
4.27 The effect of Si content on the resistivity of Au thin films. 51
4.28 X-ray diffraction pattern for the pure Au thin film. 51
4.29 X-ray diffraction pattern for the Au thin film co-evaporated with 2.5 at. % Si. 52
4.30 X-ray diffraction pattern for the Au thin film co-evaporated with 6 at. % Si. 52
4.31 X-ray diffraction pattern for the Au thin film co-evaporated with 13 at. % Si. 53
4.32 X-ray diffraction pattern for the Au thin film co-evaporated with 21 at. % Si. 53
4.33 Variation of Au peak intensity ratio, $I_{(111)}/I_{(200)}$ with Si content. 54
4.34 Schematic showing atom transport, in polycrystalline FCC films, occurring across a grain boundary from a (111) grain to a (200) grain resulting from a large compressive stress gradient. 55
4.35 X-ray diffraction pattern for the Au thin film co-evaporated with 21 at. % Si, measured after storing the specimen for approximately 8 weeks at RT. 58
4.36 Optical images showing changes in the surface topography including: (a) the presence of numerous craters on the surface and (b) film delamination occurring at the edges of the craters of the Au thin film co-evaporated with 21 at. % Si, obtained after approximately 10 and 14 weeks of RT storage, respectively. 59

4.37 Selected TEM images showing the microstructure of the Au-Si film with a nominal Si concentration of 25 at. %. (a) TEM image showing the nanocrystalline grain structure of the Au with approximately 1 - 5 nm diameter Si particles located at the Au grain boundaries. (b) High-Resolution TEM (HRTEM) image showing a 3 nm Si particle at the grain boundary of two (111) oriented Au grains. (c) Selected area diffraction pattern showing multiple Au grain orientations. 61

A.1 Schematic of the AFM cantilever holder. 85

A.2 Schematic of the AFM cantilever holder stand. 85

A.3 Top-view of the AFM scanner head showing the location of the laser control knobs. . 86

A.4 Side-view of the AFM scanner head showing the location of the detector mirror adjustment knobs. 86

B.1 Schematic cross-section of the 1-D three place capacitive transducer. 91

B.2 Schematic of the front panel of the nanoindenter transducer controller. 96

C.1 Schematic showing the proper placement of the platen adjustment tool. 103

NOMENCLATURE

AFM .... Atomic Force Microscopy
bcc .... Body-Centered Cubic
CINT .... Center for Integrated Nanotechnologies
EDS .... Energy Dispersive Spectrometry
fcc .... Face-Centered Cubic
HRTEM .... High-Resolution Transmission Electron Microscopy
ICDD .... International Centre for Diffraction Data
IDA .... Indentation Data Analyzer
ISO .... International Organization for Standardization
JCPDS .... Joint Committee on Powder Diffraction Standards
l.b. .... Lower Bound
LANL .... Los Alamos National Laboratory
LCD .... Liquid Crystal Display
LED .... Light Emitting Diode
MEMS .... Microelectromechanical Systems
MIT .... Massachusetts Institute of Technology
PDF .... Powder Diffraction File
PGRM .... Program
PIXE .... Particle Induced X-ray Emission
RBS .... Rutherford Backscattering Spectroscopy
RT .... Room Temperature
SEM .... Scanning Electron Microscopy
SPM .... Scanning Probe Microscopy
STM .... Scanning Tunneling Microscopy
TEM .... Transmission Electron Microscopy
TESP .... TappingMode Etched Silicon Probes
u.b. .... Upper Bound

UHV .... Ultra-High Vacuum

XPS .... X-ray Photoelectron Spectroscopy

XRD .... X-ray Diffraction

XTEM .... Cross-Sectional Transmission Electron Microscopy

α .... Thermal Coefficient of Expansion, $^{\circ}C^{-1}$

θ .... Angle of the Incident X-ray Beam and the Specimen, Degrees

λ .... Particle Separation Distance, nm

λ .... Wavelength, nm

ν .... Poisson's Ratio, non-dimensional

ρ .... Resistivity, $\mu\Omega$-cm

σ_i .... Friction Stress, GPa

σ_{Orowan} .... Yield strength as determined by the Orowan mechanism, GPa

σ_0 .... Yield Stress, GPa

$\Delta\sigma^{(hkl)}$ .... Stress in Grain Oriented in (hkl) Plane, MPa

τ .... Shear Stress, GPa

$\bar{\tau}$ .... Average Shear Stress, GPa

ϕ .... Breaking Angle, Degrees

A .... Projected Area, nm^2

a .... Lattice Parameter, nm

b .... Burgers vector, nm

C .... Constant, non-dimensional

D .... Grain Diameter, nm

d .... Interplanar Spacing

E .... Elastic Modulus, GPa

E_{hkl} .... Elastic Modulus in the (hkl) Plane, GPa

E_r .... Reduced Elastic Modulus, GPa

E_r' .... Reduced Elastic Modulus of Au-Si Film (Rule of Mixtures), GPa

$(E_r)_{Au}$ .... Reduced Elastic Modulus of Pure Au Film, GPa

$(E_r)_{Si}$ .... Reduced Elastic Modulus of Single Crystal Si, GPa

F .... Obstacle Strength, N

F_c .... Contact Force, N

G .... Shear Modulus,GPa

H .... Hardness, GPa

H' .... Hardness of the Au-Si Film (Rule of Mixtures), GPa

H_{Au} .... Hardness of Pure Au Film, GPa

H_{Orowan} .... Hardness increase resulting from the Orowan mechanism, GPa

H_{Si} .... Hardness of Single Crystal Si, GPa

h_c .... Contact Depth, nm

h_e .... Displacement due to elastic deformation of the surface, nm

h_f .... Final impression depth when the indenter is completely withdrawn, nm

h_s .... Surface displacement at the outer contacting edge of the indenter, nm

h_t .... Maximum displacement at peak load, nm

(hkl) .... Miller Index, non-dimensional

I .... Current, A

$I_{(111)}/I_{(200)}$ .... Intensity Ratio, non-dimensional

k .... Locking Parameter, non-dimensional

n .... Order of Diffraction (XRD), non-dimensional

n .... Total Points (Surface Roughness), non-dimensional

P_{max} .... Maximum Load, μN

R .... Radius of Curvature, nm

r .... Spherical Particle Radius, nm

Ra .... Arithmetic Mean Surface Roughness, nm

Rc .... Electrical Contact Resistance, Ω

Rq .... Root-mean Square Average Surface Roughness, nm

R_s .... Sheet Resistance, Ω or Ω/square

Rz .... Peak-to-Valley Surface Roughness, nm

S .... Contact Stiffness, μN/nm

S_{ij} .... Elastic Compliance, 10^{-11} Pa

T .... Dislocation Line Tension, N

t .... Film Thickness, cm or nm

U .... Strain Energy, GPa

V .... Voltage, V

V_{Au} .... Volume Fraction of Au, non-dimensional

V_{Si} .... Volume Fraction of Si, non-dimensional

y .... Absolute Surface Height, nm

Chapter 1

Introduction

1.1 Motivation

Two important areas of research and science which have directly benefited from the use of thin films, and specifically metallic films, are Microelectromechanical Systems (MEMS) and MEMS-based electrical contacts. Metals such as Au, Ag, Pt and Rh are often deposited onto the MEMS structures and offer great benefits in terms of increased electrical conductivity and mechanical reliability. However, little has been reported on how the nanomechanical properties of these contact films affect the mechanical degradation and electrical performance of these devices. By obtaining an understanding of the mechanical, structural and electrical properties of thin films, the optimum material can be chosen and efforts focused toward improving the properties of the material in order to create a system which utilizes the ideal combination of electrical and mechanical properties critical to a high level of device performance.

1.2 Objective

The objective of this work is to investigate the modification of pure Au films so as to examine how the material properties can be altered through the development of an Au-Si film. The strengthening mechanisms resulting from the modification of the Au films will be examined as well as the effect of the surface and subsurface material structure and properties on the mechanical and electrical properties of pure Au and Au-Si thin films.

1.3 Research plan

This work is a part of a collaboration between research groups at Oklahoma State University (OSU), Massachusetts Institute of Technology (MIT) and the Center for Integrated Nanotechnologies (CINT) at Los Alamos National Laboratory (LANL) aimed at investigating high-performance electrical contacts and the modification of thin film contacts for MEMS devices.

In this work, an investigation of a basic pure Au system was carried out to first examine the effects of deposition rate, heat treatment and different adhesion layers on the film properties. Then, an experimental study was completed to investigate the modification of pure Au films by the introduction of Si so as to examine the changes in hardness, surface topography and resistivity on the resulting film.

Atomic Force Microscopy (AFM), nanoindentation and four-point probe were utilized to investigate the surface topography, mechanical properties and resistivity of these films, respectively. Furthermore, X-ray Diffraction (XRD) and Transmission Electron Microscopy (TEM) measurements were performed to investigate the material crystallography and structure.

Chapter 2

Background

The subject of thin metallic film research is an exciting area of science and technology which impacts a broad range of industries and disciplines. A thin film can be characterized simply as a thin layer of material, generally with a thickness of less than 1 μm. The interesting aspect of thin film science is that it has existed as far back as 4,000 years ago to the Egyptians who used gold (Au) hammered into thin films, some of which were only 300 nm in thickness, to adorn statues, coffins and royal crowns. Today skilled craftsmen can create gold leaf with thicknesses of 100 - 500 nm and it can be seen adding decorative touches to a wide range of items such as picture frames, furniture, custom motorcycles and even chocolate. Gold leaf was one of the first metallic samples studied by Transmission Electron Microscopy (TEM) [1, 2].

Today thin films play a critical role in many high technology industries and scientific disciplines. The use of thin films can be seen in applications such as microelectronics, optics and general high performance coatings.

2.1 Selected studies utilizing Au thin films

MEMS switches utilizing metallic contacts often incorporate Au as a thin film contact material due to its enhanced properties such as improved electrical conductivity, low resistivity and contact resistance, corrosion resistance and ductility [3–7].

Numerous studies have been conducted on Au thin films and due to its prevalent use in MEMS applications this section will focus on research that has been carried out on Au films used in electrical contacts. Specific areas of focus in the literature have been wear [8], electrical properties such as contact resistance [4,5,9–15] and resistivity [6], adhesion [5,10,12,15,16], thermal effects [11], contact

failure [5, 11, 17] and mechanical properties [6, 14, 18–22].

When Au began to be incorporated as an electrical contact film, early studies focused primarily on characterization of the electrical performance and robustness of the films during simulated operation. One of the key issues in electrical contacts is obtaining a desirable relationship between the contact force necessary for stable resistance and the lift-off force necessary to overcome any adhesion between the contacts [10]. One of the earliest relevant studies in this area was conducted by Schimkat in 1998 [10]. Schimkat investigated the effects of contact forces in the range of 0.1 - 10 mN, on the stability and adhesion of Au, Au-Ni alloy and Rh contact rivets. Very high and unstable resistances were observed when the initial contact was established and very low contact forces were present. A minimum force was necessary to obtain a significant reduction in the resistance and the contact became stable as the force was increased. Similar trends in contact resistance and force were later reported by Hyman and Mehregany [23]. Au was found to have the smallest minimum contact force at 0.1 mN, at which stable contact was established and the resistance was less than 1 Ω. The contact resistance R_c was also measured and found to relate to the contact force F_c by the relationship $R_c \sim F_c^{-\frac{1}{3}}$, which for Au was less than 30 mΩ. Schimkat also noted that in order for the contact to be reliable, a lift-off force must be applied which exceeds the force generated due to adhesion between the two contacting surfaces. However, Au was found to have the highest lift-off force at 2.7 mN compared with 0.3 mN for the Au-Ni alloy [10].

Consistent with the work by Schimkat, most electrical contact research up to the end of the 20th century was mainly focused on establishment of the contact instead of the extended operation and reliability [24]. A later study by Hyman and Mehregany [23], conducted on Au-plated Si substrates in contact with Au-plated W probes, confirmed that the contact resistance is very high at low loads and decreases and stabilizes as the force is increased. Contact resistances for Au films were found to be between 70 - 120 mΩ for contact forces of 100 - 500 μN, respectively. It was also reported that the electroplated Au, with a hardness of about 1 GPa, had annealed and softened causing Au material transfer to the harder, sputtered Au anode, which had a hardness of about 3 GPa. In addition to showing evidence for greater performance in contacts with harder deposited Au films , it was hypothesized that the temperature at which the films annealed and softened could be related to the deposition temperature. Hyman and Mehregany reported that annealing and softening occurred for contact films subjected to temperatures greater than their deposition temperatures during contact cycling. The sputtered Au film, deposited at a higher temperature than the electroplated Au, was not expected to anneal and soften until operation temperatures exceeded the deposition temperature [23]. This would imply that electrical contacts containing Au films deposited by electron-beam evaporation

(minimum evaporation temperature of 1132 °C [2]), such as those investigated in the present study, would be able to withstand higher operation temperatures.

Although Au is often chosen due to its superior electrical properties, electrical contacts incorporating Au often experience failure as the soft Au deforms and causes the metal contact switches to adhere to one another and remain stuck closed [4]. Additionally, the low hardness (1 - 2.3 GPa for Au films previously reported in the literature [14, 21, 22]) and ductility of the Au films, leads to deformation at the contact area of the two switch surfaces, which causes an increase in the contact area and an initial reduction in contact resistance [14]. Besides causing device failure through stiction between the contacts, the junctions of adhesion between the Au contacting asperities, also known as microwelds, can shear leading to material transfer occurring between the contacts [17, 25]. This can immediately lead to device failure, or the small microwelds can also break off forming wear fragments which can further damage the surfaces [17, 25] and lead to poor electrical performance.

The next section presents some of the methods which have been used to modify and improve the material properties in Au and other thin film systems.

2.2 Improving Au film properties

Thin film modification techniques such as ion implantation, ion irradiation, the addition of various alloying elements and precipitation hardening have all been seen to be an effective means to obtain desired material properties. These methods allow the material to be tailored to individual needs and adjusted to meet various applications. The use of thin film modification techniques in Au thin film systems is presented below.

2.2.1 Ion implantation and ion irradiation of Au films

Ion implantation and ion irradiation involve creating a charged particle from an ion source and directing and accelerating a focused beam of the ions onto the surface to be modified. The accelerated ions dissipate energy by interacting with the target material. Defects are produced in the target material, as a result of the ion-solid interaction as well as the presence of the implanted ions, generating changes to the specimen's microstructure and leading to changes in the material's properties [26, 27].

A large portion of reported work has been on studies of N implanted Au films, however the use of other ion species has been investigated as well. One such early study was conducted by Robic et al. [28] in which Au films evaporated onto Si substrates were implanted with He^+, Ne^+, Ar^+, B^+, and Al^+ ions at energies of 100 - 200 keV and fluences of 3 x 10^{17} ions/cm^2. In this study, which

appears to be one of the earliest focused on altering the material properties of Au by implantation, the properties of the film including hardness, residual stress and wear were measured to understand the effects of implantation. Knoop microhardness measurements of the films revealed a 35% relative hardness increase in the Au films after implantation with B^+ or Ne^+ ions at high fluences. With the exception of work focused on N implantation of Au films, there appears to have been little other work involved with investigating the change in mechanical properties (such as hardness) as a result of implantation.

Recently, ion implantation has been used to reduce the curvature in metallized MEMS cantilever beams [29] and optical mirror devices [30]. In a study by Jin et al. [30], MEMS optical mirrors with deposited Au films were implanted with 20 - 40 keV Si^+ ions at fluences of 0.4-5 x 10^{16} ions/cm^2. It was reported that as the fluence was increased to about 0.8 x 10^{16} ions/cm^2 the metallized mirrors lost their initial curvature and became nearly flat. This was attributed to the increased compressive stress in the Au film, brought on by the introduction of the implantation species into the lattice structure of the Au. These compressive stresses induced by the implantation reduced the specimen curvature by counterbalancing the tensile stresses present in the specimens after the initial metallization. In a similar study by Kang et al. [29], MEMS microcantilever beams with deposited Au films were implanted with He^+ and N_2^+ ions at energies of 40 - 50 keV and fluences of 10^{16} - 10^{17} ions/cm^2 in order to reduce the residual stresses present in the beams leading to unwanted specimen curvature. It was found that after implantation, the residual stresses in the films were reduced by 15 - 62% for the fluence range used. Similar to that previously discussed, the reduced curvature was attributed to the induced compressive stress as a result of implantation.

The modification of the electrical properties and surface morphology of Au films as a result of ion implantation has also been investigated. One such study was conducted by Ikeyama et al. in 1994 [31] in which Au films deposited on Pyrex glass or MgO single crystal substrates were implanted with Si^+, Ni^+ and Au^+ ions at energies of 0.75 - 3 MeV and fluences of 5 x 10^{13} - 5 x 10^{16} ions/cm^2. After implantation it was observed that a depression was left on the surface of the film and increased in size with increasing fluence. Scanning Electron Microscopy (SEM) results indicated that the surface became smoother after implantation and also that grain growth occurred. Artunc et al. [32] also showed evidence for grain growth after implanting Au films with 125 keV Cr^+ ions at fluences ranging from 1 x 10^{14} - 5 x 10^{16} ions/cm^2. The structure of the films was characterized by TEM and Rutherford backscattering spectrometry (RBS); electrical measurements were conducted using a standard four-point probe technique. RBS measurements indicated the formation of a Au-Cr alloy at fluences less than 5 x 10^{16} ions/cm^2 and ion induced mixing of both the Au and Cr^+

ion into the substrate at fluences above 5 x 10^{15} ions/cm^2. TEM results indicated that the grain size increased with increasing fluence and electron diffraction patterns indicated the formation of a Au-Cr solid solution. Four-point probe measurements revealed that the resistivity doubled as the fluence was increased from 1 x 10^{14} ions/cm^2 - 1 x 10^{16} ions/cm^2.

N is often used in ion implantation and when it interacts with a material surface the reaction can produce metallic nitrides [33]. The benefits of N implantation of metallic films and the formation of metallic nitrides are widely reported [33–40] and these newly formed metal nitrides are known to be useful for a range of applications, and possess distinctive properties such as high hardness and high melting temperatures, chemical stability and useful electronic properties [38, 40].

N implantation has been utilized in Au and other metals such as Ag, Ti, Ta, Mo, W, Ni, Fe and Cu [37–43]. One of the first reports of N implantation of Au was by Lancaster and Rabalais in 1979 [34] in which Au and several other thin metallic films were implanted with N_2^+ ions at energies ranging from 30 eV - 3 keV. In this work, they were unable to detect any N1s signals in the X-ray Photoelectron Spectroscopy (XPS) measurements and proposed that this was due to either: 1.) not enough N_2^+ implanted to be detected or 2.) the lighter N was being preferentially sputtered rather than the heavier Au atoms (Atomic mass: Au = 196.97 g/mol versus N = 14.007 g/mol). There was also no N observed at low energies such as 50 eV (when sputtering rates are low) and it was proposed that this was most likely due to either low sticking probability or low chemical reactivity.

In a later study, Anttila et al. [33] implanted 16 metals, including Au, with 300 keV N_2^+ ions and observed the resulting N concentration using RBS with a 2 MeV $^4He^+$ ion beam. They also utilized a micro-hardness tester and an optical microscope to observe the mechanical and surface properties. Micro-hardness measurements revealed relative hardness increases of 1.0 for Au, Mo and Ag to as high as 2.3 for Ti. In addition, the surface analysis revealed that blisters due to the N_2^+ implantation formed on many of the metal surfaces. While a N concentration of 18% was observed in Au films, there was no confirmation of the formation of AuN. The failure to form AuN was attributed to the high sputtering yield of the N, leading to a concentration that was too low to react with the target metal. This claim was later argued by Zhou et al. [35] when they proposed that the average N concentration was not a factor in the formation of a metal nitride but aspects such as structural compatibility and compound growth kinetics were most likely the key.

The point made by Zhou et al. that the main influence in the formation of metal nitrides by implantation is chemical compatibility was concluded and expanded further by Sanghera and Sullivan in 1999 [37]. They proposed that two indications of the reactivity and the formation of a metal nitride are: 1.) the difference in the electronegativity between the metal and N and 2.) how negative the heat

of formation of the nitride is. The higher the difference in electronegativity between the metal and N and the more negative the nitride's heat of formation, the greater will be the chemical interaction and driving force for the formation of the nitride. The difficulty of forming AuN could also be due to its chemical inertness or that the N may be isolated to interstitials and then sputtered because of its lighter mass [37].

Reported experimental results have demonstrated that implantation of metallic films with N_2^+ ions can lead to an improvement in the material properties. In studies by Leech et al. [44, 45], N_2^+ ions were implanted into various Au-based alloys and electroplated Pd thin films and the tribological effects were studied. Micro-hardness measurements, utilizing a Knoop diamond indenter, showed that hardness increased by 12 - 13% in the Au-based alloy. Contact resistance measurements revealed a slight overall decrease in resistance of the Au films after implantation. There was also an observed decrease in the coefficient of friction of the implanted films.

The first reported observation of AuN was by Siller et al. in 2002 [38]. In this study, using methods similar to those used in N implantation of Cu, (110) single crystal Au was irradiated with 500 eV and 2 keV N_2^+ ions under ultra-high vacuum (UHV). The AuN formation was confirmed after XPS revealed N1s peaks at a binding energy of about 396.6 eV, which was in the range of peaks observed at 396.5 - 396.8 eV on N implanted (110) Cu. Later studies by the same group [39, 40] reported similar binding energy peaks in the N1s spectra. In a study by Siller et al. in 2005 [40], AuN films were created using both low energy reactive ion sputtering and plasma methods. Nanoindentation measurements indicated that the hardness of the films increased by about 50% compared to unmodified pure Au films. Four point probe measurements indicated that the contact resistance of the films increased 82% from about 4 x 10^{-8} Ω-m to about 1 x 10^{-7} Ω-m. The group proposed that previous work had failed to detect or produce AuN either because the ion energies were too high or the sensitivity of the equipment was insufficient.

The evidence presented from the literature suggests the possibilities of using nitrogen implantation to improve the physical and electrical properties of Au thin films. However, the lack of verification for the production of AuN by means of implantation indicates that producing AuN films is a very difficult process and thus was not pursued in this study.

The majority of studies on the modification of Au thin films by ion irradiation present in the literature utilize Ar^+ [46–52]. These studies have reported that Ar^+ irradiation in Au thin films leads to grain growth [50], increases in resistivity [46], sputtering of Au [46], mixing of Au with the substrate material [47] and the formation of islands on the surface of the film [47, 48], all of which would be detrimental to the performance of an Au coated electrical contact.

Similar to the studies utilizing Ar^+ for irradiation of Au films, those involving Xe^+ ions were principally focused on observing the Au surface morphology after irradiation and have reported crater and hole formation [53, 54], sputtering of Au from the film surface and film erosion [55–57]. Again, surface changes such as these would have adverse effects on the performance of an electrical contact film.

2.2.2 The modification of Au films through the addition of alloying elements

The low hardness of Au leads to increased wear and failure when used as a contact material [4]. One method of improving the hardness of Au films is through the addition of alloying elements such as Pt, Ag, Pd, Rh, Ru, [4,6], Co [58,59], Ni [10,12,59,60] and Cu [61]. Hard Au films consisting of Au alloyed with 0.06 - 0.5 wt. % of either Co or Ni [58] are often deposited, through electroplating, onto microrelays, circuit boards and electrical connectors [60]. Hard Au films typically have hardnesses 2 - 3 times that of soft Au. This increased hardness has been attributed to the reduction in grain size and the Hall-Petch effect [60]. In addition to hardness, the electrical properties must also be acceptable for the films to be used in electrical contact applications. In a study on the contact resistance stability of hard Au thin films, Antler [58] found that Co-hardened Au (Au-Co alloy film) exhibited a higher initial contact resistance than Au (roughly twice that of pure soft Au) due to its increased hardness and resistivity. While Ni-hardened Au (Au-Ni alloy film) had roughly the same increase in contact resistance, it was more thermally stable as the films were aged for up to 1000 hours at 200 °C. Later studies by Schimkat [10, 12] also investigated the electrical properties of Ni-hardened Au and found that the contact resistance of the alloyed films increased from 15 - 60 mΩ while the adherence force (the force required to open the closed contact) was much lower for the Ni-hardened Au film at 0.3 mN compared to 2.7 mN for the pure Au film. A recent study by Togasaki et al. [60] investigated the mechanical and electrical properties of amorphous hard Au. Knoop microhardness experiments indicated that amorphous Au-Ni alloy films possessed hardnesses more than twice that of traditional Au-Co alloy films and more than 5 times the hardness of soft Au films. It was also found that the Au-Ni alloy film had about the same contact resistance of the Co-hardened film (2.21 mΩ and 2.16 mΩ for the amorphous Au-Ni film versus the Au-Co film, respectively).

In addition to the modification of Au films by the addition of Co and Ni alloying elements, there have been studies on Au films alloyed with other elements as well. Similar to the hard Au

film discussed in the previous section, an electroplated Au-Cu alloy was recently investigated by Jankowski et al. [61]. In this study, 10 μm thick films alloyed with 5 wt. % Cu were characterized and found to possess a Vickers microhardness of 2.9 GPa. It was determined that, similar to that reported by Togasaki et al. [60], the reduction in grain size was the dominate mechanism responsible for the film hardening. Additional recent studies have been conducted by Coutu et al. [4] and Lee et al. [6] involving a comparison of several Au alloy films used as electrical contact materials for MEMS switches. In their first study [4], Au films alloyed with either Pt, Pd or Ag at concentrations of 1 - 10 at. %, were developed by co-sputtering both Au and the alloying element onto 3 in. Si wafers. XRD was performed on all films in order to determine the material composition and crystal structure. The electrical properties (contact resistance and resistivity) of the films were determined using the four-point probe method and the mechanical properties were measured using nanoindentation. Of the various alloy films investigated, the Au-Pt thin film with approximately 6% Pt performed the best with a measured hardness and contact resistance of 2.19 GPa and 0.42 Ω, respectively, compared to the pure Au film properties of 1.77 GPa and 0.21 Ω for hardness and contact resistance, respectively. The resistivity increased from 3.93 - 7.17 $\mu\Omega$-cm for the pure Au film versus the Au-6%Pt alloy film, respectively. In the second study by Lee et al. [6], Au films were alloyed with either Pt, Rh or Ru at concentrations of 10 - 70 at. %. They were developed by co-sputtering both Au and the alloying element onto Si wafers. Similar to the previous study, the resistivity was determined using the four-point probe technique and the mechanical properties were determined using nanoindentation. Nanoindentation measurements indicated hardness values, for the 1500 nm thick pure Au, Au-30%Rh, Au-30%Ru, Au-10%Pt, Au-50%Pt films, of 0.81, 3.58, 6.69, 1.47, and 4.58 GPa, respectively. Four-point probe resistivity measurements of the films indicated average values, for the 1500 nm thick pure Au, Au-30%Rh, Au-30%Ru, Au-10%Pt, Au-50%Pt films, of 3.6, 58.8, 83.9, 15.2, and 43.3 $\mu\Omega$-cm, respectively.

2.2.3 Precipitation hardening of thin films

Recently reported studies have shown an increased hardness in films containing uniformly dispersed, immiscible particles. Recently, Radmilovic et al. [62] observed that co-evaporation of Al with up to 23 at. % of Si can increase the Al film hardness by as much as 400% . In their work, evenly dispersed Si nanocrystals with sizes ranging from 10 - 20 nm were observed in Al films co-evaporated with a Si content of 12 at. %. A refined Al grain structure and morphology were observed and attributed to pinning of the grains caused by the Si phase. The improvement in the mechanical properties

was attributed to Hall-Petch strengthening resulting from the refined Al grain structure and also to Orowan strengthening from the Si particles inhibiting dislocation motion.

This increased hardness effect could be further improved by adding Ge along with Si, as discussed by Hornbogen et al. [63], to create an order of magnitude finer dispersion of particles in Al alloy films compared to those with Si alone . Mitlin et al. [64] attributed this effect to counteracting volumetric strains in Al solid solutions leading to a dense distribution of Si-Ge solutes that converted to diamond-cubic form once annealed. They also reported that the Si-Ge precipitates were more equiaxed in addition to being finer than Si precipitates alone . The dense distribution of fine precipitates has been reported to occur only when both Si and Ge are present and the addition of simply Si or Ge results in overly-coarse precipitates [65]. However, the Si-Ge precipitates, while finer than the Si or Ge particles, may still be too coarse to provide improved hardening [64, 66].

Only a few studies have been found which utilize the benefits of precipitation hardening in Au films. Recently, Ramirez and Saha [67] conducted experimental work on compositionally graded Au-Co films with material content ranging from pure Au and increasing Co content up to pure Co. A linear increase in the thin film hardness from 2 - 9 GPa was observed for the pure Au to pure Co. Nelson-Fitzpatrick et al. [68] performed a similar study on Au-Ta thin films prepared by co-sputtering Au and Ta to create pure Au films and Au-Ta films with increasing Ta content up to a pure Ta film. Nanoindentation experiments conducted on the films showed the hardness increased from about 2 GPa for the pure Au film up to about 11.5 GPa by the addition of up to 65 at. % Ta. The increase in hardness was attributed to several mechanisms including grain size reduction, precipitation hardening, the higher intrinsic hardness of the Ta and a phase change occuring in the Ta at concentrations greater than 50 at. %. The grain size ranged from 68 - 30 nm for the pure Au film to the 50 at. % Ta film. It was reported that the observed grain size reduction was due to Ta particles pinning the Au grains and restricting grain growth, similar to that reported by Radmilovic et al. [62].

While precipitate hardening has been shown to be ineffective in sputtered Al-Si and Al-Si-Ge alloys due to coarse precipitates, the previously discussed work by Radmilovic et al. [62] showed evidence that precipitation hardened Al-Si alloys can be effectively prepared using co-evaporation. Additionally, the work by Ramirez and Saha [67] and Nelson-Fitzpatrick et al. [68] indicate that the hardness of Au thin films can be enhanced by the use of precipitation hardening. Also, Al-Ge and Al-Si alloys form simple binary eutectic systems [65] similar to Au-Si alloys providing evidence for the feasibility of incorporating Si or Si-Ge precipitation hardening into Au thin films. Furthermore, Au and Si are known to be almost completely immiscible in the solid state [69] suggesting that

co-deposition of the two would result in the segregation of Si particles within the Au matrix leading to a dispersion hardening mechanism similar to precipitation hardening reported in the previously discussed studies. These prior studies suggest that mechanisms in addition to precipitation or dispersion hardening such as grain size strengthening and the higher hardness of Si (reported to be as high as 13 GPa [70]) could contribute to improving the hardness in Au thin films. These ideas are further explored in the present study.

Some of the basic principles of dispersion hardening and the mechanisms which contribute to hardening in films containing a uniform dispersion of immiscible particles are discussed next.

2.3 Dispersion hardening

Some of the typical methods used to strengthen and modify the material properties of Au thin films have been discussed in the previous section. According to Martin [71], there are four main methods in which the plastic deformation resistance of a metal may be raised: cold work, grain refinement, solid solution strengthening and precipitation hardening. Dispersion hardening could be considered an additional hardening mechanism.

Whereas precipitation hardening is most commonly performed by heating a material and initiating precipitation of second phase particles from a supersaturated solid solution [71], the second phase particles in a dispersion hardened material have very low solubility and are non-coherent with the matrix material [72]. There are three classes that dispersed phases can be classified as: 1.) hardening precipitates which have a size range of 1 - 100 nm; 2.) intermediate-sized dispersoids with a size range of 100 nm - 1 μm; 3.) coarse residual particles with sizes larger than 1 μm [71].

In the present work, improving the mechanical properties of Au thin films by dispersion hardening was pursued. A dispersion hardened material developed through the co-evaporation of two almost completely immiscible materials, Au and Si was investigated. The goal is that the Si will form uniformly dispersed and distributed particles within the polycrystalline Au matrix that will strengthen the material by impeding dislocation motion.

2.3.1 Dislocation/particle interaction

Martin [71] discussed the interaction between a dislocation line and an array of particles. An overview is presented below.

Consider the model shown in Figure 2.1. A dislocation attempting to pass a line of particles, which are separated by a distance λ, is forced to bow out to a radius R, and results in a dislocation

line tension T that is separated by an angle ϕ. The dislocation line tension is directly opposed by the force F, which represents the strength of the particle. When the angle ϕ has reached a critical value, the dislocation line can break past the particle array and continue propagating through the material. At this point, the two forces can be related through the following equation

$$F = 2T \cos \frac{1}{2}\phi \tag{2.1}$$

where the critical angle ϕ is known as the breaking angle and F and T are the previously defined values.

For the case of a particle acting as an impenetrable barrier, the breaking angle goes to zero and Eqn. (2.1) can be simplified to $F = 2T$.

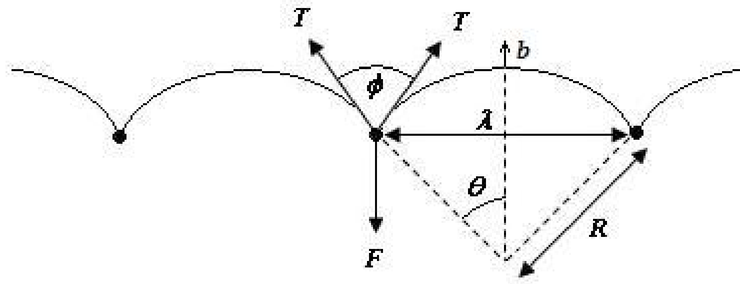

Figure 2.1: Schematic showing a dislocation interacting with a line of particles. After Reference [71].

2.3.2 Orowan strengthening

In 1948, Orowan [73] proposed that the yield stress of a dispersion hardened material can be determined by the shear stress required to bend an approaching dislocation line between two particles with an average separation distance λ, shown in Figure 2.1 [72]. The applied shear stress τ, can be directly related to the dislocation line tension through the following equation

$$\tau = T\frac{b}{R} \tag{2.2}$$

where b is the dislocation Burgers vector and R is the radius of the bowing dislocation. By observing the geometry in Figure 2.1 it can be shown that $\lambda = 2R\sin\theta$ and when substituted into Eqn. (2.2) yields

$$\tau = \frac{2T\sin\theta}{b\lambda} \tag{2.3}$$

Using the relationship $\theta = 90^\circ - 1/2\phi$ and assuming that the breaking angle $\phi = 0$, for an

impenetrable particle, Eqn. (2.3) for the shear stress becomes

$$\tau = \frac{F}{b\lambda} \tag{2.4}$$

As discussed above, as the force F increases due to the increased strength imposed by the unshearable particle, the breaking angle ϕ reaches zero and F becomes equal to twice the dislocation line tension T. Therefore, by substituting this relationship into Eqn. (2.4), the shear stress now becomes

$$\tau = \frac{2T}{b\lambda} \tag{2.5}$$

which gives the critical shear stress required for the dislocation line to pass the particles.

Equation (2.4) can be further re-arranged by assuming that the strain energy of the dislocation can be written as

$$U = \frac{Gb^2}{2} \tag{2.6}$$

where U is the total strain energy, G is the shear modulus of the matrix and b is the Burgers vector of the matrix [72]. The dislocation line tension T is assumed equal to the strain energy U, therefore by substituting Eqn. (2.6) into (2.5) the stress required to move the dislocation line between the particles is [72]

$$\tau = \frac{Gb}{\lambda} \tag{2.7}$$

Figure 2.2 shows the various steps, discussed by Orowan, as the dislocation line approaches, intercepts and passes two particles. Step 1 shows the dislocation line approaching two particles due to an applied stress. At Step 2, the dislocation line begins to bend into the gap between the two particles and continues until a critical curvature has been reached (Step 3). As this stress is reached, the line continues to move past the particles and eventually separates itself from the particle leaving a dislocation line remaining around each particle (Step 4). After Step 4 the dislocation line can continue to move through the material (Step 5) [72, 73].

Once the process described above is complete, if a new dislocation line approaches, the process repeats itself and another dislocation loop is left around the particle. Each subsequent dislocation loop causes an increased shear stress required to pass the next dislocation line past the particles causing the material to strain harden.

The most common expression used to calculate the increase in yield strength of a material, as determined by the Orowan mechanism, is one later modified by Ashby in 1968 [72].

$$\sigma_{Orowan} = \frac{0.13Gb}{\lambda} ln\frac{r}{b} \tag{2.8}$$

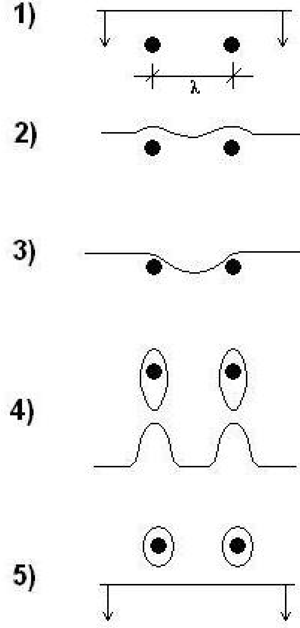

Figure 2.2: The various steps (1-5) of a dislocation line interacting with two particles due to an applied stress. After Reference [72].

where G, b and λ are the previously defined values and r is the average spherical particle radius. To obtain Eqn. (2.8), Ashby made the assumption that the Orowan stress was related to the average stress required to move a dislocation line between an array of particles, $\bar{\tau}$ by [74]

$$\sigma_{Orowan} = (1/1.18)\bar{\tau} \tag{2.9}$$

where the average stress $\bar{\tau}$ represents a modification to Eqn. (2.7), made by assuming a more complicated relationship between the dislocation line tension and the strain energy, given as [74]

$$\bar{\tau} = \frac{Gb}{2\pi\lambda} ln\frac{r}{b} \tag{2.10}$$

Equation (2.8) estimates the increase in yield stress of a material resulting from the presence of a uniform dispersion of non-shearable particles. The hardness of a material can be estimated to be 3 times the yield strength [25] and therefore the hardness increase of the material due to the Orowan mechanism can be determined through the modification of Eqn. (2.8) to obtain

$$H_{Orowan} = 3\sigma_{Orowan} \tag{2.11}$$

where H_{Orowan} is the predicted hardness increase. A similar relationship between the material hardness and the Orowan strength has been reported for Al_2O_3 reinforced Ni films [75].

2.4 Hardening by reduction in grain size

Grain refinement is one of the mechanisms in which the plastic deformation resistance of a metal can be raised [71]. Several studies have been discussed earlier which observed an increase in the thin film hardness as a result of the reduction in grain size [60–62, 68]. Additionally, researchers have reported a restricted grain growth resulting from grain pinning due to the presence of a uniform dispersion of particles [62, 68].

When plastic deformation occurs in a polycrystalline material, dislocation motion is impeded by grain boundaries. Grain boundaries typically impede dislocation motion by either causing the dislocation to alter its direction of motion as it travels from one grain to another at a different orientation or due to a discontinuity of slip planes between the two adjacent grains [76].

A material with a smaller grain size is harder than one with larger grains because the fine-grained material possesses a greater total grain boundary area to act as a barrier to dislocation motion [76]. The Hall-Petch relationship states that the yield stress of a material is inversely proportional to the grain size through the well known equation

$$\sigma_0 = \sigma_i + k\ D^{-1/2} \tag{2.12}$$

where σ_0 is the material's yield stress, σ_i is known as the "friction stress" which represents the overall resistance of the lattice to dislocation motion, k is the "locking parameter" which is a constant that represents the hardening contribution of the grain boundaries and D is the grain diameter [72].

2.5 Nanoindentation

2.5.1 Analysis of experimental data

The analysis of the indentation experimental data was performed according to the procedure developed by Oliver and Pharr [77] which has its roots in the early work by Hertz in which a method was developed to analyze the contact between a rigid sphere and a flat surface [78]. The experimental values used in the analysis are shown in Figure 2.3.

Figure 2.3(a) shows a schematic cross-section of the geometry produced as the indenter is loaded and unloaded onto the specimen surface. The load is applied to a maximum of P_{max} and a maximum depth of h_t, shown in both (a) and (b). During the loading, the total displacement h_t can be written as

$$h_t = h_c + h_s \ or \ h_t = h_e + h_f \tag{2.13}$$

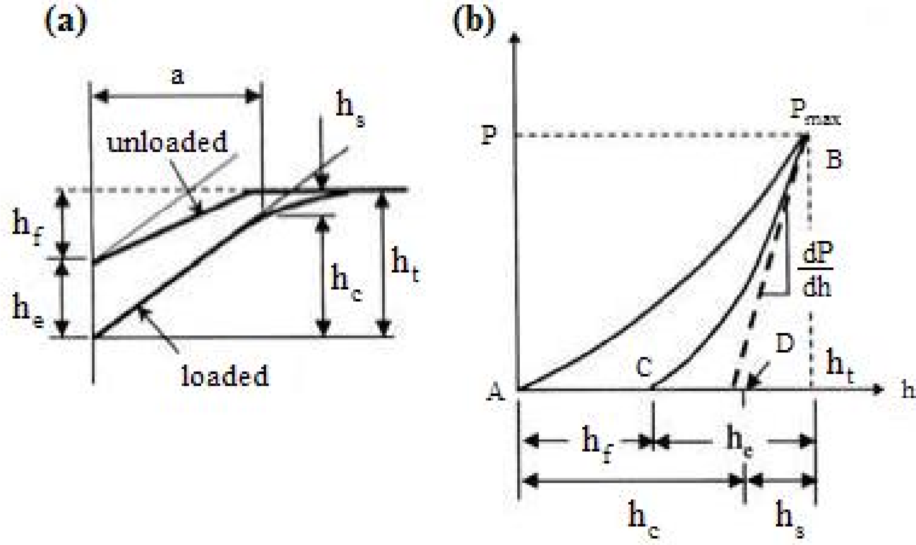

Figure 2.3: (a) Schematic of indenter and sample surface geometry for a Berkovich indenter. (b) Load versus displacement curve for the full loading and unloading. Variables are defined in the text. After Reference [78].

where the contact depth h_c is the distance that the indenter maintains contact with the surface, h_s is the displacement of the surface at the outer contacting edge of the indenter, h_e is the displacement due to elastic deformation of the surface and h_f is the final depth of the impression when the indenter is completely withdrawn. Figure 2.3(b) shows the respective load versus displacement curve for the indentation and shows where the various displacements are located relative to the curve. This curve contains the necessary experimental data needed to obtain the hardness and elastic modulus. The parameters of most interest, which will be used to extract material properties, from the curve of Figure 2.3(b) are the maximum load P_{max}, the slope of the unloading portion of the curve dP/dh, also known as the contact stiffness of the material S, the maximum displacement at peak load h_t, and the contact depth h_c.

The experimental analysis begins by observing the early work by Tabor [79] in which load and displacement indentation methods were utilized to obtain the mechanical properties of materials. Tabor developed an equation to effectively account for the non-rigid behavior of the indenter and its effect on the load-displacement behavior and determine a reduced elastic modulus E_r of the material investigated. It can be defined as

$$\frac{1}{E_r} = \frac{1-\nu^2}{E} + \frac{1-\nu_i^2}{E_i} \tag{2.14}$$

where E and ν are the elastic modulus and Poisson's ratio for the sample investigated, respectively,

and E_i and ν_i are the same material properties for the indenter. The reduced elastic modulus can be found by using the equation for the contact stiffness of the material S, developed by Bulychev, Alekhin, and Shorshorov in the 1970s [80]

$$S = \frac{dP}{dh} = \frac{2}{\sqrt{\pi}} E_r \sqrt{A} \tag{2.15}$$

where S = dP/dh is the experimentally measured stiffness, or slope, obtained from the unloading portion of the curve in Figure 2.3(b), E_r is the reduced elastic modulus and A is the projected area of the elastic contact.

The projected area of contact A is also used to determine the hardness and can be found by using the geometry of the indenter and the contact depth h_c, obtained from the load-displacement curve. For a Berkovich indenter, the equation for the area of the indenter is

$$A(h_c) = 24.5h_c^2 + C_1 h_c^1 + C_2 h_c^{1/2} + C_3 h_c^{1/4} + \ldots + C_8 h_c^{1/128} \tag{2.16}$$

where the first term $24.5h_c^2$, is the area function for a perfect Berkovich indenter and the remaining terms are added to take into account the imperfect nature and blunting of the indenter tip. Using this along with the stiffness obtained from the curve, the elastic modulus can be obtained from Eqn. (2.15). The hardness of the material can be evaluated by using Eqn. (2.16) along with the maximum load P_{max}, in the following equation

$$H = \frac{P_{max}}{A} \tag{2.17}$$

where H is the indentation hardness of the material.

2.6 Four-Point Probe

The four-point probe method is a basic technique used for measuring the electrical sheet resistance and resistivity of a film. It consists of four linear, metallic probes which contact the metallic surface in order to make an electrical connection. The instrument operates by having a current carried through two outer pins while the drop in voltage V_A, is measured between the two inner probes [81] as shown in Figure 2.4.

In obtaining the resistance, there can be effects arising from specimen geometry which can interfere with the measurements, such as variation in tip spacing or location near specimen edges [81]. This can be accounted for by utilizing a dual configuration which involves taking a second resistance measurement using an alternate probe configuration as shown in Figure 2.4. In this

configuration, current is passed through the first and third pins while the second and fourth pin record the corresponding voltage drop V_B.

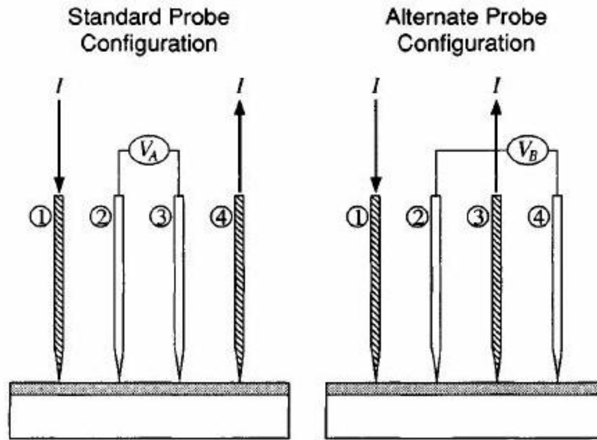

Figure 2.4: Standard and alternate instrument layout for sheet resistance measurement using the four-point probe method [81].

Use of the dual configuration technique allows for the correction of measuring inconsistencies due to the geometry [81]. Once the voltage drop is obtained, the sheet resistance or sheet resistivity R_s, in units of Ω or more commonly Ω/square can easily be obtained from the following

$$R_s = \begin{cases} 4.532 \cdot R_A \\ 5.710 \cdot R_B \end{cases} \tag{2.18}$$

where $R_A = \frac{V_A}{I}$ and $R_B = \frac{V_B}{I}$ and the constants, 4.532 and 5.710 represent geometrical correction factors [82]. Once the sheet resistance is determined and the thickness of the film is known, the bulk resistivity ρ, in units of Ω-cm, can be determined as

$$R_s = \frac{\rho(\Omega - cm)}{t(cm)} \tag{2.19}$$

To minimize the uncertainty of the measurement, a minimum contact resistance between the probes and the specimen surface should be maintained. High contact resistance can be avoided by removing any thick oxide layers which may be present on the surface and using clean probes which are free from contamination. Also, probes that are relatively sharp along with increased load can break through an oxide layer and contact a more conductive layer. Also, there should be minimum current leakage across the surface or across a film layer boundary. This can be achieved by preparing a clean surface for measurements [81].

Chapter 3

Experimental

3.1 Specimen preparation

Polycrystalline Au films prepared at MIT were used for the initial Au baseline studies. Single crystal (100) Si with a 200 nm thick thermally grown oxide layer was used as the substrate. For the first study, a Ti adhesion layer, approximately 10 nm thick, followed by a polycrystalline Au film, with a thickness of 700 nm, was deposited using a commercial electron-beam evaporator. The coated Si wafers (6 in.) were subsequently cleaved to produce individual specimens. The Au films were deposited at depositions rates of 1.5, 3 and 4.5 Å/s. In the second study, two sets of Au films, one with a 20 nm Ti adhesion layer and one with a 20 nm Cr adhesion layer were prepared using a deposition rate of 3 Å/s. To investigate the effect of heat treatment, specimens with a Ti or Cr adhesion layer were also annealed at 100 °C for 1 hr in a N_2 environment. The annealing temperature was chosen to enhance adhesion between the Au film and the Ti or Cr adhesion layers.

For the expanded Au film studies, specimens were prepared at LANL. Au-Si films were deposited by the co-evaporation of Au and Si onto (100) single crystal Si substrates using a commercial electron beam evaporator operating at room temperature with a base pressure of approximately 2 - 4 x 10^{-7} Torr. Prior to co-evaporation, a 10 nm thick Ti adhesion layer was deposited onto the substrate. The Au and Si were co-deposited at a combined rate of 10 Å/s to produce composite films with thicknesses of approximately 1000 nm and with nominal Si concentrations of approximately 2, 5, 15, and 25 at. %. Pure Au films with thicknesses of approximately 1000 nm were also prepared to serve as control specimens. Two sets of specimens were used for the experiments. To investigate the effect of heat treatment, selected specimens with Si concentrations of 5, 15 and 25 at. % from the first set were annealed at 300 °C in vacuum for 1 hour. The heat treatment temperature was based

upon a recomendation by the group responsible for film preparation. RBS and Particle Induced X-ray Emission (PIXE) were also performed at LANL to determine the actual composition present in the first and second set of specimens, respectively. For the first set of specimens, the actual Si concentration could not be measured from the RBS data due to Si signal overlap between the Si and low energy Au signals resulting from multiple scattering and possible non-uniform Si distribution. Therefore, these specimens will be referenced by their nominal Si concentrations. Si concentrations for the second specimen set were found to be 2.5, 6, 13 and 21 at. % for the nominal concentrations of 2, 5, 15 and 25 at. %, respectively.

3.2 Nanoindentation and Atomic Force Microscopy

Nanoindentation experiments were conducted using a commercially available, load-controlled nanoindenter (TriboScope Nanomechanical Test System® manufactured by Hysitron, Inc.) interfaced with an AFM (diDimension® 3100 manufactured by Veeco, Inc.).

Prior to the performing of all nanoindentation experiments, the AFM was used to measure the local surface topography and determine the roughness (Ra, Rq, Rz) over a 1 μm x 1 μm scan area.

A Berkovich diamond indenter (E = 1141 GPa, $\nu = 0.07$ [83]) was used for all nanoindentation experiments. The Berkovich indenter has a three-sided pyramidal type geometry which consists of a 65.3° face angle, allowing for the same projected area-to-depth ratio as a Vickers indenter, and a tip radius on the order of 50 - 100 nm. [78]. The specimen was placed in the instrument's thermal enclosure and the specimen, indenter and instrument were allowed to thermally equilibrate for 10 - 12 hours prior to beginning the experiments. Before each indentation, the local surface topography was measured, and the thermal drift rate was measured over a 5 second interval to confirm that it was less than 0.1 nm/sec. For each indentation, the load pattern shown in Figure 3.1 was used. The loading sequence consisted of a 30 second load application up to the peak load, a 60 second hold at peak load to account for creep in the material, followed by a 10 second unloading to 10% of the peak load and a 60 second hold to allow for the measurement of the system's thermal drift and finally a 2 second unloading to zero load. A typical load displacement curve is shown in Figure 3.2

The instrument's compliance and the area function of the Berkovich indenter were determined prior to the experiments by performing indentations upon aluminum and fused silica according to the procedure developed by Oliver and Pharr [77]. A description of the procedure followed can be found in [84]. Indentations were performed to minimum contact depths of at least 20 times the arithmetic mean roughness (20 x Ra), according to the standards set forth by the International

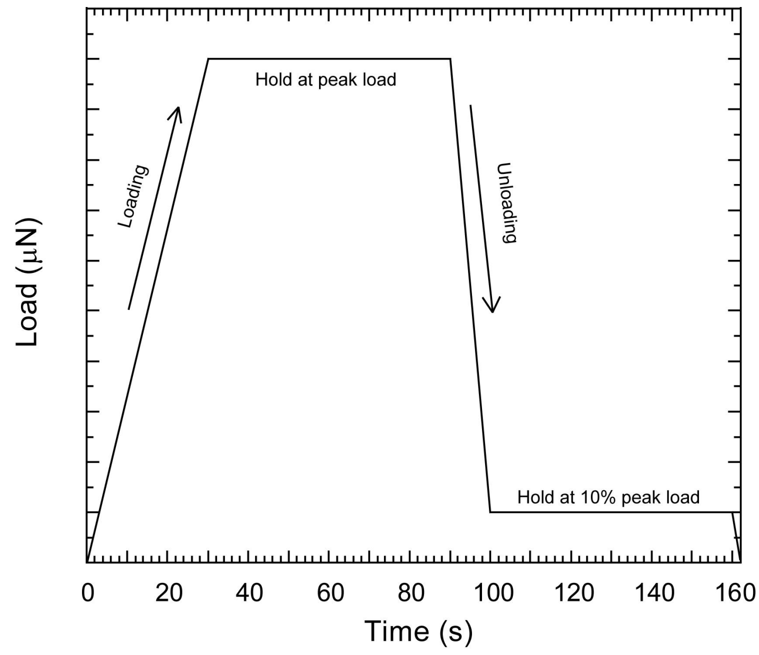

Figure 3.1: Load pattern used for all indentation experiments.

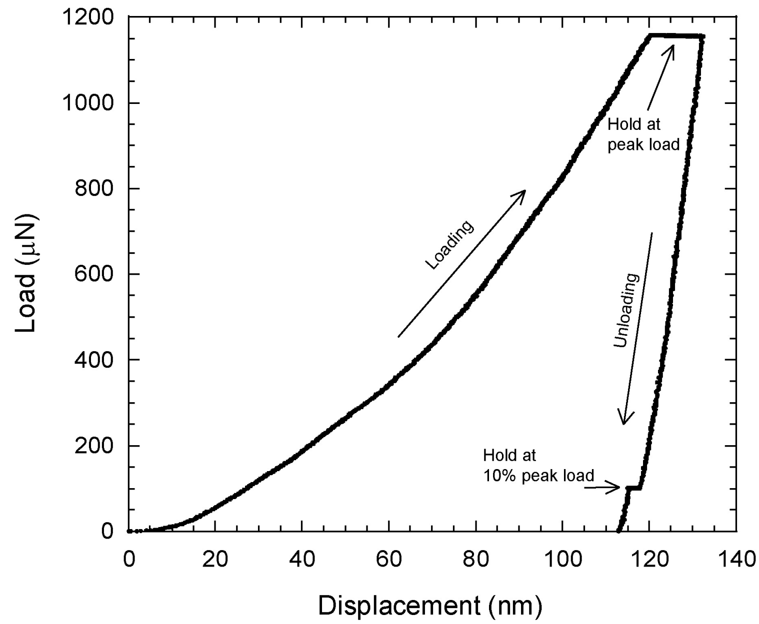

Figure 3.2: Typical load-displacement curve for the load pattern shown in Figure 3.1, obtained for the Au/2 at. % Si film.

Organization for Standardization (ISO) [85]. On some cases, these specifications had to be slightly modified, e.g., minimum contact depth of at least 5-10 x Ra, to incorporate for the increased surface roughness measured by AFM. For most indentations performed, the maximum normalized contact depth used was 10% to avoid the influence of the substrate.

After performing each indentation, the measured load versus displacement data was analyzed using the computer program, Indentation Data Analyzer (IDA), developed by M. Klopfstein [86]. From this software, the measured hardness H, reduced elastic modulus E_r, contact depth h_c and material stiffness S, were determined according to the method of Oliver and Pharr [77]. The software also determined the drift rate from the 60 s hold period at 10% of the peak load and the measured load and displacement data were corrected. A total of 5 measurements were conducted for each indentation load and an example of the repeatability is shown in Figure 3.3. The procedures described above are discussed in further detail in Appendix B.

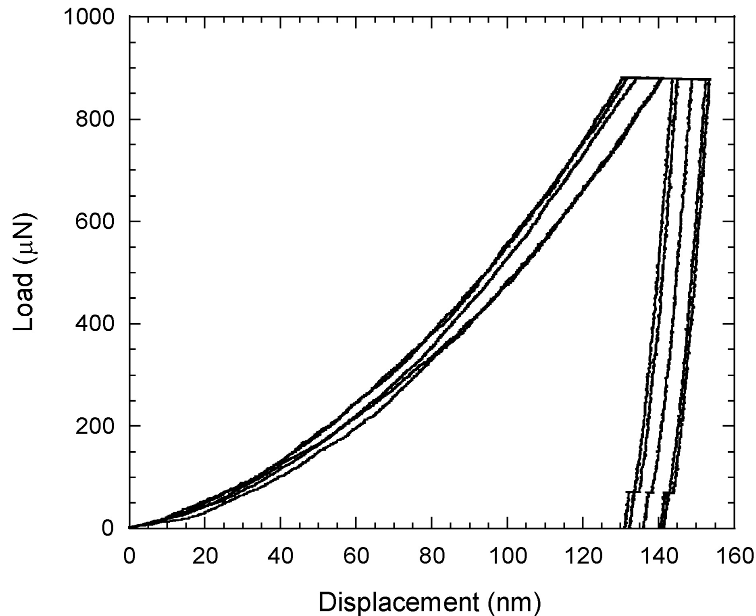

Figure 3.3: Load-displacement plot showing an example of the repeatability for 5 measurements conducted at a given load.

3.3 Four-Point Probe

Four-point probe measurements were conducted using a commercially available four-point resistivity probe instrument (FPP-5000 manufactured by Veeco, Inc.). The FPP-5000 simplifies measurement

of the electrical properties of materials by having the electronics and probe configuration contained in a single instrument. The instrument is capable of measuring the material resistance V/I in units of Ω, sheet resistance in units of Ω/square, resistivity in units of Ω-cm and thickness in units of 10^{-3} in. or μm. An accuracy of 0.5% is achievable on all measurements in the resistance range of 5 mΩ - 5 kΩ [87].

The probe apparatus was fixed to the instrument and set at a constant force (the probe pressure was pre-adjusted on the instrument) and the measurement was made by pressing the wafer onto the probes. This setup eliminated variations in force due to the operator or the specimen thickness. The probes used for the measurements were placed in a standard configuration, as shown in Figure 2.4, and had a spacing of approximately 1.6 mm. The instrument automatically applies a geometric correction factor of 4.53 which can be multiplied further by an additional correction based on the shape of the specimen and probe spacing [87]. For the results in this work, additional geometric correction factors were applied ranging from 0.765 - 0.998 which varied depending upon the shape and dimensions of the specimen [88]. Correction factors for a rectangular specimen geometry were based upon the ratio of the specimen dimensions and the ratio of the smaller specimen dimension to the probe spacing, and correction factors for a quarter wafer specimen geometry were based on the ratio of the distance from specimen edge and the probes to the probe spacing [88]. The resistivity measurements were conducted by inputing the film thickness and geometric correction factor into the instrument, placing the specimen into the wafer holder with the backing plate onto the wafer and then simply lowering the wafer onto the probe tips. The instrument automatically measured the film resistivity each time the specimen was lowered and contacted the probe tips. For each specimen, the measured resistivity was obtained from an average of four measurements which were conducted by rotating the wafer holder roughly 90° after each measurement. A more detailed procedure on the four-point probe measurements is given in Appendix C.

3.4 Supporting characterization techniques

3.4.1 Transmission Electron Microscopy

In order to investigate the material structure of the Au-Si specimens, TEM specimens were prepared and subsequently characterized at LANL. The specimens were prepared by co-evaporation of the Au-Si thin films (≈ 30 - 50 nm), with a nominal Si concentration of 25 at. %, deposited on NaCl. The films were then floated off of the NaCl substrates onto TEM grids for characterization.

3.4.2 X-ray Diffraction

XRD measurements were conducted in the OSU Department of Chemistry using a commercially available X-ray Powder Diffractometer (D8 Advance® manufactured by Bruker AXS, Inc.). The instrument was operated at a voltage and current of 40 kV and 30 mA, respectively, and Cu$K_{\alpha 1}$ radiation with a wavelength, $\lambda = 1.541$ Å was used as the x-ray source.

The measurements were conducted using a $\theta - 2\theta$ scan with the specimen mounted in a reflection geometry as shown in Figure 3.4. The angles θ and 2θ represent the angle between the x-ray source and the specimen, and the angle between the projection of the x-ray source and the detector, respectively. The specimen is placed onto the specimen holder which is mounted to the goniometer. The x-ray source and detector are mounted onto the outer groove of the goniometer which allows for a full 360° rotation [89] with a maximum usable 2θ range of -110° to 168°, maximum angular speed of 30°/s and capable of angular increments as small as 0.0001° [90].

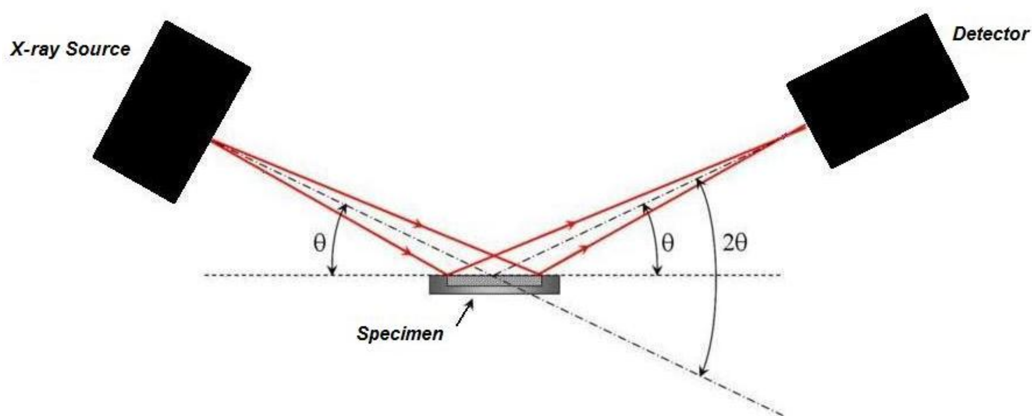

Figure 3.4: Schematic showing the main setup of the x-ray diffractometer for performing the $\theta - 2\theta$ scan with the specimen mounted in a reflection geometry. After Reference [91].

Consider a beam of x-rays, generated by the instrument's radiation source, defined and collimated through a series of slits [89], incident on the specimen surface at an angle θ, as shown in Figure 3.5. If the incident beam is diffracted off of the material's upper plane of atoms and from the lower plane, at a distance of d below, the beam diffracted from the lower plane travels a greater distance causing the effective path difference between the two beams to be equal to $2d\, sin\theta$ [89]. Constructive interference occurs when both x-rays are in phase and the path difference becomes a multiple of the

x-ray wavelength λ, leading to Bragg's Law which can be written as

$$2d\,sin\theta = n\lambda \tag{3.1}$$

where d is the interplanar spacing, θ is the angle of the incident x-ray beam and the specimen, n = 1, 2, 3 . . . , and λ is the wavelength of the x-ray source. Most often in XRD, n = 1 since higher order diffractions are typically weak [92]. The diffracted beam is then passed through a series of additional slits and the Kα radiation is isolated through the monochromator and the intensity of the beam is measured by the detector.

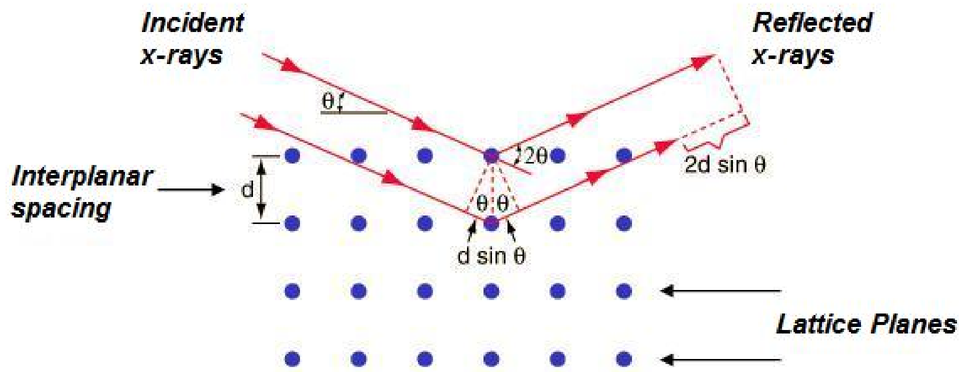

Figure 3.5: Schematic showing the diffraction of an incident x-ray beam with the upper two crystal lattice planes separated by an interplanar distance d. After Reference [92].

The measured data is processed by the instrument's software and a plot of the detected x-ray intensity versus the angle 2θ is generated which shows a pattern of the diffraction peaks generated from the measured material. The peaks can be identified by comparison with known material reference data using the Powder Diffraction File (PDF). The PDF database was created and is managed by The Joint Committee on Powder Diffraction Standards (JCPDS), established in 1969 and later became known under its present name, the International Centre for Diffraction Data (ICDD) [89]. The latest software by the ICDD, the PDF-4+ 2007 with DDView+ and PDF-2 Release 2007 with DDView+ contain diffraction pattern entries on 272,232 and 199,574 materials, respectively [93]. For this work, the peaks were identified through access to the ICDD PDF either through the diffractometer software or using the PDF-2 Release 2007 with DDView+ software.

The material grain size was measured from the broadening of the diffraction peaks using the software Win-Crysize installed on the instrument's computer. The software determines the grain

size by analyzing data which has been processed using a profile-fitting program and corrected to account for instrumental line broadening effects using a standard Pb reference material.

Chapter 4

Results and Discussion

4.1 Polycrystalline Au film baseline studies

4.1.1 Variable deposition rate

Surface Topography

Prior to investigation of the Au film mechanical properties by nanoindentation the topography of the film was measured by AFM. Figure 4.1 shows 1 μm x 1 μm AFM images of the surface topography for the Au films deposited at rates of 1.5, 3 and 4.5 Å/s. The surfaces of the film show small, uniformly sized nodules which have been previously reported for electron-beam evaporated Au films [94, 95]. It has been reported that each Au grain can consist of several nodules [94] and that factors such as the substrate temperature, deposition rate and thickness of the adhesion layer can influence the nodule size [96]. The surface of the 1.5 Å/s film varies slightly from the other films having larger nodules present on the surface. The surface roughness for the films was approximately 4 - 5 nm Ra over the 1 μm^2 area with values for individual films given in Table 4.1. Each value for the surface roughness represents the average of 3 measurements.

Mechanical Properties

Film hardness and elastic modulus as a function of the contact depth h_c, normalized to the thickness of the film, were determined from the measured nanoindentation data and are shown in Figures 4.3 and 4.4. The data represent the average of five measurements and the error bars correspond to the maximum and minimum values obtained. No material pile-up was observed for the Au films at a normalized contact depth of about 0.10, as seen in an indentation profile shown in Figure 4.2.

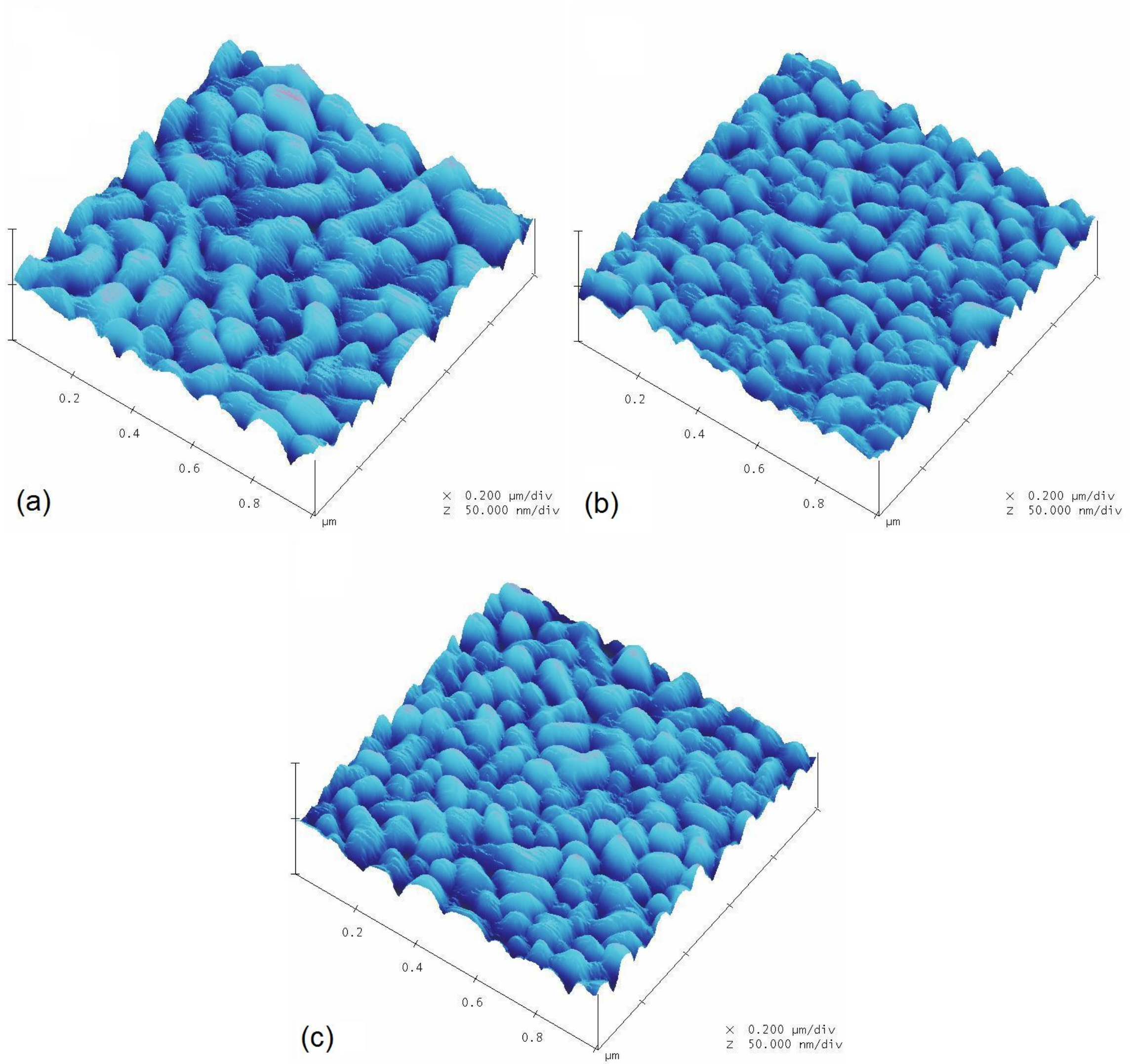

Figure 4.1: AFM image (1 μm x 1 μm scan size) showing the topography of Au films deposited at a deposition rates of (a) 1.5 Å/s, (b) 3 Å/s, and (c) 4.5 Å/s.

Specimen	**Roughness**		
	Ra (nm)	**Rq (nm)**	**Rz (nm)**
Pure Au - 1.5 Å/s	4.8	5.8	35
Pure Au - 3.0 Å/s	4.6	3.7	30
Pure Au - 4.5 Å/s	4.1	5.0	32

Table 4.1: Average roughness values for pure Au films evaporated at varying deposition rates.

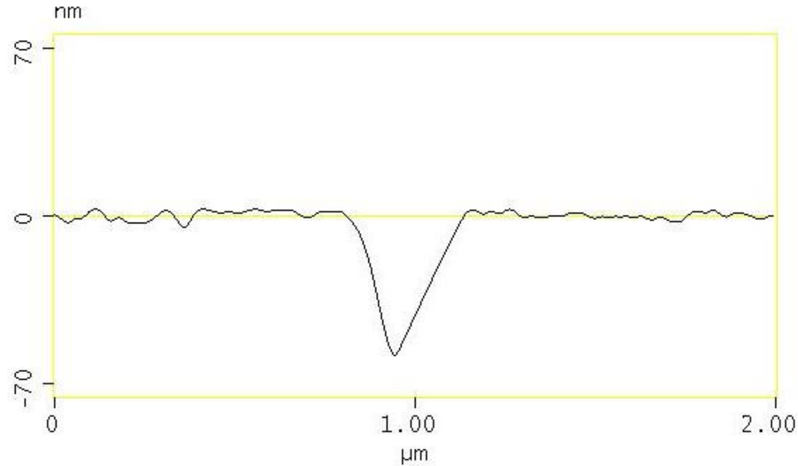

Figure 4.2: Image of the profile of an indentation, conducted on the pure Au film deposited at 1.5 Å/s at a normalized contact depth of about 0.10, showing the lack of material pile-up.

The hardness was measured over the normalized contact depth range of 0.1 - 0.5 (corresponding to contact depths of 70 - 350 nm) and was found to be 1 GPa to $\sim$ 1.5 GPa for all films. The range of hardness values is consistent with the values of 1 - 2.3 GPa for Au films previously reported in the literature [14, 21, 22]. The hardness is shown to be about the same for the 3 Å/s and 4.5 Å/s deposition rates and is slightly higher for the 1.5 Å/s rate, at a normalized contact depth of greater than 0.2. It has been reported that larger initial grain sizes form during the microstructural evolution of polycrystalline films deposited at lower deposition rates [97]. This is consistent with the Au nodular size observed in the AFM images. The higher measured hardness for the film with the larger nodules is inconsistent with the Hall-Petch relationship between hardness and grain size [72]. However, a clear relationship between nodule size and hardness can not be established since the relationship between nodule and grain size is currently unclear. The hardness is seen to increase at normalized contact depths of greater than 0.2, indicating the effect of the underlying Si substrate. This is consistent with the work by Xu and Rowcliffe [98] and Cao et al. [22] who have shown that for Au films, the substrate effect is minimized at normalized penetration depths of less than 0.2.

Nanoindentation was performed on (100) Si to investigate the properties of the substrate and the hardness was found to be approximately 9.6 GPa over a contact depth range of about 20 - 150 nm. The hardness of (100) Si has been reported in the literature to be as high as 13 GPa [70].

The elastic modulus was determined over the same depth range as the hardness and varied from approximately 80 - 130 GPa, increasing with increased normalized contact depth. The values

obtained for the elastic modulus are consistent with those reported in the literature of 77 - 115 GPa for Au films [21, 99–102]. The elastic modulus of the Si substrate was also measured by nanoindentation and found to be approximately 148 GPa. The elastic modulus values obtained for the Au films at normalized depths greater than 0.2 can be seen to approach this value in Figure 4.4. Elastic modulus values for (100) Si have been reported to range from 168 GPa [103] to 180 GPa [70] and are consistent with the value of 158 GPa measured for the (100) Si substrate at a contact depth of about 20 nm.

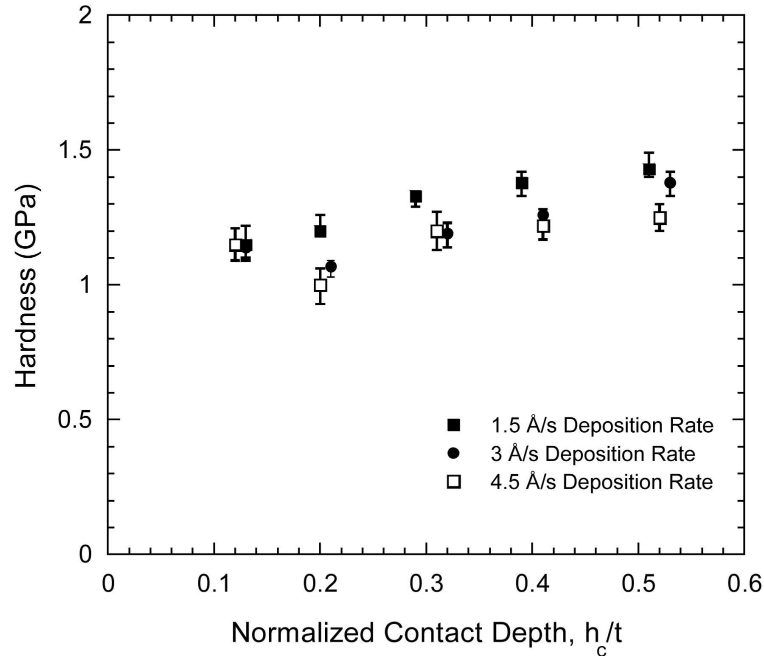

Figure 4.3: The effect of deposition rate on the hardness of Au thin films.

4.1.2 The effect of the adhesion layer and heat treatment

Surface topography

Similar to the previous specimen set, the surface topography was measured by AFM prior to performing nanoindentation. Figures 4.5 and 4.6 show 1 μm x 1 μm AFM images of the surface topography of both as-deposited and annealed Au films deposited on Ti or Cr adhesion layers. The surface roughness for the films, given in Table 4.2, was found to be approximately 2.5 - 3.5 nm Ra over the 1 μm^2 area. Each value for the surface roughness represents the average of 3 measurements. For the Ti adhesion layer specimens, the roughness decreased from 3 - 2.5 nm Ra as a result of the heat treatment, while the roughness of the Cr adhesion layer specimens increased from 3.0 - 3.5 nm Ra

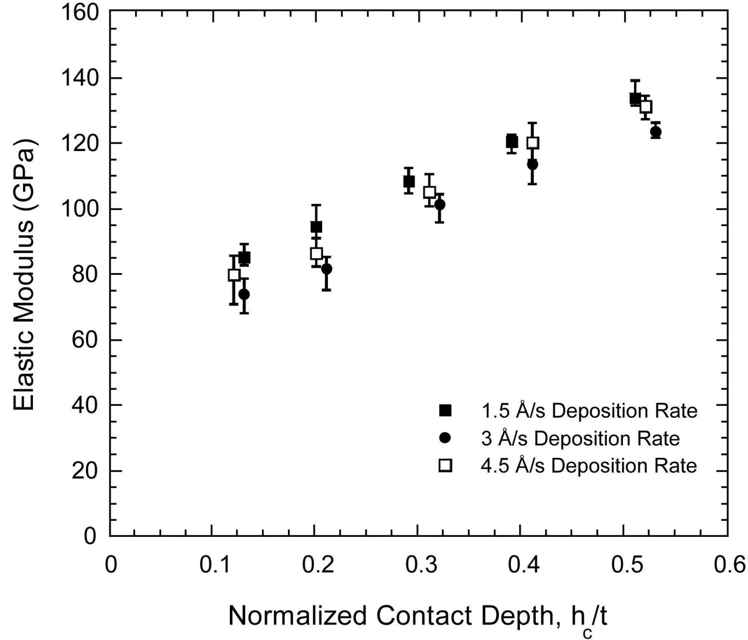

Figure 4.4: The effect of deposition rate on the elastic modulus of Au thin films.

after annealing. Figure 4.6 shows a change in the surface structure after heat treatment of the film with the Cr adhesion layer. Figure 4.7 shows a larger, 10 μm x 10 μm AFM scan of the surface. A plausible explanation for the surface cracks observed for this film could be due to diffusion of Cr toward the Au film surface, which has been reported for annealed Au films [96, 104, 105].

Specimen	**Roughness**		
	Ra (nm)	**Rq (nm)**	**Rz (nm)**
Au/Ti/SiO_2/Si - Annealed	2.5	3.1	20
Au/Ti/SiO_2/Si	3.0	3.7	23
Au/Cr/SiO_2/Si - Annealed	3.5	4.6	25
Au/Cr/SiO_2/Si	3.0	3.7	22

Table 4.2: Average roughness values for as-deposited and annealed pure Au films deposited on Ti or Cr adhesion layers.

Mechanical properties

Figures 4.10 and 4.12 show the hardness and elastic modulus as a function of the contact depth h_c, normalized to the thickness of the film. The data represent the average of five measurements

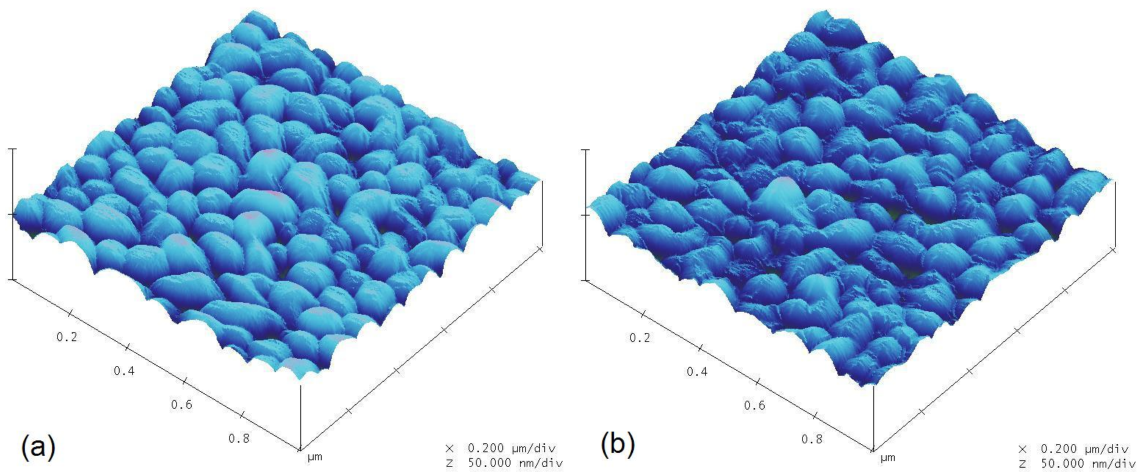

Figure 4.5: AFM images (1 μm x 1 μm scan size) showing the topography of (a) as-deposited and (b) annealed Au films deposited with Ti adhesion layers.

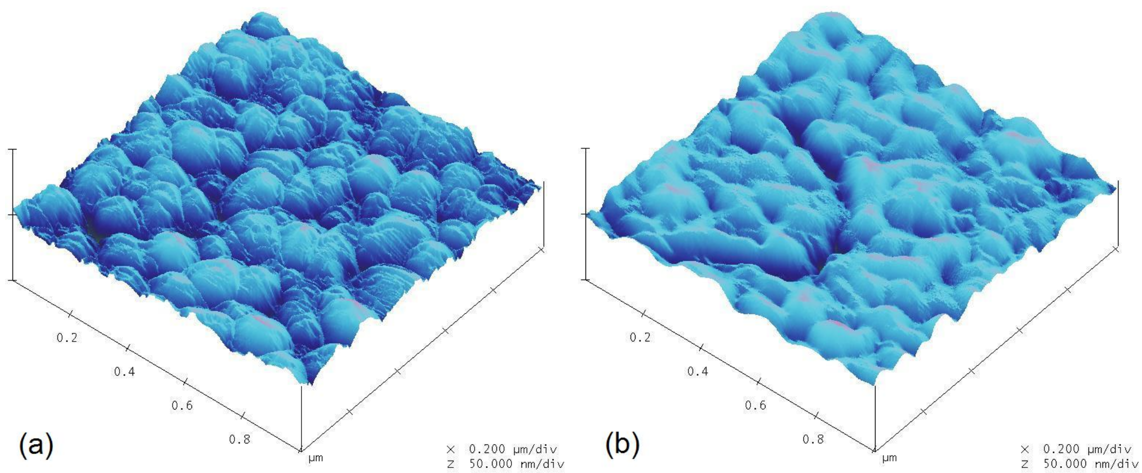

Figure 4.6: AFM images (1 μm x 1 μm scan size) showing the topography of (a) as-deposited and (b) annealed Au films deposited with Cr adhesion layers.

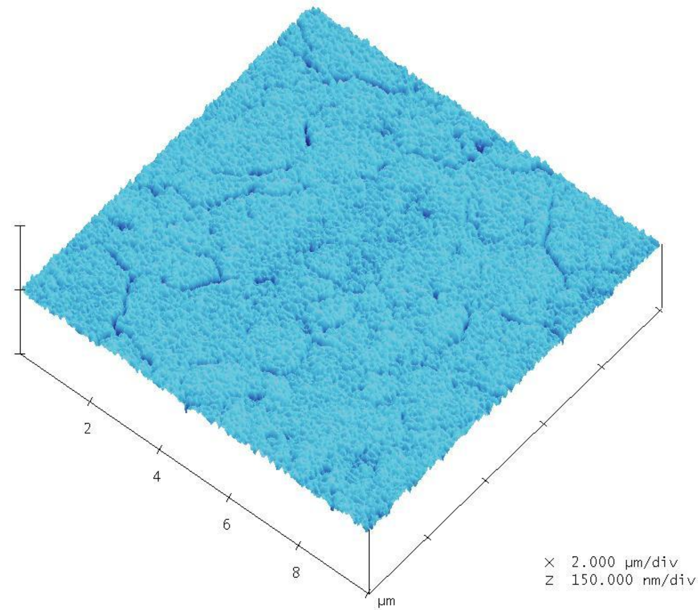

Figure 4.7: AFM image (10 μm x 10 μm scan size) showing cracks present on the surface of the annealed Au film deposited with a Cr adhesion layers.

and the error bars shown represent the maximum and minimum values obtained. Hardness ranged from 0.9 - 1.9 GPa and was seen to decrease with increasing normalized contact depth up to about 0.2. This is consistent with the indentation size effect, where the hardness is observed to increase at distances closer to the surface [106–109]. The effect is based on arguments from the strain gradient plasticity theory as discussed by Fleck et al. [106].

The indentation size effect can be seen in Figure 4.11 showing hardness of the annealed Au film with an underlying Cr adhesion layer at normalized contact depths up to 0.5. The hardness is seen to increase at normalized contact depths greater than 0.2 due to the increased influence of the underlying Si substrate, as expected. The increase in the error bars seen at lower depths could be due to the surface roughness. The minimum contact depth had to be modified to at least 10 x Ra to account for the increased surface roughness and avoid the influence of the substrate. The hardness values for this second set of films are also consistent with those previously reported in the literature [14, 21, 22]. However, recognizing the variations associated with the measurements, no significant effect of the adhesion layer and heat treatment on the hardness could be identified.

The elastic modulus was determined over the same depth range as the hardness and varied from 70 - 100 GPa, increasing with increased normalized contact depth. The values obtained for the elastic modulus are consistent with those reported in the literature of 77 - 115 GPa for Au

films [21, 99–102]. The increased influence of the Si substrate was also evident by the increase in elastic modulus at larger depths. Similar to the hardness measurements, no effect of the adhesion layer and heat treatment on the elastic modulus could be identified.

A sudden increase in penetration depth at a given load, commonly known as "pop-in", was observed for both as-deposited and annealed Au films as shown in load-displacement curves given in Figures 4.8 and 4.9. Pop-in in both as-deposited and annealed Au films has previously been observed by Miller et al. [94]. It has been reported that this effect can commonly occur either due to the sudden nucleation of dislocations at the beginning stages of plasticity or as the surface oxide layer is penetrated by the indenter [110]. Pop-in events were not observed for the other Au films presented in this study and the cause of this is currently unclear.

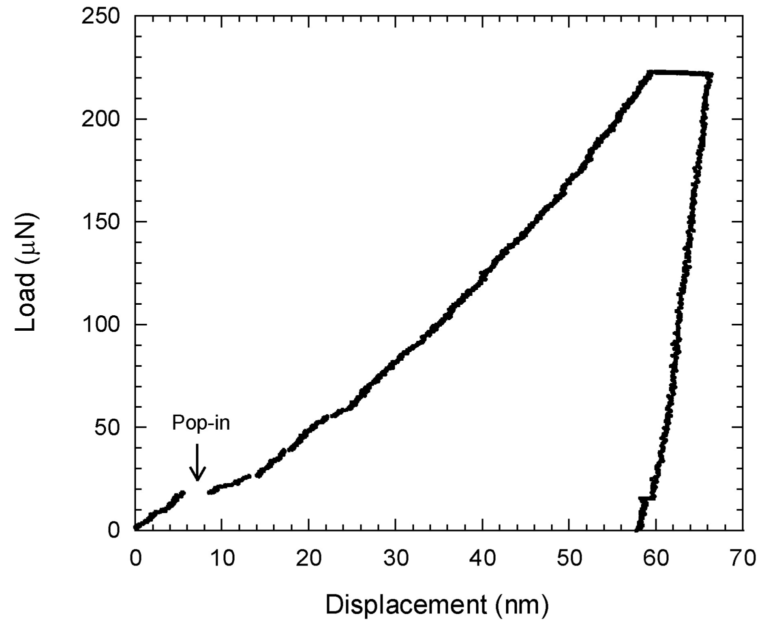

Figure 4.8: Load versus displacement curve for the as-deposited Au film with a Cr adhesion layer. A pop-in event was observed at a load of about 20 μN.

Electrical Properties

Four-point probe measurements were conducted on all films and values measured for the resistivity are shown in Table 4.3. The resistivity of the Ti adhesion layer specimens is consistent with the value of 2.35 $\mu\Omega$-cm reported for bulk Au [111]. The increased resistivity measured for the annealed Cr adhesion layer specimen could be affected by the diffusion of Cr into the Au film, as discussed earlier, which has been reported to lead to an increase in resistivity in Au films [96, 104, 105]. The

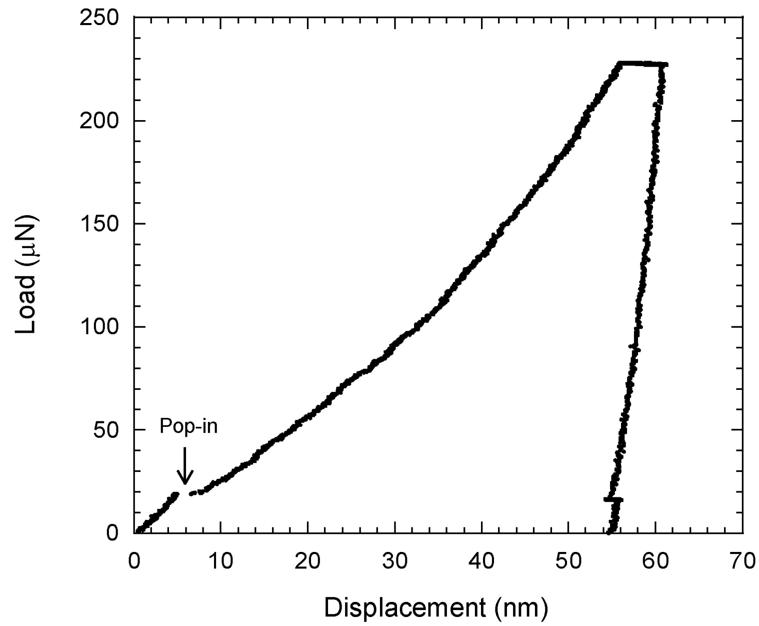

Figure 4.9: Load versus displacement curve for the annealed Au film with a Ti adhesion layer. A pop-in event was observed at a load of about 20 μN.

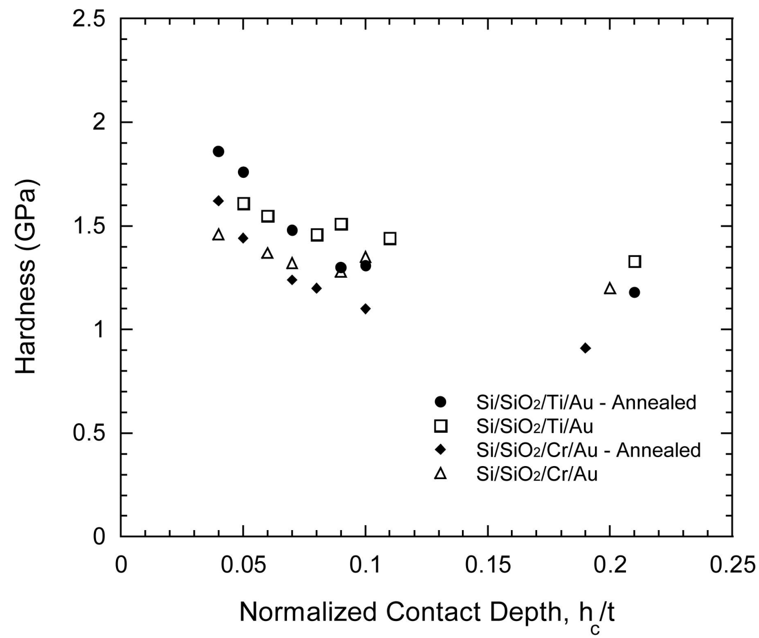

Figure 4.10: The effect of heat treatment and adhesion layer on the hardness of Au thin films.

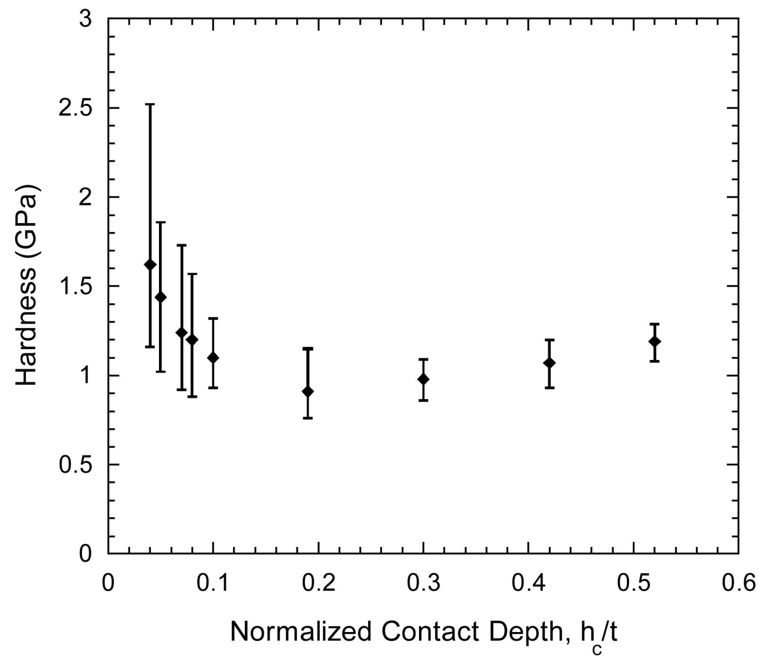

Figure 4.11: Evidence of the indentation size effect in annealed Au films with an underlying Cr adhesion layer.

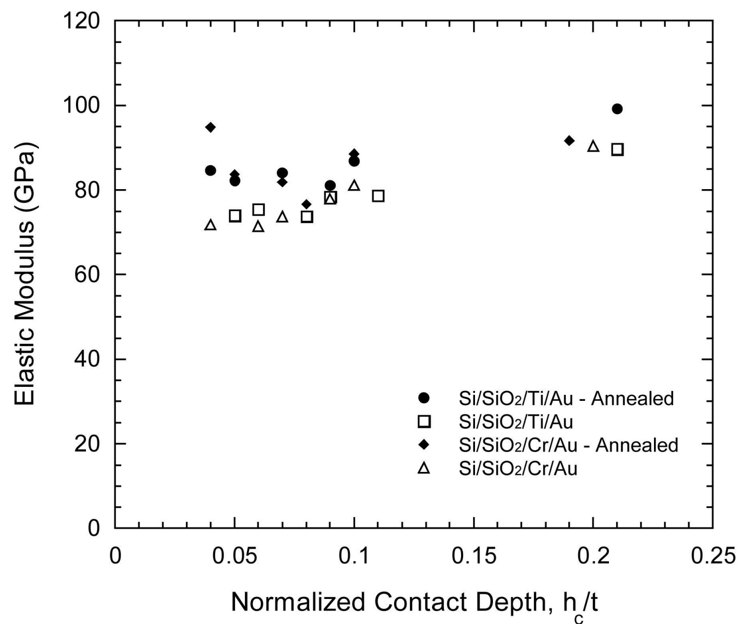

Figure 4.12: The effect of heat treatment and adhesion layer on the elastic modulus of Au thin films.

cause of the increased resistivity measured in the as-deposited pure Au film with Cr adhesion layer is unclear. Au thin film resistivity values as high as 5.3 $\mu\Omega$-cm have been reported by Artunc et al. [32], who attributed the higher values to grain boundary scattering .

Specimen	**Resistivity ($\mu\Omega$-cm)**	**Std. Dev. ($\mu\Omega$-cm)**
Au/Ti/SiO_2/Si - Annealed	2.36	0.2
Au/Ti/SiO_2/Si	2.24	0.3
Au/Cr/SiO_2/Si - Annealed	4.36	0.4
Au/Cr/SiO_2/Si	3.39	0.01

Table 4.3: Average resistivity values for as-deposited and heat treated pure Au films deposited on Ti or Cr adhesion layers.

4.2 Au-Si films

4.2.1 Initial shakedown experiments investigating the effect of Si addition and heat treatment

Surface topography

Figures 4.13 - 4.15 show AFM images of the surface topography of as-deposited and annealed Au films co-evaporated with 5, 15, or 25 at. % Si. AFM images of later prepared pure Au and Au films co-evaporated with 2 at. % Si are shown in Figure 4.16. The surface roughness for the films is given in Table 4.4. Each value for the surface roughness represents the average of 3 measurements. Heat treatment was not performed on the pure Au and Au/2 at. % Si films and will be further discussed in the next section. The surface roughness was slightly higher than the values measured on the initial Au baseline films. Furthermore, unusual peaks and craters were observed on all film surfaces during the AFM measurements. Observation using an optical microscope indicated that there was contamination on the film surfaces. Optical images of two typical surfaces are shown in Figure 4.17. Experiments performed at LANL determined that the contamination was caused by the graphite crucible used to contain the deposition materials during the evaporation process. It was reported that after observing the contaminated wafer with SEM, the same defects were found to be present on the sides of the graphite crucible. The problem was resolved when the graphite crucible was replaced with one made from W which was used to prepare future specimens.

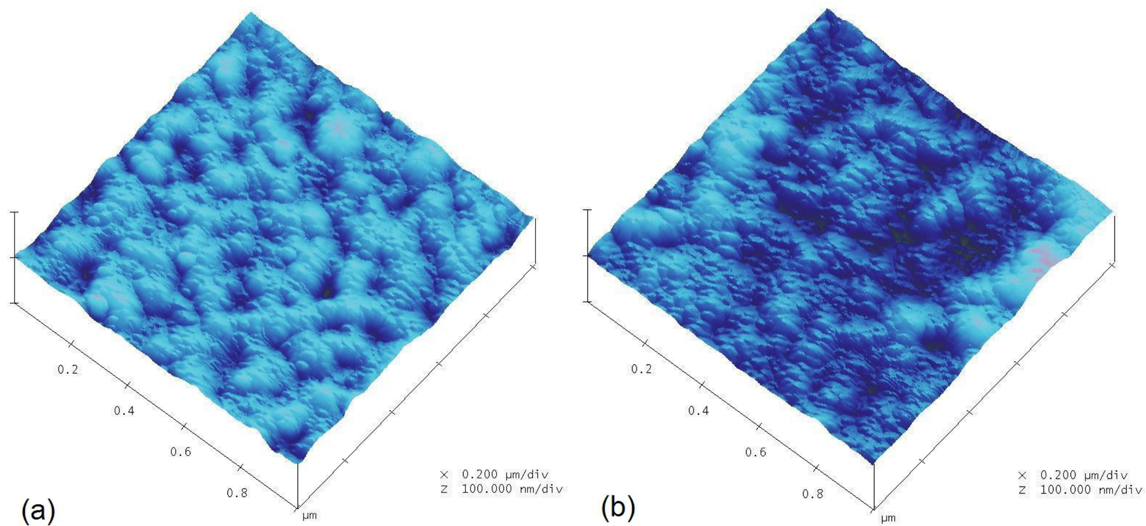

Figure 4.13: AFM images (1 μm x 1 μm scan size) showing the topography of (a) as-deposited and (b) annealed Au films co-evaporated with 5 at. % Si.

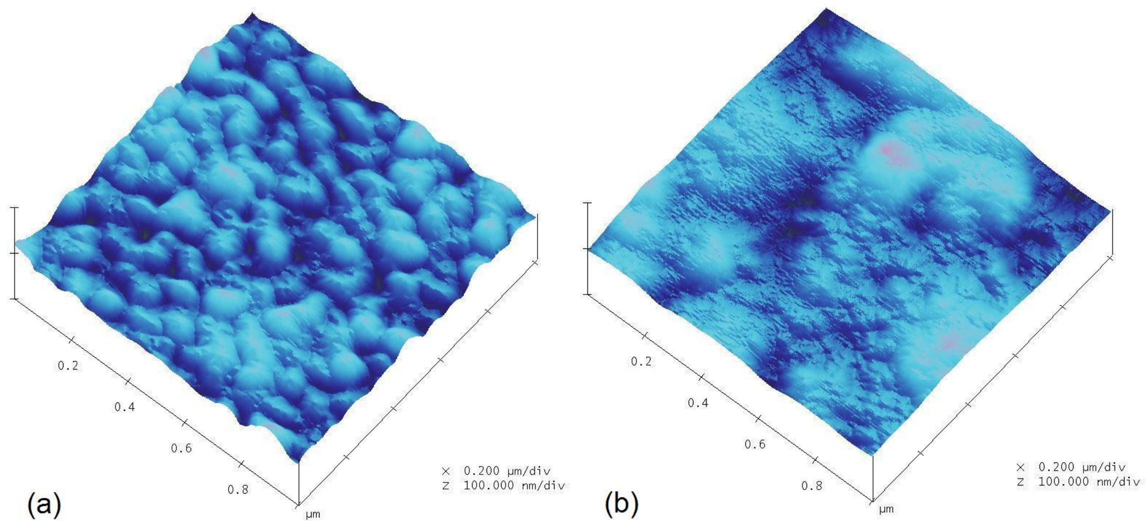

Figure 4.14: AFM images (1 μm x 1 μm scan size) showing the topography of (a) as-deposited and (b) annealed Au films co-evaporated with 15 at. % Si.

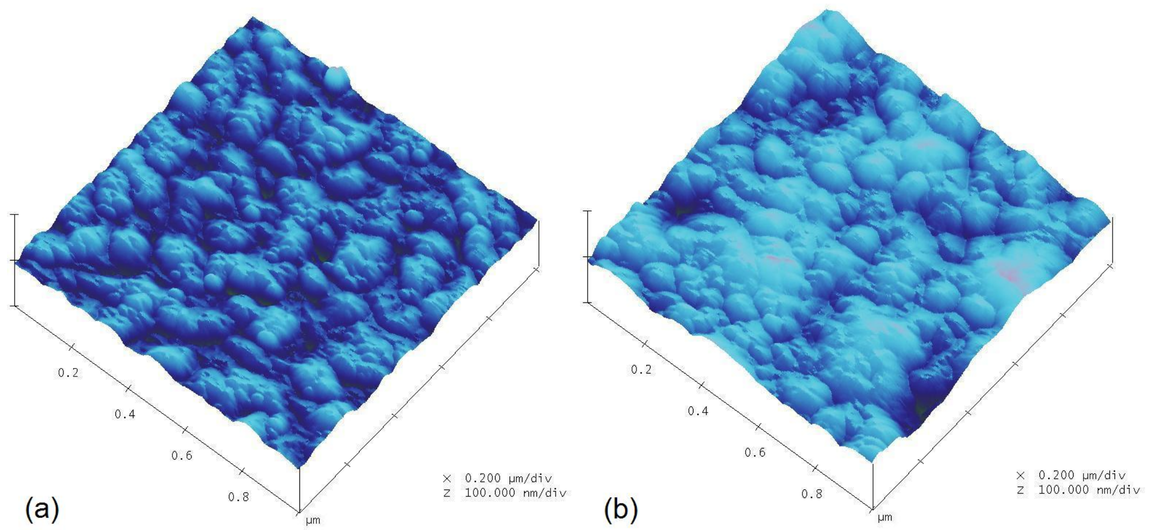

Figure 4.15: AFM images (1 μm x 1 μm scan size) showing the topography of (a) as-deposited and (b) annealed Au films co-evaporated with 25 at. % Si.

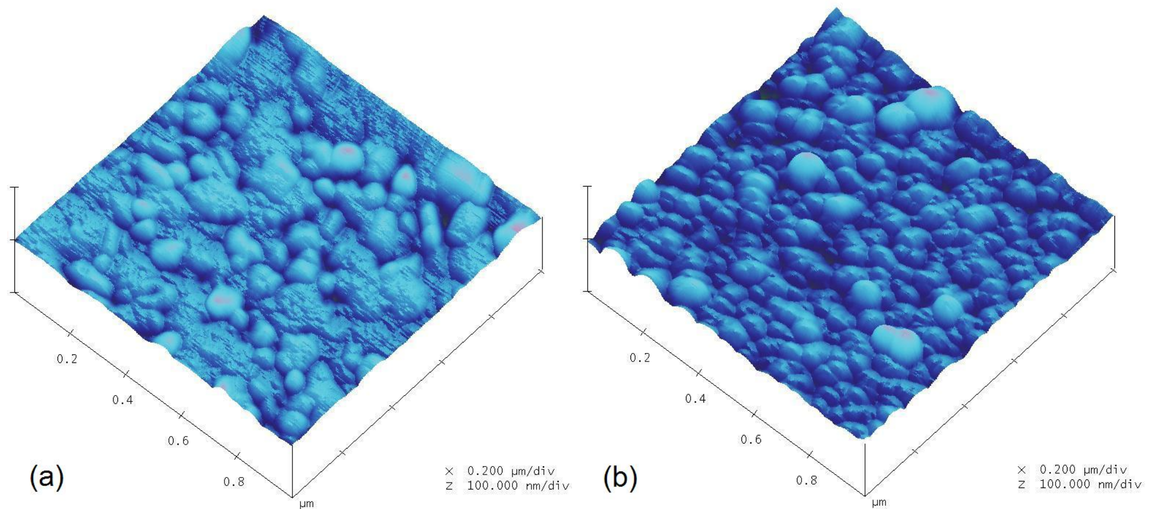

Figure 4.16: AFM images (1 μm x 1 μm scan size) showing the topography of (a) pure Au and (b) Au co-evaporated with 2 at. % Si.

Specimen	Roughness		
	Ra (nm)	Rq (nm)	Rz (nm)
Pure Au	2.8	3.5	22
Au/2 at. % Si	4.4	5.9	38
Au/5 at. % Si	5.3	7.0	42
Au/5 at. % Si - Annealed	5.9	8.0	43
Au/15 at. % Si	5.9	7.9	48
Au/15 at. % Si - Annealed	3.3	4.3	23
Au/25 at. % Si	5.0	6.2	40
Au/25 at. % Si - Annealed	6.0	7.6	40

Table 4.4: Average roughness values for the pure Au and as-deposited and annealed Au-Si films.

Mechanical properties

Figures 4.18 and 4.19 show the hardness and reduced elastic modulus as a function of Si content. The data represent the average of five measurements and the error bars correspond to the maximum and minimum values obtained. The hardness, measured at a normalized contact depth of about 0.10, was approximately 1.1 GPa for the pure Au film and is consistent with the values for Au films reported in the literature [14, 21, 22]. Hardness increased by approximately 65 - 95% (1.81 - 2.14 GPa) by the addition of 2 - 25 at. % Si, respectively. Due to the large error bars present in the measurements for the annealed films, no significant effect of the annealing on the hardness could be identified and therefore heat treatment was not further pursued.

The reduced elastic modulus was also measured at a normalized contact depth of about 0.10, and found to be about 90 GPa for the pure Au film. This corresponds to an elastic modulus of approximately 79 GPa, consistent with the bulk elastic modulus of 78 GPa, reported for Au films [103]. The reduced elastic modulus initially increased to 95 and 110 GPa by the addition of 2 at. % and 5 at. % Si, respectively, after which it decreased to 82 GPa for the Au/25 at. % Si film. After heat treatment, the reduced elastic modulus increased with increasing Si content from 5 - 25 at. % Si. Currently the cause of this effect is unclear.

After observation of the surface contamination, a new specimen set was prepared to investigate the effect of carbon contamination on the measurements and to ensure that the change in material

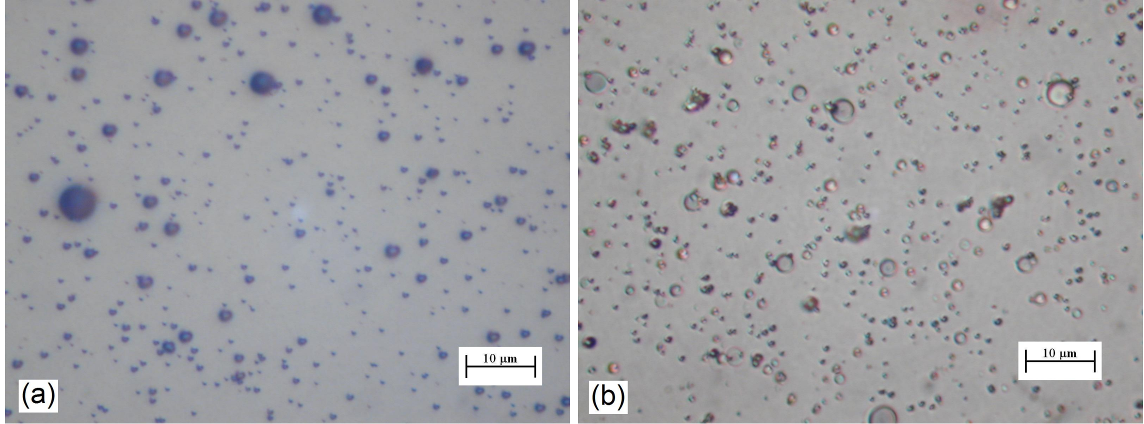

Figure 4.17: Optical images showing the overall surface roughness and contamination on the surface of the (a) Au/25 at. % Si and (b) Au/2 at. % Si films. AFM scans indicated that the asperities on the surface of the Au/2 at. % Si film had heights on the order of 2 - 3 μm.

properties was strictly due to hardening mechanisms resulting from interaction between the co-evaporated elements. The hardness and elastic modulus results shown in Figures 4.18 and 4.19 will be compared with the new films to investigate the effect of the contamination.

4.2.2 The effect of Si addition

Surface topography

Figure 4.20 shows AFM images of the surface topography of pure Au and Au films co-evaporated with 2.5, 6, 13, or 21 at. % of Si. The surface roughness is given in Table 4.5. Each value for the surface roughness represents the average of 3 measurements. The roughness was found to vary throughout the Si content range and appears to show no direct correlation between Si concentration and roughness. The surface roughness for the pure Au film was 3.4 nm Ra and consistent with the prior set. The roughness increased for all other films from 5.5 - 19.1 nm Ra for the 21 at. % Si and 13 at. % Si films, respectively. The cause of this variation in surface roughness is unclear.

Mechanical properties

Figures 4.22 and 4.23 show the hardness and reduced elastic modulus as a function of the Si content ranging from 2.5 - 21 at. %. The data represent the average of five measurements and the error bars correspond to the maximum and minimum values obtained. Some material pile-up was observed for

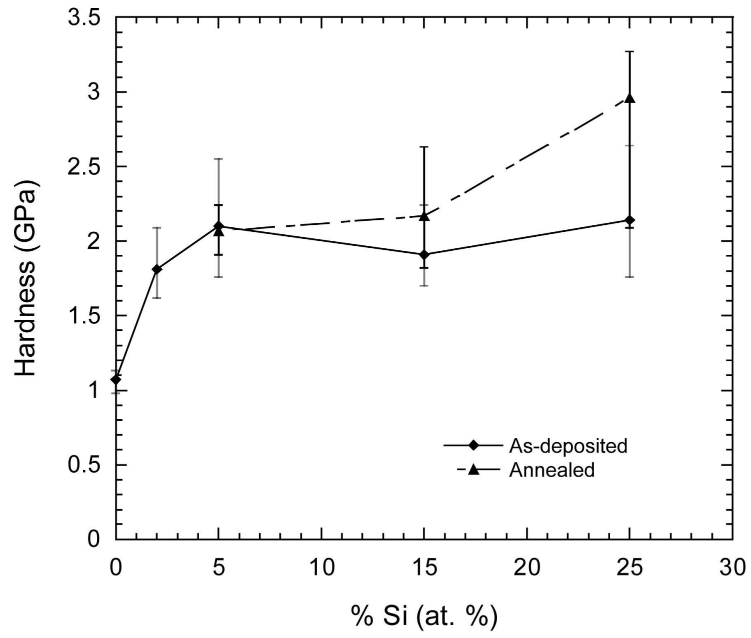

Figure 4.18: The effect of Si content and heat treatment on the hardness of pure Au and Au-Si films.

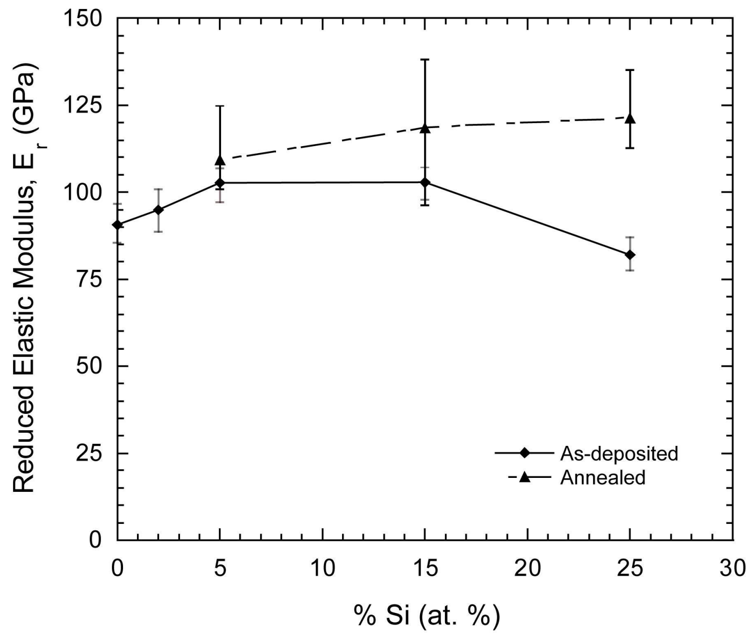

Figure 4.19: The effect of Si content and heat treatment on the reduced elastic modulus of pure Au and Au-Si films.

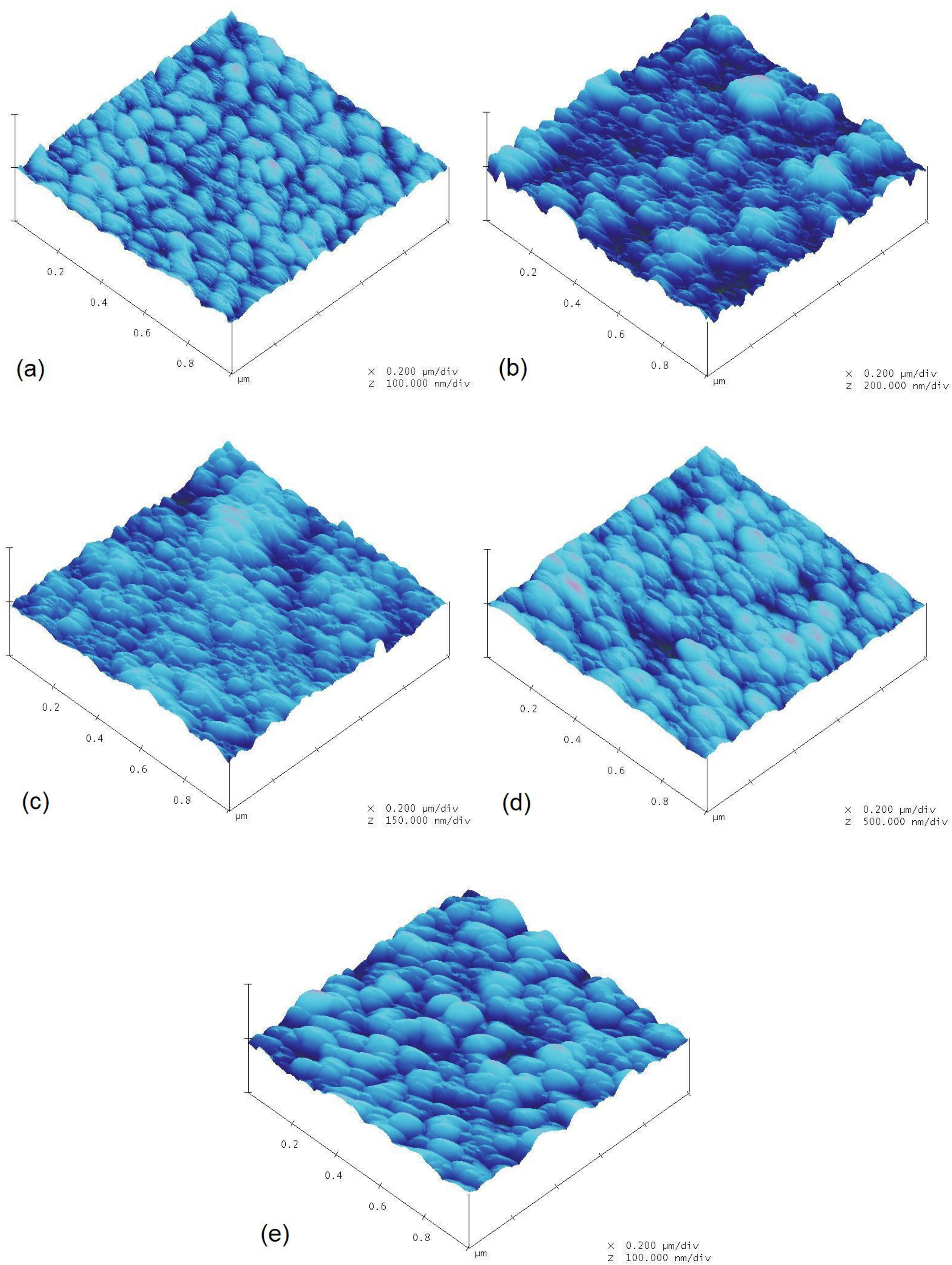

Figure 4.20: AFM images (1 μm x 1 μm scan size) showing the topography of (a) the pure Au and Au films co-evaporated with (b) 2.5 at. % Si, (c) 6 at. % Si, (d) 13 at. % Si and (e) 21 at. % Si.

Specimen	Roughness		
	Ra (nm)	**Rq (nm)**	**Rz (nm)**
Pure Au	3.4	4.2	26
Au/2.5 at. % Si	16.1	20.3	114
Au/6 at. % Si	7.6	9.6	59
Au/13 at. % Si	19.1	24.2	129
Au/21 at. % Si	5.5	7.2	45

Table 4.5: Average roughness values for pure Au films and Au films co-evaporated with 2.5, 6, 13 or 21 at. % Si.

the Au-Si films at a normalized contact depth of about 0.10, as seen in an indentation profile shown in Figure 4.21.

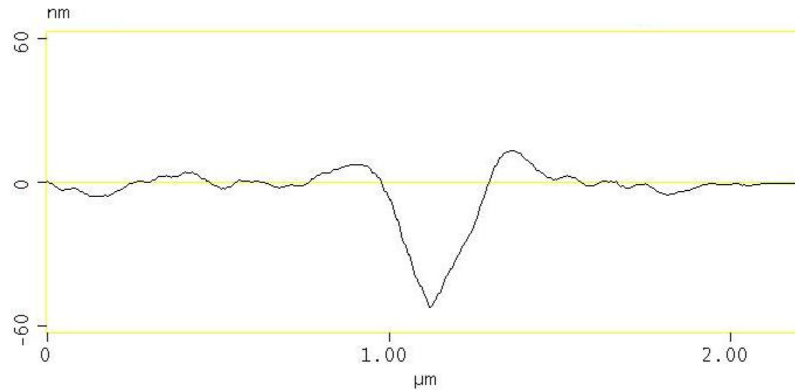

Figure 4.21: Image of the profile of an indentation, conducted on the Au/6 at. % Si film at a normalized contact depth of about 0.10, showing some material pile-up.

The hardness, obtained at a normalized contact depth of approximately 0.10, of the pure Au film was found to be approximately 1.2 GPa, and is again consistent with values for pure Au films reported in the literature [14,21,22]. Hardness was found to increase by about 40 - 80% (1.64 GPa - 2.13 GPa) by the addition of 2.5 and 6 at. % Si, respectively. The hardness increased approximately 102% to 2.41 GPa by the addition of 21 at. % Si. However, the hardness of the Au/13 at. % Si film was found to increase by only 14% to 1.36 GPa. Originally this was thought to be due to a non-uniform film deposition but measurements conducted on a second specimen (results given in Figure 4.22) indicated similar mechanical properties, minimizing this possibility and suggesting

another unknown phenomenon responsible.

The reduced elastic modulus was also obtained at a normalized contact depth of approximately 0.10, and found to be about 112 GPa for the pure Au film. This corresponds to an elastic modulus of approximately 100 GPa, consistent with values reported in the literature of 77 - 115 GPa for Au films [21,99–102]. The reduced elastic modulus is seen to follow a trend similar to the hardness with increasing Si content.

To investigate the effect of the carbon contamination on the original film properties, both measurements were compared simultaneously and are shown in Figures 4.24 and 4.25. The data compares well, when taking into account the error, for all Si concentrations except 13 at. % Si. The low hardness observed for this film could be attributed to the relieving of residual compressive stresses, which became evident after film buckling was observed on approximately 10% of the film surface. An optical image of the film, shown in Figure 4.26, indicates what is known as a "telephone cord" buckle which has been reported to occur due to compressive residual stresses in thin films [97]. A plausible explanation for the loss of film adhesion could be Si diffusion occurring into the Ti adhesion layer leading to the formation of titanium silicide, which has been shown to occur at room temperature [112]. If the thickness of the 10 nm Ti adhesion layer was small enough to allow for complete consumption, through reaction with the Si, then the film would be ineffective at providing adhesion of the Au-Si film to the substrate [113].

A comparison of the measured mechanical properties with those predicted by a simple rule of mixtures calculation is presented next. The rule of mixtures law specifies that a composite material's properties can be predicted by the properties of each phase in the composite, i.e., the matrix (Au) and the constituent (Si), according to their respective volume fractions [114]. This can be utilized to estimate the hardness and reduced elastic modulus of the Au-Si films according to the following equations

$$H'_{u.b.} = H_{Au}V_{Au} + H_{Si}V_{Si} \tag{4.1}$$

$$H'_{l.b.} = \{(V_{Au}/H_{Au}) + (V_{Si}/H_{Si})\}^{-1} \tag{4.2}$$

$$(E'_r)_{u.b.} = (E_r)_{Au}V_{Au} + (E_r)_{Si}V_{Si} \tag{4.3}$$

$$(E'_r)_{l.b.} = \{(V_{Au}/(E_r)_{Au}) + (V_{Si}/(E_r)_{Si})\}^{-1} \tag{4.4}$$

where H', H_{Au} and H_{Si} are the hardness of the Au-Si film, pure Au film and single crystal Si, respectively, E'_r, $(E_r)_{Au}$ and $(E_r)_{Si}$ are the reduced elastic moduli of the Au-Si film, pure Au film and single crystal Si, respectively, and V_{Au} and V_{Si} are the volume fractions of the co-evaporated Au and Si, respectively, which can be determined based on their atomic volume and percentages [115].

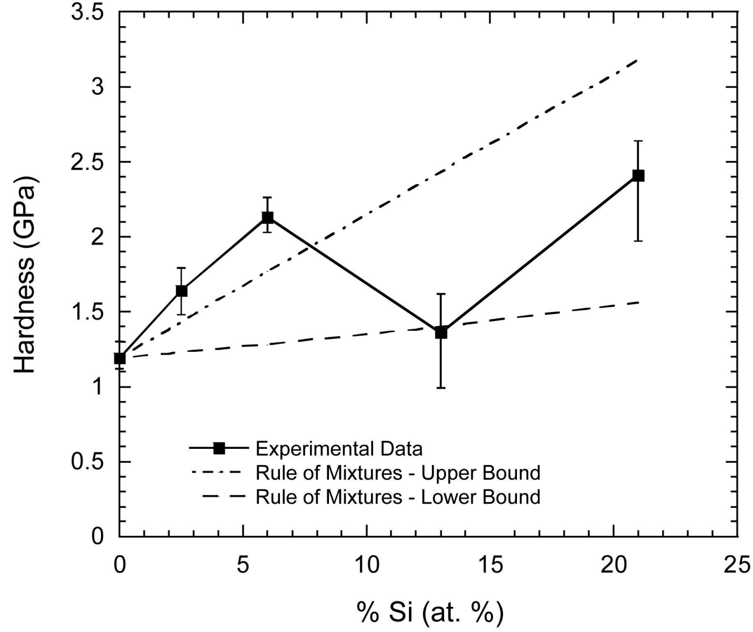

Figure 4.22: The effect of Si content on the hardness of pure Au and Au-Si films. Shown for comparison are the upper and lower bound rule of mixture predictions obtained from Eqns. (4.1) through (4.4).

The subscripts 'u.b.' and 'l.b.' represent the upper bound and lower bound of the film properties predicted by the rule of mixtures, respectively, as given by H.S. Kim [115]. The upper bound of the rule of mixtures is based upon the assumption, first proposed by Voigt in 1928 [116], that the constituents undergo the same strain in response to an applied load and is also known as the iso-strain or Voigt model [115, 117]. The lower bound of the rule of mixtures is based upon the assumption, first proposed by Reuss in 1929 [116], that the constituents undergo the same stress in response to an applied load and is also known as the iso-stress or Reuss model [115, 117].

It is shown in Figure 4.24 that the hardness is increased to a level above the upper bound of the rule of mixtures for Au films containing low amounts of Si (2.5 - 6 at. %). This suggests that an additional mechanism(s) is responsible for the increase in film hardness besides the intrinsic hardening from the co-deposited Si. The hardness does not continue to increase with increasing Si content greater than 6 at. % and is seen to lie within the rule of mixtures prediction. The hardness of the Au/13 at. % Si film is directly at the lower bound suggesting that the material follows the iso-stress model. However, the optical microscope images showing film buckling suggest that the relieving of residual compressive stresses and poor film adhesion are responsible for the low measured hardness.

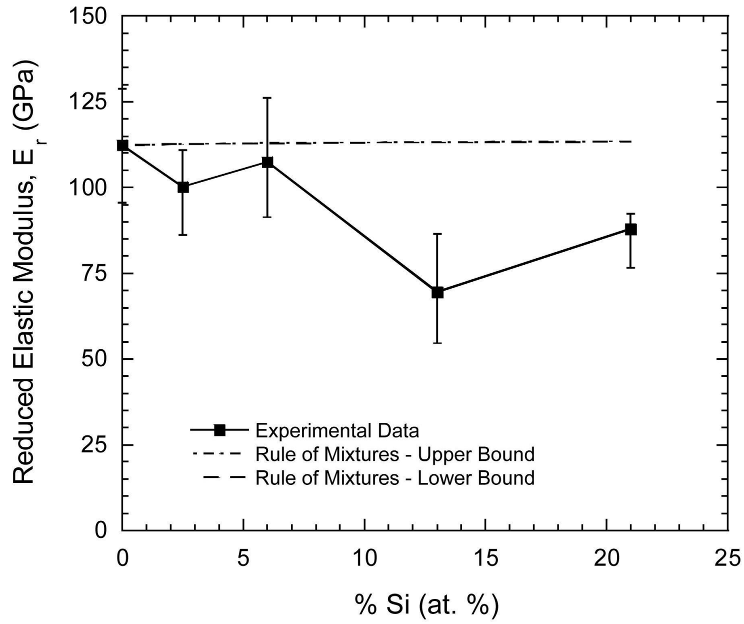

Figure 4.23: The effect of Si content on the reduced elastic modulus of pure Au and Au-Si films. Shown for comparison are the upper and lower bound rule of mixture predictions (upper and lower bound overlap) obtained from Eqns. (4.1) through (4.4).

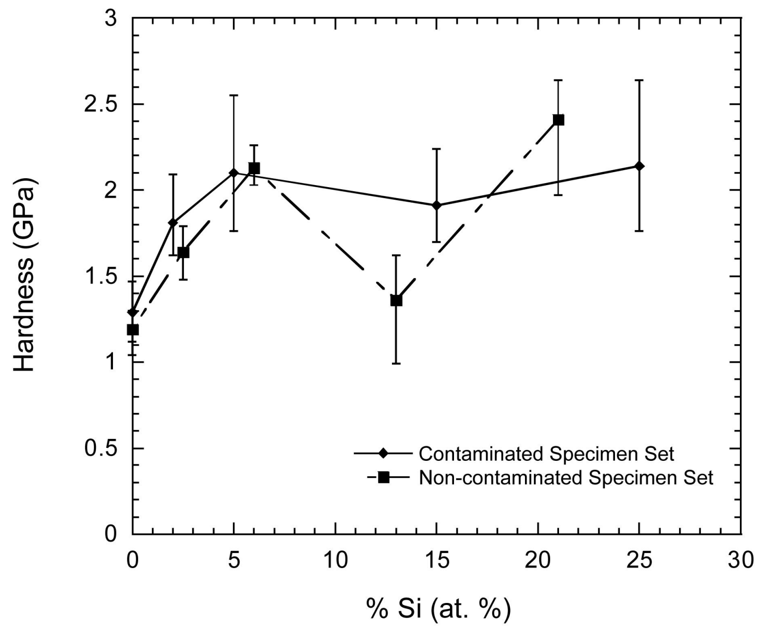

Figure 4.24: Comparison of the hardness of the contaminated versus non-contaminated pure Au and Au-Si films.

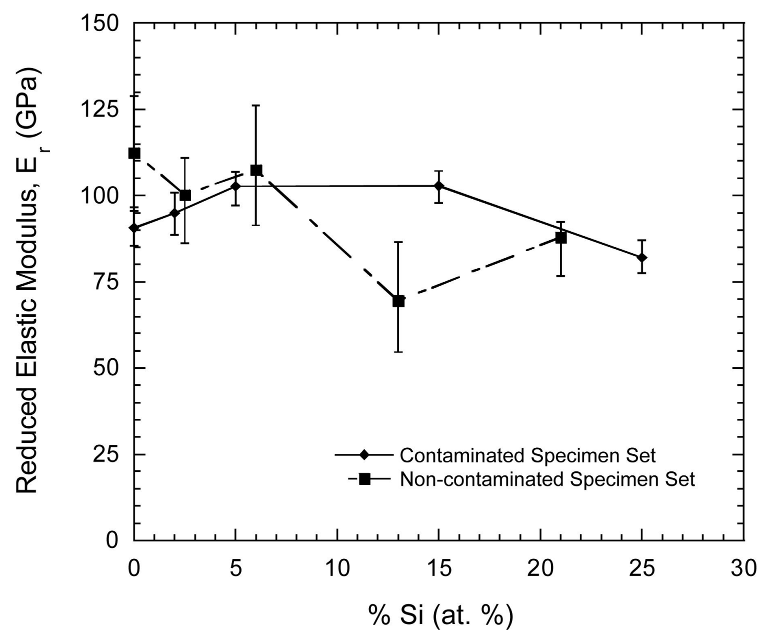

Figure 4.25: Comparison of the reduced elastic modulus of the contaminated versus non-contaminated pure Au and Au-Si films.

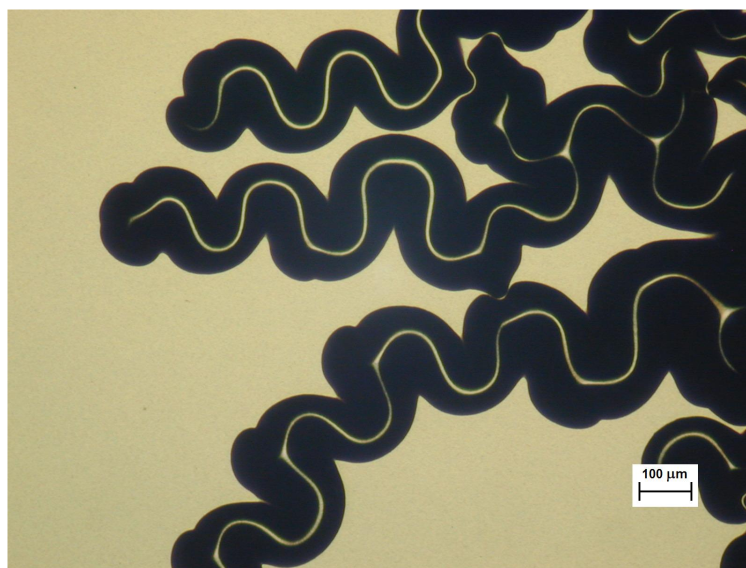

Figure 4.26: Optical image showing "telephone cord" buckling of the Au/13 at. % Si thin film. The line at the center of each "telephone cord" buckle is the apex of the delamination.

The reduced elastic modulus is seen to decrease below the rule of mixtures prediction as the Si content is increased.

Theories on the additional mechanism(s) responsible for these observations will be discussed further in the following sections.

Electrical properties

Four-point probe measurements were conducted on all films and the values measured for the resistivity are shown in Table 4.6. The resistivity of the pure Au film was about 3.18 $\mu\Omega$-cm, higher than the values measured for Au films discussed in Section 4.1.2 and the value of 2.35 $\mu\Omega$-cm reported for bulk Au [111]. The increased resistivity in these pure Au films, compared to those in Section 4.1.2, could be due to the slightly higher surface roughness. The resistivity increased nearly linear from 5.58 - 38.15 $\mu\Omega$-cm as the Si content increased from 2.5 - 21 at. %, respectively. The linear trend in resistivity is shown in Figure 4.27.

Specimen	**Resistivity ($\mu\Omega$-cm)**	**Std. Dev. ($\mu\Omega$-cm)**
Pure Au	3.18	0.01
Au/2.5 at. % Si	5.58	0.01
Au/6 at. % Si	12.00	0.08
Au/13 at. % Si	19.46	0.13
Au/21 at. % Si	38.15	0.13

Table 4.6: Average resistivity values for the pure Au and Au-Si films consisting of Au co-evaporated with 2.5, 6, 13, or 21 at. % of Si.

Material structure

XRD measurements were performed to determine the crystal structure of the pure Au and Au-Si thin films and the diffraction patterns are shown in Figures 4.28 through 4.32. The diffraction peaks are labeled with their equivalent interplanar spacing (also known as the d-spacing), and any identifiable peaks are also labeled with the respective element and Miller Index (or (hkl) value).

The first diffraction pattern, shown in Figure 4.28, was obtained for the pure Au thin film. The strong peak located at the angle, $2\theta = 38.2°$ corresponds to a d-spacing of about 2.35 Å. This peak represents the (111) lattice plane for a face-centered cubic (fcc) polycrystalline Au structure with lattice parameter a = 4.08 Å [118] and is present in the remaining patterns. However, it

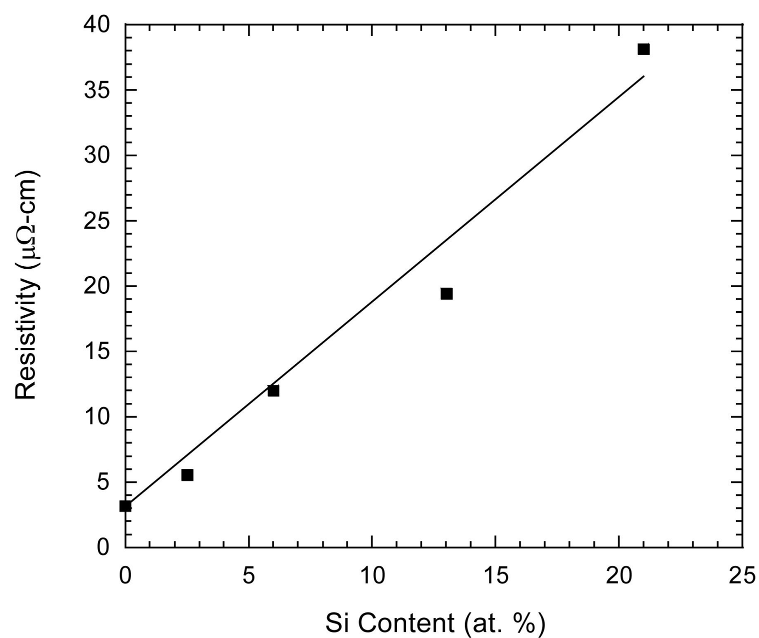

Figure 4.27: The effect of Si content on the resistivity of Au thin films.

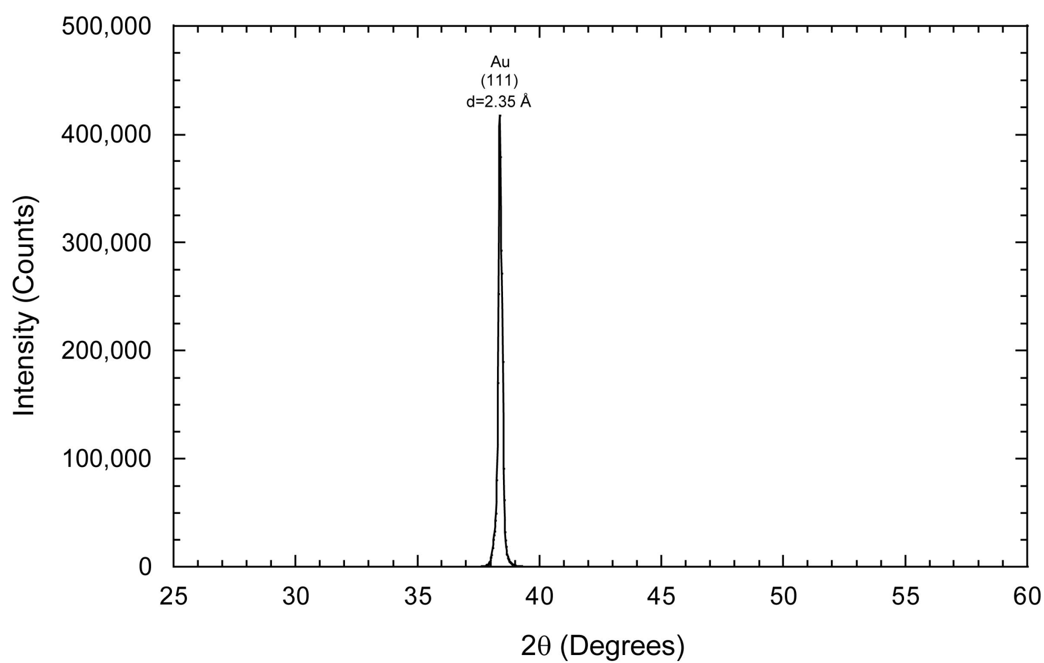

Figure 4.28: X-ray diffraction pattern for the pure Au thin film.

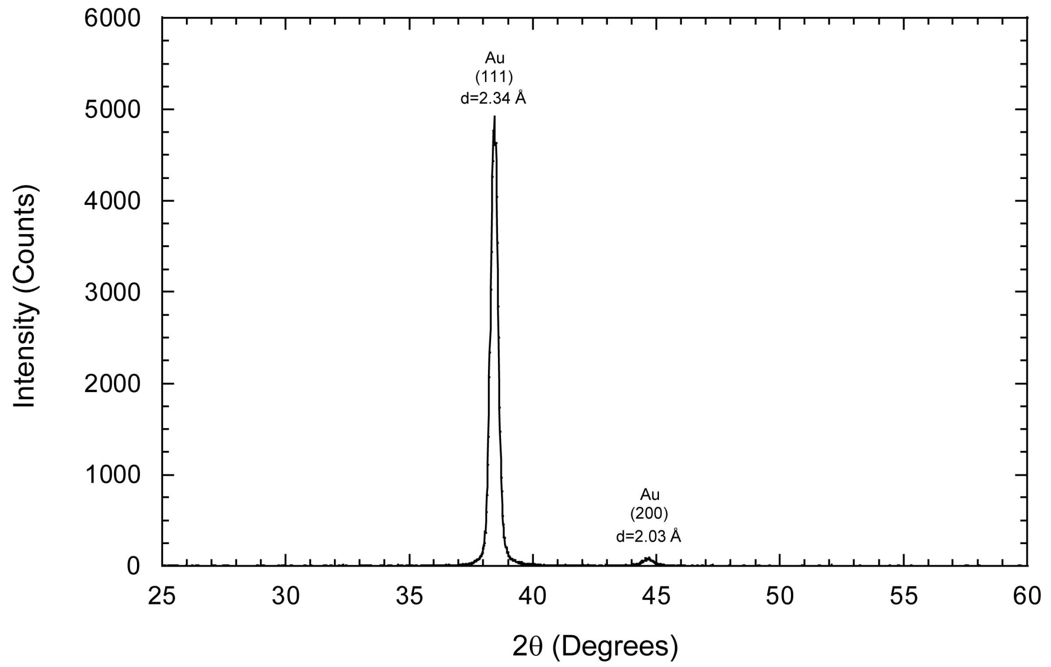

Figure 4.29: X-ray diffraction pattern for the Au thin film co-evaporated with 2.5 at. % Si.

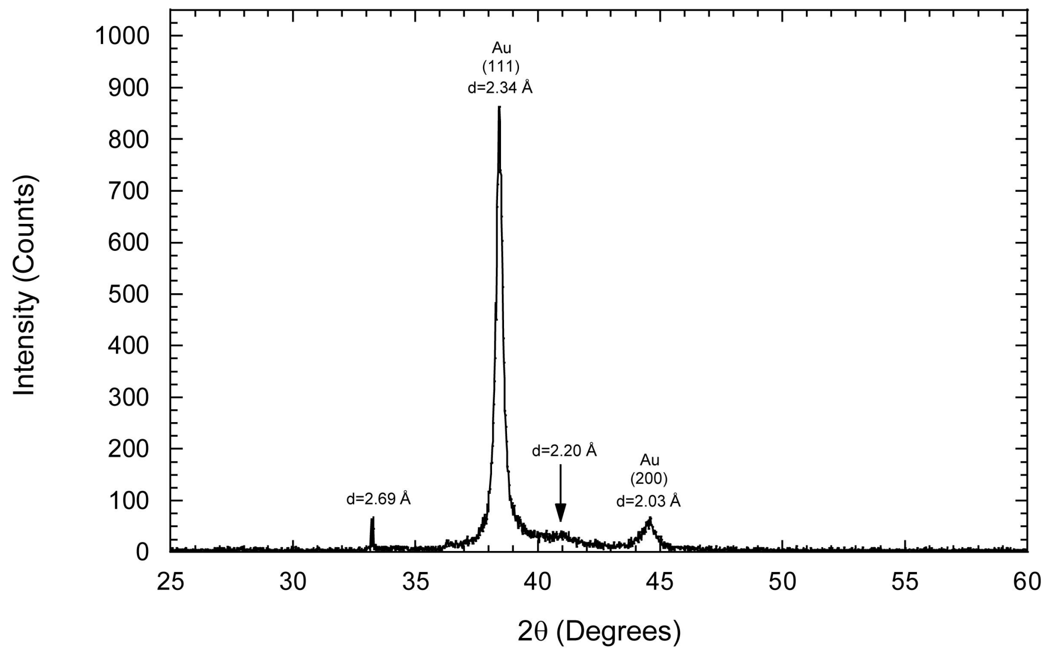

Figure 4.30: X-ray diffraction pattern for the Au thin film co-evaporated with 6 at. % Si.

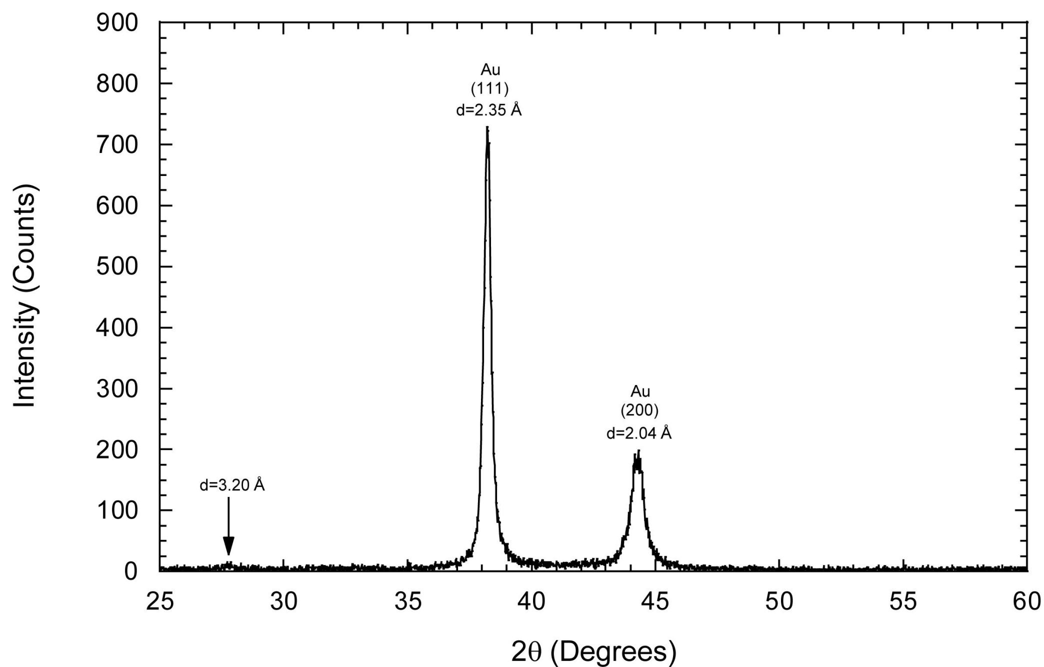

Figure 4.31: X-ray diffraction pattern for the Au thin film co-evaporated with 13 at. % Si.

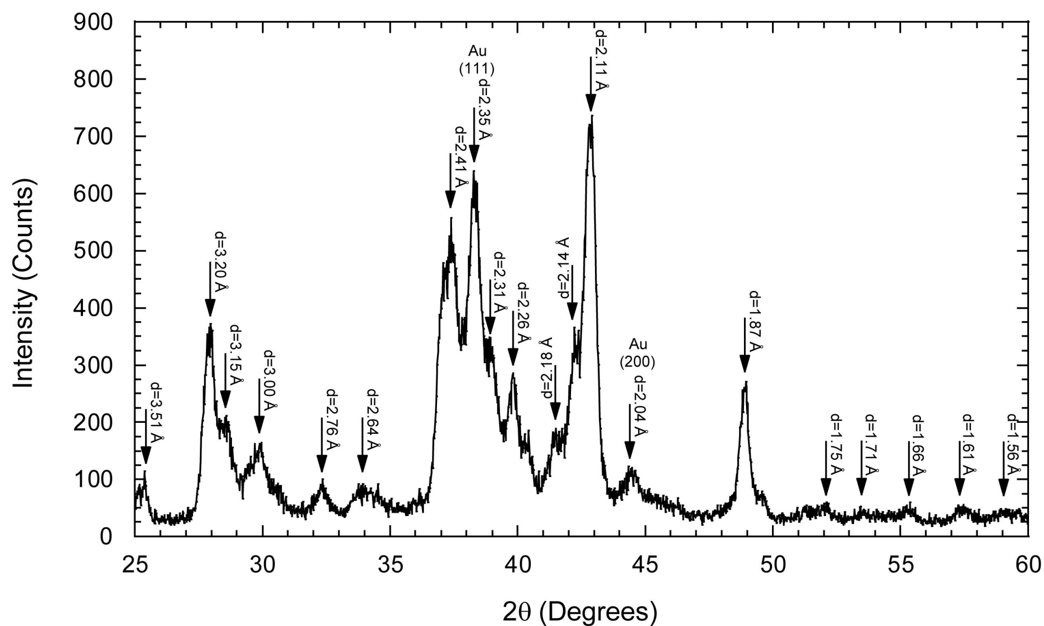

Figure 4.32: X-ray diffraction pattern for the Au thin film co-evaporated with 21 at. % Si.

decreases in intensity and increases in broadness as the Si concentration is increased. The decrease in peak intensity indicates a shift in the material's grain orientation. Peak broadening can occur due to factors such as instrumental effects, decrease in crystal/grain size and/or due to strain in the lattice [89].

The average grain size of the films was found to be approximately 51, 17, 18, 18 and 20 nm for the pure Au and Au-Si films with 2.5, 6, 13 and 21 at. % Si, respectively.

The diffraction patterns indicate that the intensity ratio between the (111) and the (200) Au peaks, $I_{(111)}/I_{(200)}$ decreases as the Si content is increased, indicating a change from the (111) orientation to the (200) orientation occurring in the films. A plot of the Au peak intensity ratio $I_{(111)}/I_{(200)}$ versus Si content is shown in Figure 4.33.

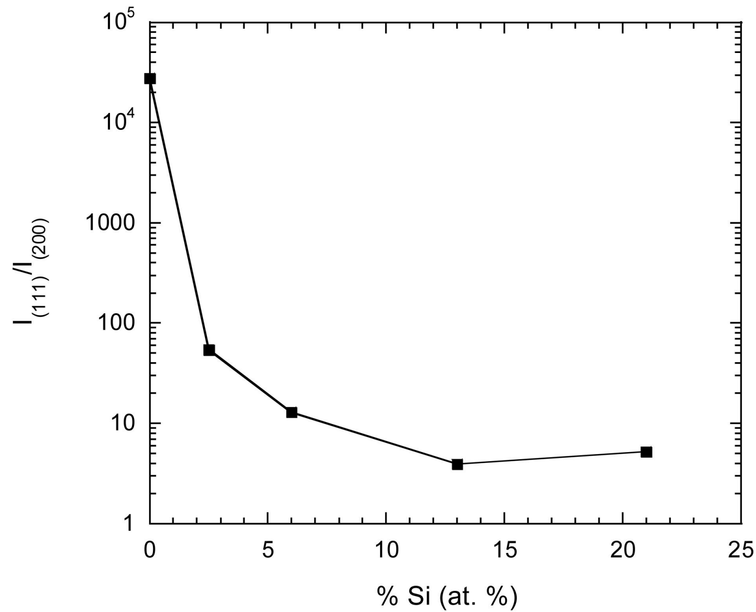

Figure 4.33: Variation of Au peak intensity ratio, $I_{(111)}/I_{(200)}$ with Si content.

A similar decrease in $I_{(111)}/I_{(200)}$ has been reported by Tang et al. [119, 120] for annealed Au films deposited by electroplating. It was proposed that atom transport occurred, either due to the heat treatment and/or residual compressive stress gradients, at the boundary of (111) and (200) grains resulting in the preferential growth of the (200) oriented grains. As $I_{(111)}/I_{(200)}$ decreased, an increase in the thin film residual compressive stress was also measured. This has also been reported to occur in evaporated Cu films [121] and sputtered Al films [122].

According to Zhang et al. [123], the difference between stresses in Au grains oriented in the (111) and (200) planes is $\Delta\sigma^{(111)} - \Delta\sigma^{(200)} = (18.87 - 7.91)$ MPa $= 10.96$ MPa. If compressive stresses are

introduced into the film, which for the films investigated in this work could be due to the presence of Si, the stress difference could lead to large compressive stress gradients at the boundaries of (111) and (200) oriented grains [123]. Tang et al. [119, 120] reported that these large stress gradients could cause atom transport to occur at the grain boundary, schematically shown in Figure 4.34. Thus, it is plausible that this mechanism would lead to growth of (200) oriented grains and explain the change in $I_{(111)}/I_{(200)}$ observed in the XRD measurements presented here. Furthermore, XRD measurements indicated an almost exclusive (111) orientation for the pure Au film. Therefore, the biaxial stresses present from co-evaporation with Si could have been minimized and an increase in the (200) orientation would have provided a system with minimized energy, due to the lower strain energy of the (200) plane, and a slip system more favorable for deformation and accommodation of strain [120].

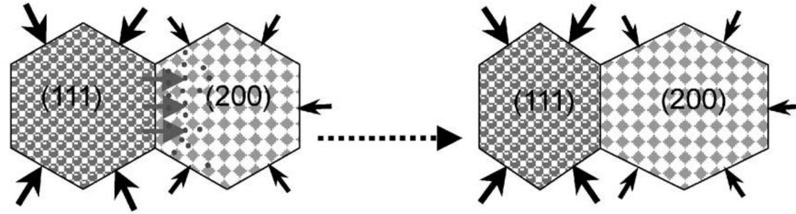

Figure 4.34: Schematic showing atom transport, in polycrystalline FCC films, occurring across a grain boundary from a (111) grain to a (200) grain resulting from a large compressive stress gradient [119].

Unknown peaks were observed in the Au/6 at. % Si and Au/13 at. % Si films which have not been reported in the literature or the ICDD PDF database. No crystalline Si peaks were observed in the Au-Si films, suggesting that the Si is amorphous. It has been reported that cooling rates in liquid-quenched Au-Si can be high enough to allow for near or complete suppression of Si crystal formation [124].

The reduction in grain size suggests that strengthening in the films can be partially attributed to the Hall-Petch effect. A plausible explanation for this reduction could be pinning of the Au grains by the dispersed Si particles, which has been reported to occur in Ta particle strengthened Au films [68] and Si particle strengthened Al films [62].

The deviation from the hardness increase for a Si content greater than 6 at. % Si, shown in Figure 4.22, could be partly related to the increase in the (200) orientation. Roy et al. [121] reported a decreased hardness in the (200) planes compared to the (111) planes for evaporated Cu films. The increased hardness was attributed to stronger elastic constants in the (111) plane. Fur-

thermore, the increased (200) orientation could also be responsible for the observed decrease in reduced elastic modulus. Based on the compliance constants given for Au as $S_{11} = 2.355\,x\,10^{-11}$ Pa, $S_{12} = -1.0814\,x\,10^{-11}$ Pa and $S_{44} = 2.4096\,x\,10^{-11}$ Pa [103], the elastic modulus of Au can be predicted for the (111) and (200) planes through the following equation [72]:

$$E_{hkl} = \left\{ S_{11} - 2\left[(S_{11} - S_{12}) - \frac{1}{2}S_{44}\right](l^2m^2 + m^2n^2 + l^2n^2) \right\}^{-1} \tag{4.5}$$

where S_{11}, S_{12}, S_{44} are previously defined and l, m, n are the corresponding direction cosines for each plane in the cubic lattice. From Eqn. (4.5) the estimated elastic modulus values for polycrystalline Au are $E_{(111)} = 115$ GPa and $E_{(200)} = 43$ GPa. Therefore, it is plausible that the pure Au film with the preferred (111) orientation would have a much higher reduced elastic modulus and that an increasing degree of (200) orientation could effectively cause the film's reduced modulus to decrease, as shown in Figure 4.23.

The diffraction pattern, shown in Figure 4.32 for the Au/21 at. % Si film, exhibits numerous intense, unidentifiable peaks which suggest the formation of an unknown crystalline Au-Si phase.

Metastable Au-Si phases have been previously reported throughout the literature and have been the subject of extensive work [69, 124–138] since the first reported observation by Klement et al. in 1960 [139]. While Au and Si are almost completely immiscible in the solid state [69], Klement et al. [139] first demonstrated that Au-Si alloys could be formed by rapidly quenching a liquid mixture (a method known as "splat cooling" [126]) of Au with 25 at. % Si to form a metastable amorphous Au-Si alloy which crystallized at room temperature. The formation of these phases was attributed to the high cooling rates and it has been reported that metastable Au-Si phases can form at cooling rates greater than 10^6 K/s [140]. According to Liebermann [141], vapor deposition methods such as sputtering and electron-beam evaporation allow for material cooling rates on the order of 10^8 K/s and rates as high as 10^{10} K/s have been estimated [2], suggesting the feasibility of observing metastable Au-Si phases in the films investigated here. Two prior studies by Dhere and Loral [134] and Robison et al. [136] have investigated co-evaporated Au-Si and both reported the observation of metastable phases.

A detailed summary of the various reported structures of Au-Si phases is given by Ashtikar and Sharma [137]. There have been a total of nine different types of metastable Au-Si alloys reported, having cubic (fcc or bcc), orthorhombic or hexagonal type crystal structures [137]. While several of these reported phases have d-spacings which closely match those measured for the Au/21 at. % Si film, the experimental data is most consistent with a fcc β-Mn-type structure with a = 6.750 Å, first reported by Suryanarayana and Anantharaman [129, 142] and later by Gaigher and Van der

Berg [133]. A comparison of the d-spacings reported for the β-Au-Si phase with those measured for the Au/21 at. % Si film is shown in Table 4.7.

β-Mn-type Au-Si [129, 142]			**β-Mn-type Au-Si [133]**	**This Work**
hkl	$d_{calc.}$	$d_{obs.}$	$d_{calc.}$	$d_{obs.}$
100	6.750	6.526	6.67	—
110	4.776	4.677	4.75	—
111	3.897	3.905	3.86	—
200	3.375	3.365	3.33	—
210	3.018	2.976	2.99	3.00
211	2.755	2.750	2.76	2.76
220	2.388	2.385	2.40	2.41
300	2.250	2.250	2.24	2.26
221	2.250	2.250	2.24	2.26
310	2.134	2.137	2.11	2.14 & 2.11
222	1.948	1.948	—	—
320	1.872	1.873	—	1.87
321	1.804	1.805	—	—
400	1.688	1.708	—	1.71
410	1.637	1.639	—	1.66
322	1.637	1.639	—	1.66
330	1.592	1.590	—	1.61
411	1.592	1.590	—	1.61

Table 4.7: Comparison of the measured d-spacings for the Au/21 at. % Si film with those reported in the literature for a fcc β-Mn-type structure [129, 133, 142].

Comparing the experimental values shown in Table 4.7, the data suggests that a metastable Au-Si phase has formed in this film with a composition similar to the fcc β-Mn-type structure. However, while the d-spacings were consistent with this structure, the measured intensities did not compare as well. The most intense peak shown in Figure 4.32, centered at about $2\theta = 42.6°$ (d = 2.12 Å) has not been reported in the literature for Au-Si films. Also, throughout the studies reported for Au-Si films [142–149], a very strong peak was reported at about $2\theta = 40.0°$ (d ≈ 2.25 Å) . The intensity of this peak was fairly weak to medium for the Au/21 at. % Si film. One plausible explanation for

this lower intensity is that the XRD measurements were conducted after dissociation had already initiated. The structure and material properties of rapidly cooled samples can depend on the type of preparation method used [141], suggesting that the unidentifiable Au-Si compound observed in this study would not be unexpected. Also, Dhere and Loural note that the precise structure is influenced by local differences in material composition and atomic arrangement, annealing conditions and cooling rate [134], thus explaining the abundance of different metastable Au-Si structures reported in the literature.

The metastability of the unknown phase was shown experimentally by performing a second XRD measurement on the Au/21 at. % Si film after it was stored at room temperature (RT) for approximately 8 weeks. The second measurement, shown in Figure 4.35, indicates that the unknown Au-Si phase has almost completely dissociated, as evident by the almost complete dissapearance of the unidentifiable peaks. The average grain size was found to increase from 20 - 43 nm. The (111) Au peak has increased in intensity and only two peaks at approximately $2\theta = 42.6°$ (d = 2.12 Å) and $2\theta = 48.6°$ (d = 1.87 Å) remain. The slight shoulder present at the base of the (111) Au peak (not labeled in Figure 4.35) could represent the unknown peak located at $2\theta = 37.3°$ (d = 2.41 Å) with lower intensity.

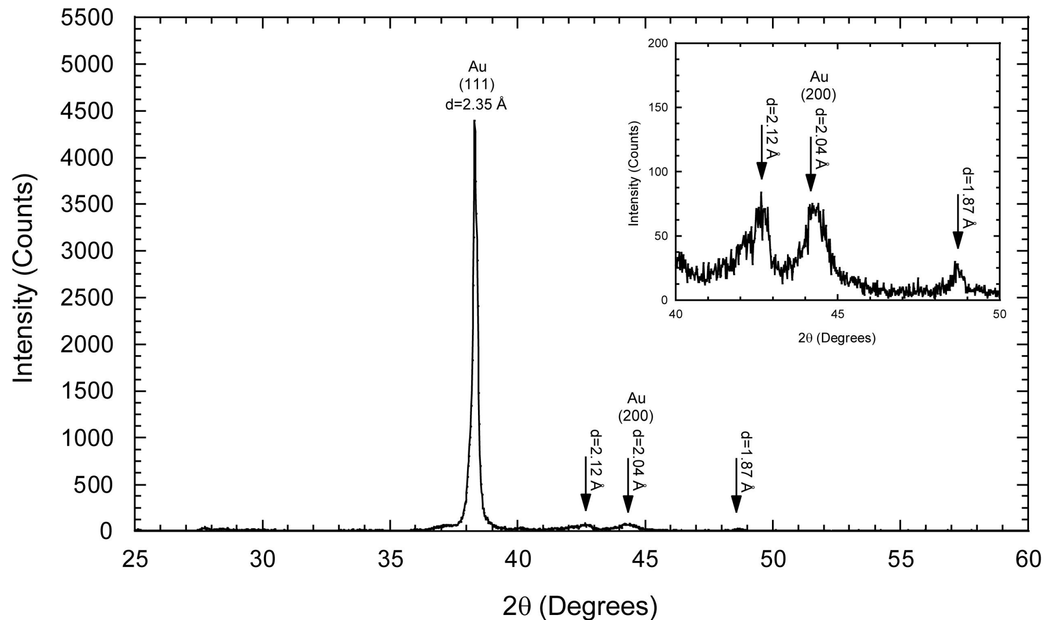

Figure 4.35: X-ray diffraction pattern for the Au thin film co-evaporated with 21 at. % Si, measured after storing the specimen for approximately 8 weeks at RT.

The surface topography and mechanical properties of the film also changed after the storage

period. The average surface roughness increased by about 30% from 5.5 - 7.2 nm Ra. Numerous craters, approximately 20 - 100 μm in diameter, were observed with the optical microscope during the 10th week of the RT storage period. Delamination, which initiated at the edges of the craters, was observed with the optical microscope during the 14th week of the storage period. Optical images of the film surface are shown in Figure 4.36. AFM measurements indicated that the film surface around the craters exhibited a nodular type topography similar to the surface prior to aging. Johnson and Johnson [69] reported that dissociation of the metastable Au-Si phase into Au and Si must be accompanied by a volume expansion. Such an expansion could introduce compressive stresses into the film and thus explain the observation of film buckling occuring at the edge of each crater [97]. The hardness and reduced elastic modulus, measured at a normalized contact depth of about 0.10 during the 12th week of RT storage, were found to decrease by approximately 32% from 2.41 - 1.65 GPa and 53% from 88 - 41.5 GPa, respectively.

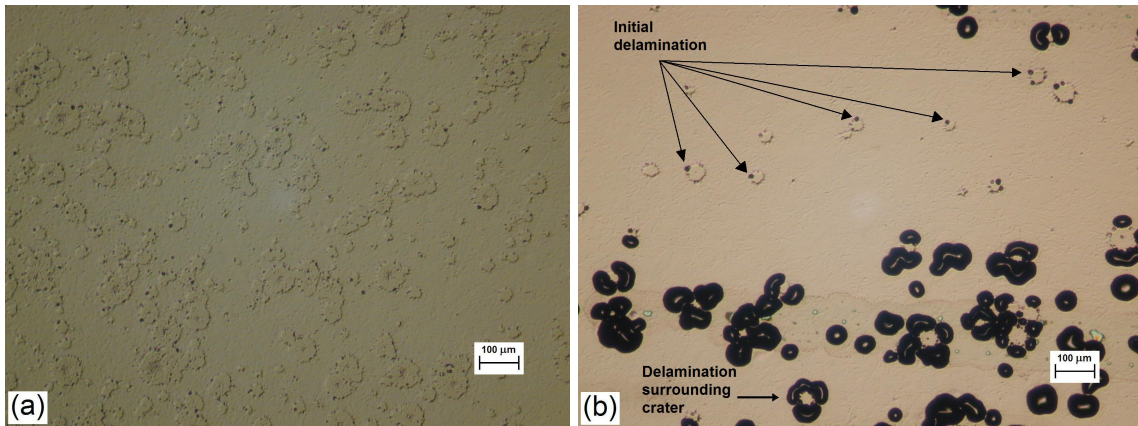

Figure 4.36: Optical images showing changes in the surface topography including: (a) the presence of numerous craters on the surface and (b) film delamination occurring at the edges of the craters of the Au thin film co-evaporated with 21 at. % Si, obtained after approximately 10 and 14 weeks of RT storage, respectively.

The RT dissociation of metastable Au-Si phases has been reported in the literature. In a study by Robison et al. [136], 1000 nm thick Au-Si films were prepared by co-depositing Au with 50 at. % Si and annealed at temperatures of 100 - 250 °C for 5 minutes to compare with the as-deposited films. XRD measurements indicated numerous peaks which matched those previously reported for Au_2Si and it was proposed that the structure was most likely fcc with a = 19.50 Å. The structure of the co-deposited films was found to be similar to previous work, in which metastable Au-Si films were prepared by rapid quenching of liquid Au-Si melts. To demonstrate the metastability of the

Au_2Si phase, XRD measurements were conducted on specimens stored for one month at RT under vacuum. In all specimens, with the exception of the as-deposited specimen, the Au_2Si phase was undetectable and appeared to have dissociated. While only one additional study has been found showing evidence of a metastable Au-Si alloy formed through co-evaporation [134], only Robison et al. have reported RT dissociation [136].

The RT dissociation of metastable Au-Si phases has been reported elsewhere, however, the investigated films were prepared by liquid quenching methods. Johnson and Johnson [69] (with earlier similar work [150]), reported dissociation of the Au_3Si phase (prepared from Au with a Si content of 4 - 14 at. %) after specimens were stored for 98 to 111 months at RT. The work by George et al. [124] is the only known reported RT dissociation of an as-deposited metastable Au-Si phase in an aging time period on the order of that used in this study. In the previously discussed studies, the dissociation was reported to occur after post-deposition heat treatment, or after a period of several months at RT [69]. George et al. [124] reported that in liquid quenched Au-25 at. % Si specimens, Au_3Si peaks measured by XRD dissapeared (only peaks from the polycrystalline Au film were reported, similar to the results shown in Figure 4.35) after RT storage for several weeks.

TEM measurements were performed to investigate the underlying material structure of the Au-Si films. An image obtained for an Au film with a nominal Si concentration of 25 at. % is shown in Figure 4.37(a)-(c). Figure 4.37(a) shows the nanocrystalline Au grain structure with a dispersion of amorphous Si particles. The average grain and particles sizes were found to be about 18 nm and 1 - 5 nm, respectively. The measured average grain size is consistent with XRD measurements for the as-deposited Au/21 at. % Si film. The selected area diffraction pattern, shown in Figure 4.37(c), shows strong (111) Au, (220) Au and (200) Au reflections indicating multiple grain orientations as well as a lack of Si reflection suggesting an amorphous structure. The (220) reflection is reported to occur at $2\theta = 64.6°$ [118], which is outside of the 2θ scan range (25° - 60°) used for the XRD measurements explaining the lack of detection for those experiments. The Si particles are located at the Au grain boundaries suggesting that the decrease in grain size, measured by XRD, could be partly due to pinning from the dispersed Si particles. A high-resolution image of a 3 nm Si particle at the grain boundary of two (111) oriented Au grains is shown in Figure 4.37(b).

The measured average Si particle size and separation distance were used to estimate the stress required to displace a dislocation past a line of Si particles, based on the Orowan mechanism. Using Eqn. (2.8), the shear modulus G, is determined for the Au film from the elastic modulus (determined from nanoindentation) and the Poisson's ratio for the Au film [94] by the equation, $G = E/2(1+\nu) = 100.5$ GPa$/2(1+0.43) = 35$ GPa [72]. The magnitude of the Burgers vector is estimated from the

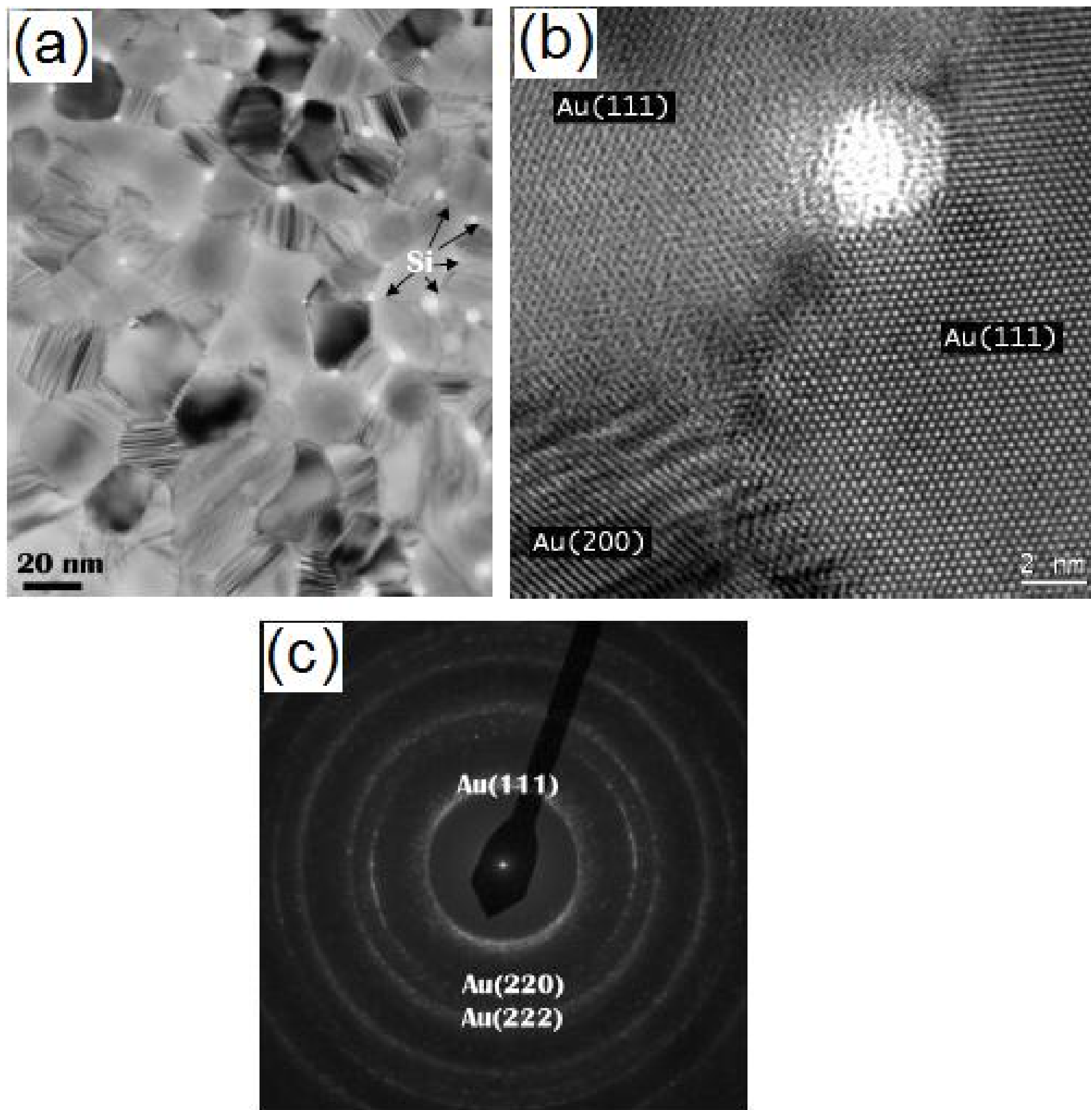

Figure 4.37: Selected TEM images showing the microstructure of the Au-Si film with a nominal Si concentration of 25 at. %. (a) TEM image showing the nanocrystalline grain structure of the Au with approximately 1 - 5 nm diameter Si particles located at the Au grain boundaries. (b) High-Resolution TEM (HRTEM) image showing a 3 nm Si particle at the grain boundary of two (111) oriented Au grains. (c) Selected area diffraction pattern showing multiple Au grain orientations.

interatomic spacing of Au, and assuming a hard-sphere model, is equal to the atomic diameter of Au, 0.29 nm [76]. The average particle radius r and spacing λ are estimated from the TEM image shown in Figure 4.37 to be about 1.5 nm and 17 nm, respectively. Using Eqn. (2.8), the increase in yield strength for the Au-Si film resulting from the Orowan mechanism is estimated to be

$$\sigma_{Orowan} = \frac{(0.13)(35GPa)(0.29nm)}{17nm} \, ln \, \frac{1.5nm}{0.29nm} \tag{4.6}$$

and from the above equation, $\sigma_{Orowan} \approx 130$ MPa. Therefore, $H_{Orowan} \approx 0.4$ GPa, where H_{Orowan} is the predicted hardness increase of the Au-Si film resulting from the Orowan hardening mechanism. The maximum and minimum Orowan stresses can be determined from the range of Si particle size and distributions. Eqn. (2.8) predicts that the Orowan stress will be minimum when the Si particle radius r is minimum and the particle spacing λ is maximum, and from Figure 4.37, are estimated to be about 0.5 nm and 44 nm, respectively. Similarly, Eqn. (2.8) also predicts that the Orowan stress will be maximum when the Si particle radius r is maximum and the particle spacing λ is minimum, and from Figure 4.37, are estimated to be about 2.5 nm and 8 nm, respectively. From Eqn. (2.8), these values lead to an estimated hardness range, $H_{Orowan} \approx 0.05$ GPa - 1.07 GPa.

This estimate predicts that, assuming the same Si content for the TEM specimens as the 21 at. % Si film investigated by nanoindentation, the increase in hardness due to the Orowan mechanism would for about 4 - 88% of the overall hardness increase measured for the Au/21 at. % Si film, with an average increase of 33% (based on the average particle size and spacing).

The estimated H_{Orowan} range indicates that additional mechanisms, such as the Hall-Petch effect, may be responsible for the measured hardness increase.

Chapter 5

Conclusions and Proposed Future Work

5.1 Conclusions

An investigation of the material properties of electron-beam evaporated polycrystalline Au films and the effect of Si content on the material properties and structure of co-evaporated Au-Si films has been performed. Atomic Force Microscopy (AFM), nanoindentation and four-point probe were utilized to investigate the surface topography, mechanical properties and resistivity of these films, respectively. Furthermore, X-ray Diffraction (XRD) and Transmission Electron Microscopy (TEM) measurements were performed to investigate the material crystallography and structure.

The conclusions from the polycrystalline Au baseline investigation are:

Variable deposition rate investigation

1. The surface topography of pure Au films was investigated and the surfaces of the films showed small, uniformly sized nodules. The surface roughness was found to decrease with increasing deposition rate.

2. The hardness and elastic modulus of the films ranged from 1 - 1.5 GPa and 80 - 130 GPa, respectively. Both were found to increase with increasing depth of penetration indicating the effect of the underlying Si substrate.

The effect of the adhesion layer and heat treatment

1. Surface topography measurements were conducted on as-deposited and annealed Au films deposited on Ti or Cr adhesion layers and the roughness was about 2.5 - 3.5 nm Ra. Surface cracks were observed in the annealed Au film with the Cr adhesion layer and it was suggested that the cracks formed as a result of diffusion of Cr toward the Au film surface, which has been reported for annealed Au films [96, 104, 105].

2. The hardness and elastic modulus were found to be about 0.9 - 1.9 GPa and 70 - 100 GPa, respectively, for all films. The hardness was seen to decrease with increasing normalized contact depth up to about 0.2, consistent with the indentation size effect. Both hardness and elastic modulus increased with increasing depth of penetration, at normalized contact depths greater than 0.2, due to the increased influence of the underlying Si substrate, as expected. Recognizing the variations associated with the measurements, no significant effect of the adhesion layer and heat treatment on the hardness or elastic modulus was identified. Pop-in was observed for both as-deposited and annealed Au films.

3. The resistivity of the films with the Ti adhesion layer was found to be 2.24 - 2.36 $\mu\Omega$-cm for the as-deposited and annealed films, respectively, and was consistent with bulk Au values [111]. The resistivity of the films with the Cr adhesion layer increased to 3.39 - 4.36 $\mu\Omega$-cm for the as-deposited and annealed films, respectively. The increased resistivity measured for the annealed Cr adhesion layer specimen was possibly affected by the diffusion of Cr into the Au film, which has been reported to lead to an increase in resistivity in Au films [96, 104, 105].

The conclusions from the Au-Si film investigation are:

Initial shakedown experiments

1. The surface roughness was slightly higher than the values measured for the initial Au baseline films. Unusual peaks and craters were observed on the surfaces of all films which was later attributed to carbon contamination occurring during the deposition process.

2. The hardness of the pure Au film was found to be about 1.1 GPa and increased by approximately 65 - 95% (1.81 - 2.14 GPa) by the addition of 2 - 25 at. % Si, respectively. The effect of heat treatment was investigated, yet due to the large error bars present in the measurements, no significant effect of the annealing on the hardness could be identified and therefore heat treatment was not further pursued.

Secondary investigation

1. The surface roughness was found to vary throughout the Si content range. The surface roughness for the pure Au film was found to be 3.4 nm Ra, consistent with the prior set. The roughness increased for all other films from 5.5 - 19.1 nm Ra for the 21 at. % Si and 13 at. % Si films, respectively. There appeared to be no direct correlation between Si concentration and roughness. The cause of the variation in surface roughness was unclear.

2. The hardness of the pure Au film was found to be about 1.2 GPa and increased by approximately 40 - 80% (1.64 GPa - 2.13 GPa) by the addition of 2.5 and 6 at. % Si, respectively, and increased approximately 102% to 2.41 GPa by the addition of 21 at. % Si. However, the hardness of the Au/13 at. % Si film increased by only 14% to 1.36 GPa. The reduced elastic modulus for the pure Au film found to be approximately 112 GPa. This corresponded to an elastic modulus of approximately 100 GPa. The reduced elastic modulus was seen to follow a trend similar to the hardness with increasing Si content. To investigate the effect of the carbon contamination on the original film properties, both measurements were compared simultaneously. The data compared well, when taking into account the error, for all Si concentrations except 13 at. % Si. The low hardness observed for this film could be attributed to the relieving of residual compressive stresses, which became evident after film buckling was observed on approximately 10% of the film surface which has been reported to occur due to residual stresses in thin films [97].

3. The film resistivity increased nearly linear from 5.58 - 38.15 $\mu\Omega$-cm as the Si content increased from 2.5 - 21 at. %, respectively.

4. XRD measurements indicated that the film structure consisted of polycrystalline Au grains oriented primarily in the (111) plane and secondarily in the (200) plane. No crystalline Si peaks were observed in the Au-Si films, suggesting that the Si is amorphous. The intensity ratio between the (111) and the (200) Au peaks, $I_{(111)}/I_{(200)}$ decreased as the Si content increased, indicating a change from the (111) orientation to the (200) orientation occurring in the films. A similar decrease in $I_{(111)}/I_{(200)}$ has been reported in the literature [119–122] and attributed to an increase in the thin film residual compressive stress. It was suggested that a deviation from the hardness increase observed for a Si content greater than 6 at. % Si was partly related to the increase in the (200) grain orientation. The average grain size of the films was found to be approximately 51, 17, 18, 18 and 20 nm for the pure Au and Au-Si films with 2.5, 6, 13 and

21 at. % Si, respectively. The reduction in grain size suggested that strengthening in the films could be partially attributed to the Hall-Petch effect. The diffraction pattern for the Au/21 at. % Si film exhibited numerous intense, unidentifiable peaks which suggested the formation of an unknown crystalline Au-Si phase. The metastability of the unknown phase was shown experimentally by performing a second XRD measurement on the Au/21 at. % Si film after it was stored at room temperature (RT) for approximately 8 weeks. The measurement indicated that the unknown Au-Si surface phase had almost completely dissociated. The average grain size was found to increase from 20 - 43 nm. The average surface roughness, increased by about 30% from 5.5 - 7.2 nm Ra and the hardness and reduced elastic modulus decreased by approximately 32% from 2.41 - 1.65 GPa and 53% from 88 - 41.5 GPa, respectively after 12 weeks of RT storage.

5. TEM measurements, conducted on a Au/25 at. % Si specimen, showed the nanocrystalline grain structure of the Au, with an average grain size of 18 nm (consistent with the XRD measurement), with a dispersion of amorphous Si particles approximately 1 - 5 nm in diameter. From these results, the predicted hardness increase of the Au-Si film resulting from the Orowan hardening mechanism was estimated to be $H_{Orowan} \approx$ 0.05 GPa - 1.07 GPa representing approximately 4 - 88% of the overall hardness increase measured for the Au/21 at. % Si film, assuming the same Si content for the TEM specimens. The estimated H_{Orowan} range indicated that additional mechanisms, such as the Hall-Petch effect, may be responsible for the measured hardness increase.

5.2 Proposed Future Work

1. Determine if a thicker Ti adhesion layer could eliminate the loss of adhesion observed in the Au/13 at. % Si film and result in an increase in hardness.

2. Further investigate the effect of Si on the Au film properties through a larger concentration range by preparation of a compositionally graded film with continuous Si content from 0 - 50 at. %.

3. Investigate the modification of Au films by the introduction of Si-Ge particles, through simultaneous electron beam evaporation, which has been reported to lead to an order of magnitude finer dispersion of particles in Al alloy films compared to those with Si alone [63].

4. Further investigate the metastable Au-Si phase observed in the Au/21 at. % Si film by performing nanoindentation, surface topography, four-point probe and XRD measurements at more closely spaced time intervals after film deposition.

Bibliography

[1] K.D. Leaver and B.N. Chapman. *Thin Films*. The Wykeham Science Series. Wykeham Publications LTD., London, 1971.

[2] Milton Ohring. *The Materials Science of Thin Films*. Academic Press Inc., Boston, 1st edition, 1992.

[3] J.J. Yao. RF MEMS from a device perspective. *Journal of Micromechanics and Microengineering*, 10(4):R9–R38, 2000.

[4] R.A. Coutu, P.E. Kladitis, K.D. Leedy, and R.L. Crane. Selecting metal alloy electric contact materials for MEMS switches. *Journal of Micromechanics and Microengineering*, 14(8):1157–1164, 2004.

[5] S.T. Patton and J.S. Zabinski. Failure mechanisms of capacitive MEMS RF switch contacts. *Tribology Letters*, 19(4):265–272, 2005.

[6] H. Lee, R.A. Coutu, S. Mall, and K.D. Leddy. Characterization of metal and metal alloy films as contact materials in MEMS switches. *Journal of Micromechanics and Microengineering*, 16(3):557–563, 2006.

[7] J. Oberhammer and G. Stemme. Active opening force and passive contact force electrostatic switches for soft metal contact materials. *Journal of Microelectromechanical Systems*, 15(5):1235–1242, 2006.

[8] Yang-Tse Cheng, G. Drew, B. Gillispie, S.J. Simko, M.C. Militello, R.A. Waldo, and C.A. Wong. Vapor deposited thin gold coatings for high temperature electrical contacts. In *IEEE Holm Conference on Electrical Contacts*, pages 404–413, 1996.

[9] S. Majumder, N.E. McGruer, G.G. Adams, A. Zavracky, P.M. Zavracky, R.H. Morrison, and J. Krim. Study of contacts in an electrostatically actuated microswitch. In *IEEE Holm Conference on Electrical Contacts*, pages 127–132, 1998.

[10] J. Schimkat. Contact materials for microrelays. In *The Eleventh Annual International Workshop on Micro Electro Mechanical Systems*, pages 190–194, 1998.

[11] D. Hyman and M. Mehregany. Contact physics of gold microcontacts for MEMS switches. *IEEE Transactions on Components and Packaging Technologies*, 22(3):357–364, 1999.

[12] J. Schimkat. Contact measurements providing basic design data for microrelay actuators. *Sensors and Actuators A-Physical*, 73(1-2):138–143, 1999.

[13] S. Majumder, N.E. McGruer, G.G. Adams, P.M. Zavracky, R.H. Morrison, and J. Krim. Study of contacts in an electrostatically actuated microswitch. *Sensors and Actuators A-Physical*, 93(1):19–26, 2001.

[14] B.L. Pruitt, W.T. Park, and T.W. Kenny. Measurement system for low force and small displacement contacts. *Journal of Microelectromechanical Systems*, 13(2):220–229, 2004.

[15] S. Majumder, N.E. McGruer, and G.G. Adams. Adhesion and contact resistance in an electrostatic MEMS microswitch. In *IEEE International Conference on Microelectromechanical Systems*, pages 215–218, 2005.

[16] S.T. Patton and J.S. Zabinski. Failure mechanisms of capacitive MEMS RF switch contacts. *Tribology Letters*, 19(4):265–272, 2005.

[17] W.M. van Spengen. MEMS reliability from a failure mechanisms perspective. *Microelectronics Reliability*, 43(7):1049–1060, 2003.

[18] A. Bogozi, A.V. Datye, M. Brzhezinskaya, Y.S. Hijazi, J. Martinez, J. Noel, K.H. Wu, Y.A. Vlasov, and G.L. Larkins. Elastic modulus study of gold thin film for use as an actuated membrane in a superconducting RF MEM switch. *IEEE Transactions on Applied Superconductivity*, 15(2):980–983, 2005.

[19] C.W. Baek, J.M. Kim, Y.K. Kim, J.H. Kim, H.J. Lee, and S.W. Han. Mechanical characterization of gold thin films based on strip bending and nanoindentation test for MEMS/NEMS applications. *Sensors and Materials*, 17(5):277–288, 2005.

[20] C.W. Baek, Y.K. Kim, Y. Ahn, and Y.H. Kim. Measurement of the mechanical properties of electroplated gold thin films using micromachined beam structures. *Sensors and Actuators A-Physical*, 117(1):17–27, 2005.

[21] D.C. Miller, M.J. Talmage, and K. Gall. Incipient yielding behavior during indentation for gold thin films before and after annealing. *Journal of Materials Research*, 21(10):2480–2492, 2006.

[22] Y. Cao, D.D. Nankivil, S. Allameh, and W.O. Soboyejo. Mechanical properties of Au films on silicon substrates. *Materials and Manufacturing Processes*, 22(2):187–194, 2007.

[23] D. Hyman and M. Mehregany. Contact physics of gold microcontacts for MEMS switches. *IEEE Transactions on Components and Packaging Technologies*, 22(3):357–364, 1999.

[24] D. Hyman, J. Lam, B. Warneke, A. Schmitz, T.Y. Hsu, J. Brown, J. Schaffner, A. Walston, R.Y. Loo, M. Mehregany, and J. Lee. Surface-micromachined RF MEMS switches on GaAs substrates. *International Journal of RF and Microwave Computer-Aided Engineering*, 9(4):348–361, 1999.

[25] S. Kalpakjian and S.R. Schmid. *Manufacturing Processes for Engineering Materials*. Pearson Education, Inc., Upper Saddle River, 4th edition, 2003.

[26] G.R. Fenske. *Ion Implantation Processes*, volume 18 of *ASM Handbook*. ASM International, Materials Park, 2002.

[27] M. Nastasi and J.W. Mayer. *Ion Implantation and Synthesis of Materials*. Springer, Berlin, 2006.

[28] J.Y. Robic, J. Piaguet, and J.P. Gailliard. Some measurements of hardness, wear and stresses in ion-implanted thin metallic-films. *Nuclear Instruments & Methods*, 182(2):919–922, 1981.

[29] T.J. Kang, J.G. Kim, J.S. Lee, J.H. Lee, J.H. Hahn, H.Y. Lee, and Y.H. Kim. Low-thermal-budget and selective relaxation of stress gradients in gold micro-cantilever beams using ion implantation. *Journal of Micromechanics and Microengineering*, 15(12):2469–2478, 2005.

[30] S. Jin, H. Mavoori, J. Kim, and V.A. Aksyuk. Control of microelectromechanical systems membrane curvature by silicon ion implantation. *Applied Physics Letters*, 83(12):2321–2323, 2003.

[31] M. Ikeyama, K. Saitoh, S. Nakao, H. Niwa, S. Tanemura, Y. Niyagawa, and S. Miyagawa. Effects of MeV ion-implantation on metal-films. *Surface & Coatings Technology*, 66(1-3):305–309, 1994.

[32] N. Artunc, N. Elgun, A. Vizir, I. Brown, S. Bo, and E. Tarhan. Electrical and structural properties of Cr ion-implanted thin Au films. *Materials Chemistry and Physics*, 60(2):182–187, 1999.

[33] A. Anttila, J. Keinonen, M. Uhrmacher, and S. Vahvaselka. Nitrogen implantation of metals. *Journal of Applied Physics*, 57(4):1423–1425, 1985.

[34] G.M. Lancaster and J.W. Rabalais. Chemical-reactions of ${N_2}^+$ ion-beams with 1st-row transition-metals. *Journal of Physical Chemistry*, 83(2):209–212, 1979.

[35] X. Zhou, H.D. Li, and B.X. Liu. Formation of noble-metal nitrides by nitrogen implantation. *Nuclear Instruments and Methods in Physics Research Section B-Beam Interactions with Materials and Atoms*, 39(1-4):583–586, 1989.

[36] V.P. Bhattacharyya and P.D. Prabhawalkar. Effect of nitrogen ion-bombardment on copper gold interface. *Vacuum*, 42(8-9):543–546, 1991.

[37] H.K. Sanghera and J.L. Sullivan. Study of low energy high dose nitrogen implantation in aluminium, iron, copper and gold. *Surface and Interface Analysis*, 27(7):678–690, 1999.

[38] L. Siller, M.R.C. Hunt, J.W. Brown, J.M. Coquel, and P. Rudolf. Nitrogen ion irradiation of Au(110): Formation of gold nitride. *Surface Science*, 513(1):78–82, 2002.

[39] S. Krishnamurthy, M. Montalti, M.G. Wardle, M.J. Shaw, P.R. Briddon, K. Svensson, M.R.C. Hunt, and L. Siller. Nitrogen ion irradiation of Au(110): Photoemission spectroscopy and possible crystal structures of gold nitride. *Physical Review B*, 70(4):045414–1–5, 2004.

[40] L. Siller, N. Peltekis, S. Krishnamurthy, Y. Chao, S.J. Bull, and M.R.C. Hunt. Gold film with gold nitride - A conductor but harder than gold. *Applied Physics Letters*, 86(22):221912–1–3, 2005.

[41] Sun Ming, Rong Mingzhe, Wang Qiping, and Chen Degui. Modification of Ag-plated contacts by nitrogen ion implantation. In *IEEE Holm Conference on Electrical Contacts*, pages 467–471, 1996.

[42] P.I. Ignatenko, N.A. Klyakhina, and M.Y. Badekin. Structure and properties of metal nitride films produced by ion implantation. *Inorganic Materials*, 41(1):36–41, 2005.

[43] C. Karwat. The effect of nitrogen ion irradiation on the operational temperature regime of working surfaces of electrical contacts. *Vacuum*, 63(4):665–669, 2001.

[44] P.W. Leech. The effect of nitrogen implantation on the tribological properties of gold-based alloys and electroplated palladium. *IEEE Transactions on Components, Hybrids, and Manufacturing Technology [see also IEEE Trans. on Components, Packaging, and Manufacturing Technology, Part A, B, C]*, 11(1):16–21, 1988.

[45] P.W. Leech. The tribological properties of N_2^+ implanted AuAgCu alloy and palladium in sliding contact with gold electroplate. *IEEE Transactions onComponents, Hybrids, and Manufacturing Technology [see also IEEE Trans. on Components, Packaging, and Manufacturing Technology, Part A, B, C]*, 13(2):353–357, 1990.

[46] B. Navinsek and G. Carter. Ion-bombardment-induced resistivity changes in thin films of silver, gold, titanium and tungsten. *Canadian Journal of Physics*, 46(6):719–723, 1968.

[47] A. Komissarov, H. Kheyrandish, and Z.Y. Altamimi. Gold-films on silicon - Ion-bombardment-induced reactions between gold and silicon. *Thin Solid Films*, 137(2):267–279, 1986.

[48] V. Vishnyakov, S.E. Donnelly, and G. Carter. Scanning-tunneling-microscopy observations of the evolution of small-scale topography on gold surfaces following irradiation with low-energy argon ions. *Philosophical Magazine B-Physics of Condensed Matter Statistical Mechanics Electronic Optical and Magnetic Properties*, 70(1):151–157, 1994.

[49] M.V. Ramana Murty, T. Curcic, A. Judy, B.H. Cooper, A.R. Woll, J.D. Brock, S. Kycia, and R.L. Headrick. X-ray scattering study of the surface morphology of Au(111) during Ar^+ ion irradiation. *Physical Review Letters*, 80(21):4713–4716, 1998.

[50] S. Olliges, P. Gruber, A. Bardill, D. Ehrler, H.D. Carstanjen, and R. Spolenak. Converting polycrystals into single crystals - Selective grain growth by high-energy ion bombardment. *Acta Materialia*, 54(20):5393–5399, 2006.

[51] L. Guczi, Z. Paszti, K. Frey, A. Beck, G. Peto, and C.S. Daroczy. Modeling gold/iron oxide interface system. *Topics in Catalysis*, 39(3-4):137–143, 2006.

[52] H. Yin, H.G. Boyen, X.W. Zhang, and P. Ziemann. Fabrication of ohmic Au/Cr contacts on top of cubic boron nitride films. *Diamond and Related Materials*, 16(1):46–49, 2007.

[53] R.C. Birtcher and S.E. Donnelly. Plastic flow induced by single ion impacts on gold. *Physical Review Letters*, 77(21):4374–4377, 1996.

[54] R.C. Birtcher and S.E. Donnelly. Plastic flow produced by single ion impacts on metals. *Nuclear Instruments and Methods in Physics Research Section B-Beam Interactions with Materials and Atoms*, 148(1-4):194–199, 1999.

[55] T.M. Nenadovic, Z.B. Fotiric, and T.S. Dimitrijevic. Sputtering of gold bombarded by 20-50 keV Ar^+ and Xe^+ ions. *Surface Science*, 33(3):607–616, 1972.

[56] N. Matsunami, M. Sataka, A. Iwase, T. Inami, and M. Kobiyama. Sputtering of nanocrystalline gold by high energy heavy ions. *Journal of Nuclear Materials*, 302(2-3):206–210, 2002.

[57] J. Samela, J. Kotakoski, K. Nordlund, and J. Keinonen. A quantitative and comparative study of sputtering yields in Au. *Nuclear Instruments & Methods in Physics Research Section B-Beam Interactions with Materials and Atoms*, 239(4):331–346, 2005.

[58] M. Antler. Gold-plated contacts: Effect of thermal aging on contact resistance. *Plating and Surface Finishing*, 85(12):85–90, 1998.

[59] T. Osaka, Y. Okinaka, J. Sasano, and M. Kato. Development of new electrolytic and electroless gold plating processes for electronics applications. *Science and Technology of Advanced Materials*, 7(5):425–437, 2006.

[60] N. Togasaki, Y. Okinaka, T. Homma, and T. Osaka. Preparation and characterization of electroplated amorphous gold-nickel alloy film for electrical contact applications. *Electrochimica Acta*, 51(5):882–887, 2005.

[61] A.F. Jankowski, C.K. Saw, J.F. Harper, B.F. Vallier, J.L. Ferreira, and J.P. Hayes. Nanocrystalline growth and grain-size effects in Au-Cu electrodeposits. *Thin Solid Films*, 494(1-2):268–273, 2006.

[62] V. Radmilovic, D. Mitlin, and U. Dahmen. Ultra-hard nanostructured Al-Si thin films. In *Current Research in Advanced Materials and Processes*, volume 494 of *Materials Science Forum*, pages 13–18. 2005.

[63] E. Hornbogen, A.K. Mukhopadhyay, and E.A. Starke. Precipitation hardening of Al-(Si,Ge) alloys. *Scripta Metallurgica et Materialia*, 27(6):733–738, 1992.

[64] D. Mitlin, U. Dahmen, V. Radmilovic, and J.W. Morris. Precipitation and hardening in Al-Si-Ge. *Materials Science and Engineering A-Structural Materials Properties Microstructure and Processing*, 301(2):231–236, 2001.

[65] V. Radmilovic, M.K. Miller, D. Mitlin, and U. Dahmen. Strain-compensated nano-clusters in Al-Si-Ge alloys. *Scripta Materialia*, 54(11):1973–1978, 2006.

[66] D. Mitlin, V. Radmilovic, U. Dahmen, and J.W. Morris. Precipitation and aging in Al-Si-Ge-Cu. *Metallurgical and Materials Transactions A-Physical Metallurgy and Materials Science*, 32(1):197–199, 2001.

[67] A.G. Ramirez and R. Saha. Combinatorial studies for determining properties of thin-film gold-cobalt alloys. *Applied Physics Letters*, 85(22):5215–5217, 2004.

[68] N. Nelson-Fitzpatrick, C. Ophus, E. Luber, L. Gervais, Z. Lee, V. Radmilovic, D. Mitlin, and S. Evoy. Synthesis and characterization of Au-Ta nanocomposites for nanomechanical cantilever devices. *Nanotechnology*, 18(35):1–7, 2007.

[69] A.A. Johnson and D.N. Johnson. The room-temperature dissociation of Au_3Si in hypoeutectic Au-Si alloys. *Materials Science and Engineering*, 61(3):231–235, 1983.

[70] B. Bhushan and X.D. Li. Micromechanical and tribological characterization of doped single-crystal silicon and polysilicon films for microelectromechanical systems devices. *Journal of Materials Research*, 12(1):54–63, 1997.

[71] J.W. Martin. *Precipitation Hardening*. Butterworth Heinemann, Boston, 2nd edition, 1998.

[72] G.E. Dieter. *Mechanical Metallurgy*. McGraw Hill, Boston, 3rd edition, 1986.

[73] E. Orowan. Symposium on internal stress in metals and alloys. In *The Institute of Metals*, page 451, London, 1948.

[74] M.F. Ashby. The Theory of the Critical Shear Stress and Work Hardening of Dispersion-Hardened Crystals. In *Proceedings of the Second Bolton Landing Conference on Oxide Dispersion Strengthening*, pages 143–212, London, 1966.

[75] I. Shao, P.M. Vereecken, C.L. Chien, P.C. Searson, and R.C. Cammarata. Synthesis and characterization of particle-reinforced Ni/Al_2O_3 nanocomposites. *Journal of Materials Research*, 17(6):1412–1418, 2002.

[76] W.J. Callister. *Materials Science and Engineering - An Introduction*. John Wiley & Sons, Inc., New York, 6th edition, 2003.

[77] W.C. Oliver and G.M. Pharr. An improved technique for determining hardness and elastic-modulus using load and displacement sensing indentation experiments. *Journal of Materials Research*, 7(6):1564–1583, 1992.

[78] A.C. Fischer-Cripps. *Nanoindentation*. Mechanical Engineering Series. Springer-Verlag, New York, 2002.

[79] D. Tabor. A simple theory of static and dynamic hardness. *Proceedings of the Royal Society of London Series A*, 192(1029):247–274, 1948.

[80] S.I. Bulychev, V.P. Alekhin, M.K. Shorshorov, A.P. Ternovskii, and G.D. Shnyrev. Determination of Young's modulus according to indentation diagram. *Zavodskaya Laboratoriya*, 41(9):1137–1140, 1975.

[81] Y. Strausser, editor. *Characterization in Silicon Processing*. Elsevier, 1993.

[82] K. Seshan, editor. *Handbook of Thin-Film Deposition Process and Techniques - Principles, Methods, Equipment and Applications*. William Andrew Publishing/Noyes, 2nd edition, 2002.

[83] G.M. Pharr. Measurement of mechanical properties by ultra-low load indentation. *Materials Science and Engineering A-Structural Materials Properties Microstructure and Processing*, 253(1-2):151–159, 1998.

[84] M.J. Klopfstein. *Investigation of the Near Surface Mechanical Behavior of Single Crystal* ZnO *by Nanoindentation*. Ph.d. dissertation, Oklahoma State University, 2004.

[85] ISO. ISO 14577-4: Test method for metallic and non-metallic coatings. Technical report, International Organization for Standardization, 2004.

[86] M.J. Klopfstein. Indentation Data Analyzer (IDA), 2006.

[87] Veeco Inc. FPP-5000 Four Point Resistivity Probe: Installation, Operation and Maintenance Manual.

[88] H. Topsoe. *Geometric Factors in Four Point Resistivity Measurement*. 2nd edition, 1968. [Online:http://www.four-point-probes.com/haldor.html; accessed 29-May-2008].

[89] C. Suranarayana and M.G. Norton. *X-Ray Diffraction - A Practical Approach*. Plenum Press, New York, 1998.

[90] Bruker AXS Inc. Diffraction Solutions - D8 Advance, 2008. [Online:http://www.brukersupport.com/Uploaded/Documents/Repository/B88-E00014%20D8%20ADVANCE%20Brochure.pdf; accessed 28-May-2008].

[91] V.K. Pecharsky and P.Y. Zavalij. *Fundamentals of Powder Diffraction and Structural Characterization of Materials*. Kluwer Academic Publishers, Boston, 2003.

[92] B.P. Grady. Characterizing arrangement of atoms in a nanostructure: Wide-angle x-ray diffraction, 2006. [Online:http://frontpage.okstate.edu/nanotech; accessed 28-May-2008].

[93] International Centre for Diffraction Data, 2008. [Online:http://www.icdd.com; accessed 28-May-2008].

[94] D.C. Miller, C.F. Herrmann, H.J. Maier, S.M. George, C.R. Stoldt, and K. Gall. Intrinsic stress development and microstructure evolution of Au/Cr/Si multilayer thin films subject to annealing. *Scripta Materialia*, 52(9):873–879, 2005.

[95] D.C. Miller, C.F. Herrmann, H.J. Maier, S.M. George, C.R. Stoldt, and K. Gall. Thermo-mechanical evolution of multilayer thin films: Part II. Microstructure evolution in Au/Cr/Si micro cantilevers. *Thin Solid Films*, 515(6):3224–3240, 2007.

[96] P.H. Holloway. Gold/chromium metallization for electronic devices. *Solid State Technology*, 23(2):109–115, 1980.

[97] L.B. Freund and S. Suresh. *Thin Film Materials - Stress, Defect Formation and Surface Evolution*. Cambridge University Press, Cambridge, 2003.

[98] Z.H. Xu and D. Rowcliffe. Deriving mechanical properties of soft coatings using nanoindentation: An application of mechanism-based strain gradient plasticity. *Surface & Coatings Technology*, 157(2-3):231–237, 2002.

[99] C. San Marchi, N.R. Moody, M.J. Cordill, G. Lucadamo, J.J. Kelly, T. Headley, and N. Yang. Structure-property relationships of Au films electrodeposited on Ni. In P.M. Anderson, T. Foecke, A. Misra, and R.E. Rudd, editors, *Nanoscale Materials and Modeling-Relations Among Processing, Microstructure and Mechanical Properties*, volume 821 of *Material Res. Soc. Symp. Proc.*, Warrendale, PA, 2004.

[100] J.F. Smith and S. Zheng. High temperature nanoscale mechanical property measurements. *Surface Engineering*, 16(2):143–146, 2000.

[101] A.A. Volinsky, N.R. Moody, and W.W. Gerberich. Nanoindentation of Au and Pt/Cu thin films at elevated temperatures. *Journal of Materials Research*, 19(9):2650–2657, 2004.

[102] N.R. Moody, D.P. Adams, D. Medlin, T. Headley, N. Yang, and A. Volinsky. Effects of diffusion on interfacial fracture of gold-chromium hybrid microcircuit films. *International Journal of Fracture*, 119(4-2):407–419, 2003.

[103] G. Simmons and H. Wang. *Single Crystal Elastic Constants and Calculated Aggregate Properties: A Handbook*. The M.I.T. Press, Cambridge, 2nd edition, 1971.

[104] D.M. Mattox. Thin-film metallization of oxides in microelectronics. *Thin Solid Films*, 18(2):173–186, 1973.

[105] P. Madakson. Correlation between resistivity and diffusion in thin-films. *Journal of Applied Physics*, 70(3):1380–1384, 1991.

[106] N.A. Fleck, G.M. Muller, M.F. Ashby, and J.W. Hutchinson. Strain gradient plasticity - Theory and experiment. *Acta Metallurgica et Materialia*, 42(2):475–487, 1994.

[107] Q. Ma and D.R. Clarke. Size-dependent hardness of silver single-crystals. *Journal of Materials Research*, 10(4):853–863, 1995.

[108] W.D. Nix. Elastic and plastic properties of thin films on substrates: Nanoindentation techniques. *Materials Science and Engineering A-Structural Materials Properties Microstructure and Processing*, 234:37–44, 1997.

[109] W.D. Nix and H.J. Gao. Indentation size effects in crystalline materials: A law for strain gradient plasticity. *Journal of the Mechanics and Physics of Solids*, 46(3):411–425, 1998.

[110] D.A. Lucca, M.J. Klopfstein, O.R. Mejia, L. Rossettini, and L.T. DeLuca. Investigation of ammonium perchlorate by nanoindentation. *Materials Science and Technology*, 22(4):396–401, 2006.

[111] R.F. Hummel. *Electronic Properties of Materials*. Springer-Verlag, Berlin, 2nd edition, 1993.

[112] A. Arranz and C. Palacio. The room temperature growth of Ti on sputter-cleaned Si(100): Composition and nanostructure of the interface. *Surface Science*, 588(1-3):92–100, 2005.

[113] S.P. Murarka and D.B. Fraser. Thin-film interaction between titanium and polysilicon. *Journal of the Electrochemical Society*, 126(11):C456–C456, 1979.

[114] B.D. Agarwal, L.J. Broutman, and K. Chandrashekhara. *Analysis and Performance of Fiber Composites*. John Wiley & Sons, Inc., Hoboken, 3rd edition, 2006.

[115] H.S. Kim. On the rule of mixtures for the hardness of particle reinforced composites. *Materials Science and Engineering A-Structural Materials Properties Microstructure and Processing*, 289(1-2):30–33, 2000.

[116] R. Hill. The elastic behaviour of a crystalline aggregate. *Proceedings of the Physical Society of London Section A*, 65(389):349–355, 1952.

[117] G.H. Staab. *Laminar Composites*. Butterworth-Heinemann, Oxford, 1999.

[118] International Centre for Diffraction Data. JCPDS card number 00-004-0784.

[119] W. Tang, K.W. Xu, P. Wang, and M. Li. Residual stress and crystal orientation in magnetron sputtering Au films. *Materials Letters*, 57(20):3101–3106, 2003.

[120] W. Tang, L.J. Deng, K.W. Xu, and J. Lu. X-ray diffraction measurement of residual stress and crystal orientation in Au/Ni/Cr/Ta films prepared by plating. *Surface & Coatings Technology*, 201(12):5944–5947, 2007.

[121] R.A. Roy, J.J. Cuomo, and D.S. Yee. Control of microstructure and properties of copper-films using ion-assisted deposition. *Journal of Vacuum Science & Technology A-Vacuum Surfaces and Films*, 6(3):1621–1626, 1988.

[122] S.P. Kim, H.M. Choi, and S.K. Choi. A study on the crystallographic orientation with residual stress and electrical property of Al films deposited by sputtering. *Thin Solid Films*, 322(1-2):298–302, 1998.

[123] J.M. Zhang, K.W. Xu, and V. Ji. Dependence of stresses on grain orientations in thin polycrystalline films on substrates: An explanation of the relationship between preferred orientations and stresses. *Applied Surface Science*, 180(1-2):1–5, 2001.

[124] D.K. George, A.A. Johnson, and R.J. Storey. Preparation of the metastable compound Au_3Si by quenching liquid droplets of a Au-25 at.% Si alloy into water. *Materials Science and Engineering B-Solid State Materials for Advanced Technology*, 55(3):221–224, 1998.

[125] P. Duwez and R.H. Willens. Rapid quenching of liquid alloys. *Transactions of the Metallurgical Society of AIME*, 227(2):362–365, 1963.

[126] P. Predecki, B.C. Giessen, and N.J. Grant. New metastable alloy phases of gold, silver and aluminum. *Transactions of the Metallurgical Society of AIME*, 233(7):1438–1439, 1965.

[127] G.A. Andersen, J.L. Bestel, A.A. Johnson, and B. Post. Eutectic decomposition in gold-silicon system. *Materials Science and Engineering*, 7(2):83–90, 1971.

[128] R.C. Krutenat, J.K. Tien, and D.E. Fornwalt. Sputter deposition of a metastable phase in Au-Si system. *Metallurgical Transactions*, 2(5):1479–1481, 1971.

[129] C. Suryanarayana and T.R. Anantharaman. Crystal-structure of a nonequilibrium phase in gold-silicon system. *Materials Science and Engineering*, 13(2):73–81, 1974.

[130] R.P. Anantatmula, A.A. Johnson, S.P. Gupta, and R.J. Horylev. Gold-silicon phase-diagram. *Journal of Electronic Materials*, 4(3):445–463, 1975.

[131] A.K. Green and E. Bauer. Formation, structure, and orientation of gold silicide on gold surfaces. *Journal of Applied Physics*, 47(4):1284–1291, 1976.

[132] P. Mangin, G. Marchal, C. Mourey, and C. Janot. Physical studies of Au_xSi_{1-x} amorphous-alloys. *Physical Review B*, 21(8):3047–3056, 1980.

[133] H.L. Gaigher and N.G. Van der Berg. The structure of gold silicide in thin Au-Si films. *Thin Solid Films*, 68(2):373–379, 1980.

[134] N.G. Dhere and C.D.A. Loural. Metastable structures in Au-Si thin-films. *Thin Solid Films*, 81(3):213–223, 1981.

[135] L. Hultman, A. Robertsson, H.T.G. Hentzell, I. Engstrom, and P.A. Psaras. Crystallization of amorphous-silicon during thin-film gold reaction. *Journal of Applied Physics*, 62(9):3647–3655, 1987.

[136] W. Robison, R. Sharma, and L. Eyring. Observation of gold silicon alloy formation in thin-films by high-resolution electron-microscopy. *Acta Metallurgica et Materialia*, 39(2):179–186, 1991.

[137] M.S. Ashtikar and G.L. Sharma. Structural investigation of gold induced crystallization in hydrogenated amorphous-silicon thin-films. *Japanese Journal of Applied Physics Part 1-Regular Papers Short Notes & Review Papers*, 34(10):5520–5526, 1995.

[138] R.R. Chromik, L. Zavalij, M.D. Johnson, and E.J. Cotts. Calorimetric investigation of the formation of metastable silicides in Au/a-Si thin film multilayers. *Journal of Applied Physics*, 91(11):8992–8998, 2002.

[139] W. Klement, R.H. Willens, and P. Duwez. Non-crystalline structures in solidified gold-silicon alloys. *Nature*, 187(4740):869–870, 1960.

[140] M. Telford. The case for bulk metallic glass. *Materials Today*, 7(3):36–43, 2004.

[141] H.H. Liebermann. Sample preparation: Methods and process characterization. In F.E. Luborsky, editor, *Amorphous Metallic Alloys*. Buttersworth & Co. Ltd., Boston, 1983.

[142] International Centre for Diffraction Data. JCPDS card number 00-026-0725.

[143] International Centre for Diffraction Data. JCPDS card number 00-024-0463.

[144] International Centre for Diffraction Data. JCPDS card number 00-026-0723.

[145] International Centre for Diffraction Data. JCPDS card number 00-026-0724.

[146] International Centre for Diffraction Data. JCPDS card number 00-026-0726.

[147] International Centre for Diffraction Data. JCPDS card number 00-036-0938.

[148] International Centre for Diffraction Data. JCPDS card number 00-039-0735.

[149] International Centre for Diffraction Data. JCPDS card number 00-040-1140.

[150] D. Bhattacharya, A.A. Johnson, R.K. Sorem, and G.A. Andersen. Room-temperature dissociation of compound Au_3Si. *Materials Science and Engineering*, 32(2):181–184, 1978.

[151] Digital Instruments. Dimension 3100 Instruction Manual, 1997.

[152] Digital Instruments Veeco Metrology Group. Scanning Probe Microscopy Training Notebook, 1997.

[153] Digital Instruments Veeco Metrology Group. NanoScope Command Reference Manual, 2001.

[154] Hysitron Inc. Triboindenter® User Manual, 2005.

[155] Hysitron Inc. Triboscope® Nanomechanical Test System: Setup & Operation Guide, 1996.

Appendix A

Procedure for measuring the surface topography using the Atomic Force Microscope

This chapter describes the procedure performed during a set of surface topography measurements using the AFM instrument (diDimension® 3100 manufactured by Veeco, Inc.), including the set-up of the instrument and software, performing the surface scan and analyzing the results. The operating procedures have been adapted from the Dimension 3100 Series Scanning Probe Microscope Instruction Manual [151], Scanning Probe Microscopy Training Notebook [152] and the Veeco Command Reference Manual [153].

A.1 Instrument and software set-up

The NanoScope Dimension 3100 controller, Nanoscope IIIa Scanning Probe Microscope Controller and the computer system to the right of the instrument are turned on. Next, the toggle switch, located at the rear of the instrument, is adjusted so that **STD** is activated.

The NanoScope software is started by selecting the desktop shortcut labeled *NanoScope Version 5.30r3.S13*. The proper AFM mode of operation is selected by choosing **Microscope** → **Profile** → selecting either *Tapping* or *Contact* → **Load** in the Real-time operating window of the software. Tapping mode was used for all experimental measurements. The software is then interfaced with the AFM head by selecting **Microscope** → **Scanner** → **1024g**.

A.1.1 SPM parameters

The SPM parameters, which are the most important Z-axis parameter values for correct operation of the AFM, are specified next. These are selected by choosing **Stage** → **SPM Parameters** and the appropriate values from Table A.1 are specified in the SPM Parameters panel. For further detail on SPM Parameters, see *Section 9.13* of the Veeco Command Reference Manual [153].

SPM Parameters	
Sample Clearance:	1000 μm
SPM Safety:	100 μm
SPM Engage Step:	0.417 μm
Load/Unload Height:	2000 μm
SPM Exclusion Limit:	0.00
SPM Exclusion Limit 2:	0.00

Table A.1: SPM parameters panel

A.1.2 Initial scan parameters

The initial scan parameters are then set in the Real-time operating window of the software according to the values in Tables A.2 through A.6. For the **Channel 1** panel, height is specified as the data type, however additional Channels 2 and 3 can be activated to display a different data type such as amplitude, current, deflection, frequency, friction, phase, potential or thermal (temperature) [153]. For further detail on the initial scan parameters, see *Chapter 3* of the Veeco Command Reference Manual [153].

A.1.3 Installing the cantilever, cantilever holder and AFM head

After all of the software settings have been correctly specified, the cantilever is installed onto the cantilever holder. The cantilevers used for the surface topography measurements are the model RTESP5, also known as TappingMode Etched Silicon Probes (TESP) [152]. The tip number and date are recorded in the "SPM Tips" laboratory notebook. The tip is placed into the cantilever mounting groove, using sharp tweezers, flush against the rear edge and centered between the left and right edges of the groove located on the cantilever holder, shown in Figure A.1, and the spring loaded probe clip is used to hold the cantilever in place. The cantilever holder is located on the

Scan Controls	
Scan size:	1 μm
X offset:	0.0 μm
Y offset:	0.0 μm
Scan angle:	0.00°
Scan rate:	0.40 Hz
Tip velocity:	0.800 μ/s
Samples/line:	256
Lines:	256
Slow scan axis:	Enabled

Table A.2: Scan Controls panel

Feedback Controls	
Z modulation:	Disabled
Integral gain:	0.200
Proportional gain:	0.300
LookAhead gain:	0
Amplitude setpoint:	1.00 V
Drive frequency:	*Determined by Autotune*
Drive amplitude:	*Determined by Autotune*

Table A.3: Feedback Controls panel

Other Controls	
Microscope Mode:	Tapping
Z limit:	2.064 μm
FM igain:	15.00
FM pgain:	15.00
Illumination:	0
Units:	Metric
Color:	13
Engage:	0.970
Tip serial:	——
Serial number:	SN5-129-08 (*Automatically Entered*)
Min. engage gain:	3.00
Parm update retract:	Disabled

Table A.4: Other Controls panel

Channel 1	
Data type:	Height
Data Scale:	100 nm
Line direction:	Trace/Retrace
Scan line:	Main (*Automatically Entered*)
Realtime planefit:	Line
Offline planefit:	None

Table A.5: Channel 1 panel

Drive Feedback Controls	
Drive feedback:	Disabled
Drive height:	2.209 nm
Drive time:	10.0 ms
Drive setpoint:	0.900
Drive gain:	1.00

Table A.6: Drive Feedback Controls panel

standard AFM station of the cantilever holder stand, shown in Figure A.2, which allows for easy operation of the cantilever holder [151].

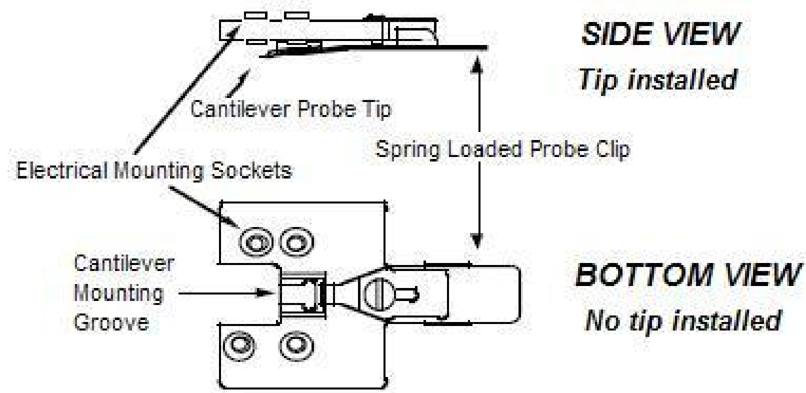

Figure A.1: Schematic of the AFM cantilever holder. After Reference [151].

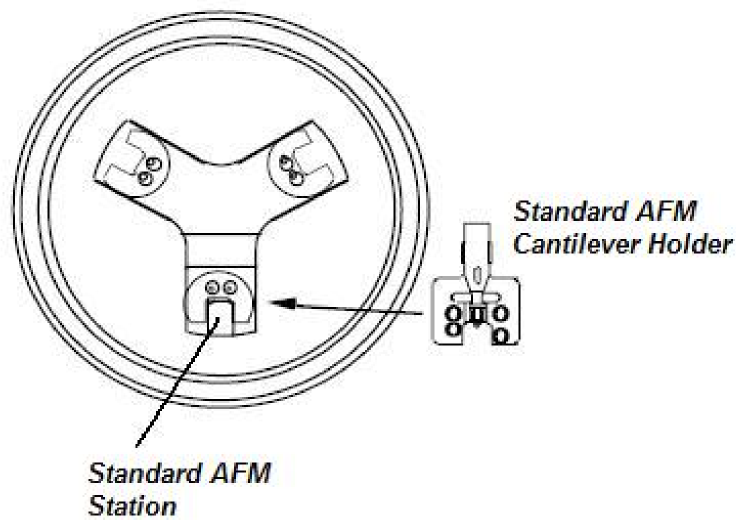

Figure A.2: Schematic of the AFM cantilever holder stand. After Reference [151].

Next, the cantilever holder, with the tip facing toward the instrument's optics, is installed onto the AFM head by mating the electrical mounting sockets flush with the electrical pins on the bottom of the AFM head. The AFM head is then installed in the dovetail groove of the main instrument and properly mounted by turning the screw, located to the right of the groove, counter-clockwise. The two plugs from the scanner are then connected to the appropriate sockets located on the electronics box of the main instrument after which the AFM's laser will activate.

A.1.4 Aligning the laser

It is then necessary to align the laser on the cantilever tip to ensure proper collection by the photodetector. The laser spot is positioned on the edge of the tip using the X and Y laser control knobs located on the AFM scanner, shown in Figure A.3. When the laser spot is properly positioned on the edge of the tip, the Laser Sum Signal should be approximately 2 V [152]. The photodetector mirror knobs located on the left side of the AFM scanner, shown in Figure A.4, are then adjusted. When the laser spot is properly positioned, the red spot will be brightly visible at the origin of the Detector quadrant schematic located in the Vision System window [151].

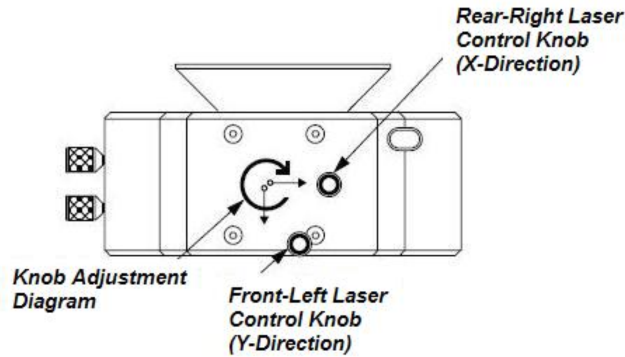

Figure A.3: Top-view of the AFM scanner head showing the location of the laser control knobs. After Reference [151].

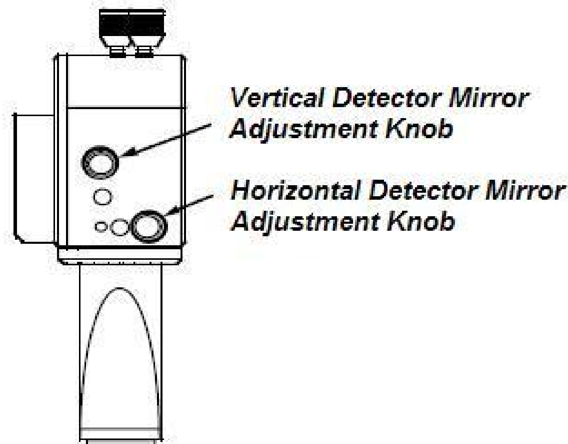

Figure A.4: Side-view of the AFM scanner head showing the location of the detector mirror adjustment knobs. After Reference [151].

A.1.5 Specimen placement

When the laser alignment is complete, the specimen is placed on the instrument's vacuum chuck. Before doing so, ensure that the AFM scanner is raised high enough, using the trackball, to allow for proper clearance, and the vacuum chuck is clean and free of debris. The chuck can be cleaned with a lint-free cloth and alcohol if necessary. The specimen is placed directly onto the vacuum chuck and held in place by engaging the "Vacuum" toggle switch on the main Electronics Box [151]. The stage and chuck are adjusted in the X and Y directions using the **Focus Surface** command button and the trackball to properly place the specimen under the AFM tip.

A.1.6 Locating the tip in the Vision System

Before using the optical system to locate the tip, the tip is moved closer to the specimen surface using the **Focus Surface** command icon and the trackball, with the bottom left button pressed, while simultaneously visually confirming tip clearance with the specimen surface. Next, the tip is located by using the **Focus Tip** command icon and the adjustment knobs located next to the optics to the left of the scanner. During this step it is necessary to adjust the illumination within the **Focus Tip** control box. When the tip is located in the Vision System window, the cantilever tip is focused using the trackball, with the bottom left button pressed, and the optical adjustment knobs are used to align the cross-hairs at the center of the edge of the cantilever tip. *OK* on the **Focus Tip** control box is selected when finished.

A.1.7 Focusing on the specimen surface

The AFM's Z-stage is then used to focus on the surface of the specimen which will serve to bring the tip within the correct initial starting vertical position. The **Focus Surface** command icon is selected and using the trackball, with the bottom left button pressed, the tip is slowly moved down in the Z-direction to focus the surface of the specimen on the Vision System. While performing this step it is again necessary to simultaneously visually confirm tip clearance with the specimen surface to avoid damaging the AFM tip. *OK* on the **Focus Tip** control box is selected when finished.

A.1.8 Auto tuning the cantilever

Finally, the cantilever is tuned to determine its resonance peak and adjust the oscillation voltage to ensure that the cantilever vibrates properly [151]. The **Cantilever Tune** command icon is selected within the software and then **Auto Tune** is selected to prompt the software to automatically

perform this procedure, during which, "Tuning..." will appear on the screen and disappear when the procedure is complete [152]. The resonance peak should have a sharp Gaussian profile [151]. When the Auto Tune is complete, the cantilever Drive Frequency and Amplitude are recorded within the "SPM Tips" laboratory notebook and *Quit* is selected to close the **Cantilever Tune** control box and complete the tuning procedure.

A.2 Performing a surface scan

Once the initial setup of the instrument and software is complete, a surface scan is performed. The **Engage** command icon is selected within the software at which time the instrument lowers the AFM tip to the specimen surface and automatically begins scanning once the surface is detected. When the scanning begins, the **Scope Mode** command icon is selected and proper tip tracking is confirmed by ensuring that the *Trace* and *Retrace* scans are similar and have a minimum vertical separation. The tip tracking can be improved by increasing both the *Integral* and *Proportional Gains* equal amounts by pressing the right arrow key 1 - 3 times in each box. Additionally, the *Setpoint* can be increased, again by pressing the right arrow, which will decrease the force from the cantilever tip applied to the specimen surface [152].

The image of the surface topography is then obtained by first assigning a filename by choosing **Capture** → **Capture Filename**. An additional file note can be added within **Capture Filename** control box. *OK* is selected when finished. The image is captured by selecting the **Capture** icon. The Status Bar located at the bottom of the Real-time operating window of the software will display **On** when the capture is in progress, **Next** if the system is waiting for the next complete frame to begin and **Done** when the capture is complete.

After the image is captured, it will automatically stored in the temporary !:\ directory and the system will continue to scan the surface until prompted to stop. At this time, if no additional images are desired, the tip is secured by choosing the **Withdraw** command icon to end scanning and secure the instrument.

A.3 Analyzing the AFM image

Once the scan is complete and the instrument is secured, the image analysis is begun by switching from the Real-time operating window to the Off-line operating window by choosing the **Off-line** icon. The captured image is selected and first processed using an automatic Planefit filter which

applies a either a 1st, 2nd or 3rd order polynomial fit to the image in both the X and Y directions to remove tilt, tilt and an arch-shaped bow, or tilt and an S-shaped bow, respectively [152]. For all images used in this study, a 1st order planefit was applied by selecting **Modify** → **Plane Fit Auto** → **XY** → **Execute** → **Quit** within the Off-line operating window. Next, the image is processed using a Flatten filter which applies either a 0th, 1st, 2nd or 3rd order polynomial fit to each scan line to remove image artifacts due to scanner drift, image bow, skips or additional effects which could have caused vertical offset between between scan lines, respectively [152]. For all images used in this study, a 0th order planefit was applied by selecting **Modify** → **Flatten** → **Execute** → **Quit** within the Off-line operating window.

After the images are filtered, the surface roughness is measured by selecting **Analyze** → **Roughness** within the Off-line window at which time the **Roughness Analysis** window appears. Ra and Rq are automatically calculated and displayed under *Image Statistics* within the **Roughness Analysis** window. Rz is measured by using the mouse to select the entire image and select **Execute**, after which the value is calculated and displayed under *Box Statistics* within the **Roughness Analysis** window.

Once the roughness is measured the analysis is complete and the image is saved and exported by selecting **Utility** → **JPEG Export**. Within the **JPEG Export** command window, *Screen* is selected under **Source**, *Reverse* for the **Background** and the Destination Directory and file to be exported are specified.

Appendix B

Procedure for measuring the mechanical properties by Nanoindentation

This chapter describes the procedure performed during a set of nanoindentation experiments using the load-controlled nanoindenter (TriboScope Nanomechanical Test System® manufactured by Hysitron, Inc.) interfaced with the AFM system described in Appendix A. The procedure necessary to install and interface the nanoindenter with the AFM system will be discussed first after which the procedure for set-up of the Hysitron software and instrumentation will be discussed. The operating procedures have been adapted from the TriboIndenter® User Manual [154], Dimension 3100 Series Scanning Probe Microscope Instruction Manual [151], Scanning Probe Microscopy Training Notebook [152] and the Veeco Command Reference Manual [153].

Topics discussed will include a background on the operation of the Hysitron nanoindenter, the set-up of both instruments and software 10-12 hours prior to experimentation, performing the preliminary surface scan, the indentation and analysis of the results.

B.1 Background

The nanoindentation experiments were performed on the same instrument as the AFM by replacing the AFM head with the Hysitron nanoindentation system. Besides the necessary computer, controller and signal adapter, the main portions of the instrument are the TriboScanner piezoelectric scanner,

three plate capacitive transducer and indenter. The TriboScanner allows for precise placement of the indenter on the specimen surface as well as in-situ imaging of the surface before and after indentations are performed. It operates through a series of piezoelectric ceramic plates that change shape due to an applied voltage (operating voltage: -185V to +185V) allowing for precise motion in the X, Y and Z directions with maximum X, Y and Z ranges of 60 μm, 60 μm and 3 μm, respectively [154].

The three plate capacitive transducer is utilized to perform the simultaneous application of the force and measurement of the indenter's displacement into the material. The transducer, shown in Figure B.1, consists of the two outer electrodes, the top and bottom drive plates and the center pickup electrode, to which the indenter is mounted (such that the force and displacement of the center plate correspond to the force and displacement of the tip). The transducer measures the vertical displacement of the pickup electrode, and therefore the indenter tip, by applying an AC signal, 180° out of phase, to the two outer drive plates. The electric potential between the two outer plates varies linearly and since the AC signal is 180° out of phase, the electric potential is equal to the applied signal at the drive plates and zero at the pickup electrode. The impedance is such that the output signal from the transducer is equal to the potential of the center pickup electrode. Therefore, the vertical displacement is measured from this signal and equal to zero at the center position and varies linearly as the pickup electrode moves toward each drive plate. The transducer is capable of a maximum vertical displacement of 5 μm with a resolution of less than 1 nm. The force is applied to the pickup electrode, and therefore the indenter tip, by applying a DC voltage to the bottom drive plate to create an electrostatic attraction to the center pickup electrode causing it to deflect toward the bottom plate. The applied vertical force is then measured from the applied voltage. The system is capable of applying a maximum vertical force of approximately 10 mN with a resolution of 1nN [155].

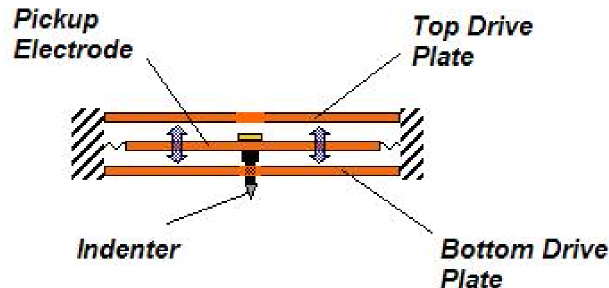

Figure B.1: Schematic cross-section of the 1-D three place capacitive transducer. After Reference [154].

B.2 Instrument and software set-up - Interfacing the TriboScope with the AFM system

The NanoScope Dimension 3100 controller, Nanoscope IIIa Scanning Probe Microscope Controller and the computer system are turned on. *It is then crucial at this point to adjust the toggle switch, located at the rear of the instrument, so that* ***Hysitron*** *is activated.* The TriboScanner will not operate correctly if this step is not completed and there is a risk for damaging both the transducer and indenter.

Next, the NanoScope software is started by selecting the desktop shortcut labeled *NanoScope Version 5.30r3.S13*. The proper nanoindentation mode of operation is then selected by choosing **Microscope** → **Profile** → **STM - hys** → **Load** in the Real-time operating window of the software. The software is then interfaced with the Hysitron TriboScope head by choosing **Microscope** → **Scanner** → **SN5-129-08**.

B.2.1 SPM parameters

The SPM parameters, which are also the most important Z-axis parameter values for correct operation of the nanoindenter, are specified next. These are selected by choosing **Stage** → **SPM Parameters** and the appropriate values from Table B.1 are specified in the SPM Parameters Panel. For further detail on SPM Parameters, see *Section 9.13* of the Veeco Command Reference Manual [153].

SPM Parameters	
Sample Clearance:	100 μm
SPM Safety:	100 μm
SPM Engage Step:	0.139 μm
Load/Unload Height:	2000 μm
SPM Exclusion Limit:	0.00
SPM Exclusion Limit 2:	0.00

Table B.1: SPM parameters for proper nanoindenter operation

B.2.2 Initial scan parameters

The initial scan parameters are then set in the Real-time operating window of the software according to the values in Tables B.2 through B.5. In the the **Scan Controls** panel, the Scan size is initially set to 0.00 nm and therefore the tip velocity will initially be 0.00 μ/s. The *Integral* and *Proportional Gains* are set to 2.00 and 3.00, respectively, in the **Feedback Controls** panel when performing nanoindentation experiments. Additionally, only one channel is activated when using the nanoindenter. For further detail on the initial scan parameters, see *Chapter 3* of the Veeco Command Reference Manual [153].

Scan Controls	
Scan size:	0.00 nm
X offset:	0.0 μm
Y offset:	0.0 μm
Scan angle:	0.00°
Scan rate:	1.00 Hz
Tip velocity:	0.00 μ/s
Samples/line:	256
Lines:	256
Slow scan axis:	Enabled

Table B.2: Scan Controls panel

Feedback Controls	
Current setpoint:	1.00 nA
Integral gain:	2.00 μm
Proportional gain:	3.00 μm

Table B.3: Feedback Controls panel

B.2.3 Cleaning and installing the indenter tip

Prior to installing the indenter to the transducer, it is necessary to clean the diamond tip. This is done by removing the tip from the transducer (or from the storage case if not installed) and wiping the surface of the tip with a lint-free lens tissue which has been saturated with a 70%/30% mixture

Other Controls	
Z limit:	2.064 μm
Illumination:	0
Units:	Metric
Color:	13
Tip serial:	——
Serial number:	SN5-129-08 (*Automatically Entered*)
Min. engage gain:	3.00
Parm update retract:	Disabled

Table B.4: Other Controls panel

Channel 1	
Data type:	Height
Data Scale:	100 nm
Line direction:	Trace/Retrace
Realtime planefit:	Line
Offline planefit:	None

Table B.5: Channel 1 panel

of methanol/ethyl alcohol. The saturated tissue, which is held using a pair of locking forceps, is first carefully wiped in a single direction across the tip using the top side of the tissue and then wiped in the opposite direction using the bottom side of the tissue. The tip is then washed directly with the methanol/ethyl alcohol mixture and immediately dried using ultra high purity N_2 gas.

The tip is then placed into the tip holder, with the threaded end facing out, and placed on the threads of the transducer. Before tightening the tip onto the transducer threads, it is necessary to first ensure that it is not cross-threaded by turning counter-clockwise until a slight click is felt. Next, holding the tip holder with two hands, the tip is slowly threaded into the transducer until a slight pressure is felt. During this step it is crucial not to apply pressure toward the transducer (the center pickup electrode in which the indenter is mounted to is extremely fragile) or over-tighten the indenter tip. When the indenter is properly installed onto the transducer, the tip holder is carefully removed.

B.2.4 Installing transducer and TriboScanner

For all nanoindentation experiments used in this study, a 1-D transducer was used capable of measuring the normal force and vertical displacement of the tip. The transducer is then installed onto the dovetail of the TriboScanner and the small hex screw located on the side of the transducer is tightened to firmly secure it in place. It is connected to the scanner by plugging the electrical cable from the transducer to the right 15-pin female socket located on the top of the TriboScanner. Before installing the TriboScanner, it is necessary to ensure that the Z-stage of the AFM is completely raised to allow for adequate clearance for the scanner. The TriboScanner is then installed in the dovetail groove of the main AFM system, and properly mounted by turning the screw, located to the right of the groove, counter-clockwise. The scanner is then connected to the Dimension® 3100 AFM system by plugging in the male electrical cable, coming from the top of the scanner between the two 15-pin female plugs, into the electronics box of the AFM system. Next, the male transducer controller cable is plugged into the left 15-pin female socket located on the top of the TriboScanner.

After all of the proper electrical connections have been established between the transducer, TriboScanner and the instrument electronics, the transducer controller is turned on. When the controller, shown schematically in Figure B.2, is turned on the green power indicator LED should illuminate and the LOAD (mg) LCD will initially display a value of -1 and the DISPLAY GAIN will need to be decreased to 1. With the equipment properly installed, the LOAD (mg) LCD should now show the reading of the load applied to the transducer due to the weight of the tip and be

approximately 266.1 mg. The other settings of the transducer controller are as follows: LOW PASS FILTER: 300 Hz, OUTPUT 1 GAIN - DISPLACEMENT: 1000, OUTPUT 2 GAIN - MICROSCOPE FEEDBACK: 1000 and DISPLAY GAIN: 10. After the initial LOAD value has been checked, the display is set to zero by first pressing AUTO ZERO and then using the FINE or COURSE MANUAL ZERO knobs to zero the load value in the LCD.

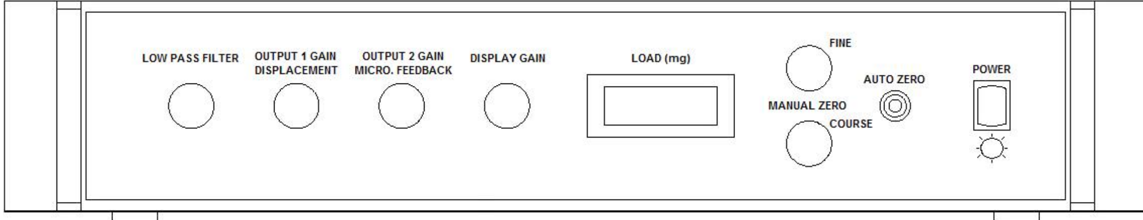

Figure B.2: Schematic of the front panel of the nanoindenter transducer controller. After Reference [154].

B.2.5 Locating the indenter tip in the Vision System

The tip is located within the AFM Vision System by using the **Focus Tip** command icon and the adjustment knobs located next to the optics to the left of the scanner. During this step it is necessary to adjust the illumination within the **Focus Tip** control box. The Vision System will show a side view of the indenter with the tip pointed to the right of the image. When the indenter tip is located in the Vision System window, the tip is focused using the trackball, with the bottom left button pressed, and the optical adjustment knobs are used to align the cross-hairs slightly to the right of the tip. *OK* is selected on the **Focus Tip** control box when finished.

B.2.6 Specimen placement

When the indenter has been located in the Vision System, the specimen is placed onto the instrument's vacuum chuck. Before doing so, ensure that the TriboScanner is raised high enough, using the trackball, to allow for proper clearance, and the vacuum chuck is clean and free of debris. The chuck can be cleaned with a lint-free cloth and alcohol if necessary. The specimen is placed directly onto the vacuum chuck and held in place by engaging the "Vacuum" toggle switch located on the main Electronics Box [151]. The stage and chuck are adjusted in the X and Y directions by using the **Focus Surface** command button and with the trackball to properly place the specimen under the indenter tip.

B.2.7 Manual approach

The AFM's Z-stage is then used to bring the tip closer toward the specimen surface. To perform this task, the secondary illumination switch located on top of the transducer control box is turned on, then the **Focus Surface** command icon is selected and using the trackball, with the bottom left button pressed, the tip is slowly moved down in the Z-direction until the secondary illumination becomes visible on the Vision System and the tip becomes visible via the AFM's optical system. While performing this step it is again absolutely necessary to simultaneously visually confirm indenter clearance with the specimen surface to avoid damaging the indenter tip. The manual approach is continued until a reflection of the indenter tip (tip pointed to the left) appears from the right side of the Vision System window. At this point the tip should be about less than 1 mm from the surface of the specimen and the approach is stopped. The Z-stage motion is deactivated by choosing *OK* on the **Focus Surface** control box and the secondary illumination is turned off.

B.2.8 Thermal equilibration

Once the tip is brought to roughly 1 mm from the specimen surface, the transducer controller and vacuum chuck are turned off and the thermal enclosure of the instrument is secured. The entire instrument and specimen are allowed to thermally equilibrate for 10-12 hours, typically overnight, before the experiments are begun.

B.3 Instrument and software set-up - Hysitron system

After the thermal equilibration period is complete, the thermal enclosure is opened, the vacuum chuck is turned on to secure the specimen and the enclosure temperature and humidity are recorded. This process should take approximately less than 10 seconds. Next, the transducer controller is turned back on and the LOAD LCD checked and zeroed. The secondary illumination is again turned on and the **Focus Surface** command icon is selected and the trackball is used to carefully bring the indenter tip to within less than 100 μm of the specimen surface. During this step, the indenter reflection on the right side of the vision screen will slowly approach the real image of the indenter to the left until it is a distance of about the width of the cross-hairs in the center of the screen. At this point, the tip is within the proper placement from the specimen surface and the remaining approach is controlled by the AFM system. The **Focus Surface** control box is then closed and the illumination turned off. The system is allowed to re-thermally equilibrate again for

about 1 hour to overcome the effects of opening the enclosure. During this waiting period, set-up of the Hysitron software necessary to begin the experiment is completed.

The Hysitron software is opened by selecting the desktop shortcut labeled *TriboScope3.5FL*, on the computer system to the left of the instrument, prompting the **Data Analysis** window to appear on the screen. The **Setup Indent** icon is selected to open the **Load Function** window. It is then necessary to check if the proper transducer constants file is installed which matches the transducer to be used for the experiments. This is done by selecting the **Set Transducer Constants** icon and confirming that the file name in the Transducer Constants box matches the serial number of the transducer installed on the instrument. The transducer constants used for the experiments performed in this study are given in Table B.6. See the TriboIndenter® User Manual [154] for more discussion on Transducer Constants.

Z-axis	
Load Scale Factor (mV/mg)	1.00
Displacement Scale Factor (mv/μm)	100
Electrostatic Force Constant (μN/V^2)	0.02800 - 0.03000
Machine Compliance (nm/mN)	1.50
Maximum Force (μN)	10296.00
Displacement Gain	1000

Table B.6: 1-D transducer constants

Prior to beginning each set of indentation experiments, while the indenter tip is still positioned less than 100 μm from the surface of the specimen, a procedure known as an air-indent is performed to properly adjust the Electrostatic Force Constant. To set up this procedure, the air-indent loading function is opened on the software by selecting **File** → **Open** and choosing the saved air-indent load function. The load pattern consists of a uniform 4 second loading up to a peak load of 20 μN followed by a 4 second unloading to zero load. The Spring Force Compensation is turned on, which corrects the forces resulting from deflection of the transducer's center pickup electrode [154]. This is done by selecting **Setup** → **Spring Force Compensation**. Also, 2,000 data points are specified for the loading pattern.

B.4 Performing the indentation

B.4.1 The air-indent

After the 1 hour period is complete, the load on the transducer controller is again zeroed, if necessary, and the first air-indent is completed. When finished, the .hys file is saved and the **Data Analysis** window again appears showing the Load versus Displacement data for the completed indentation. If the Electrostatic Force Constant is properly set, then the load-displacement data will appear as an increasing displacement at a constant zero load. If not, then the Electrostatic Force Constant is adjusted by selecting the **EDIT** icon and adjusting the Electrostatic Force Constant by increments of 0.00005 - 0.00010 μN/V^2 until the load-displacement curve maintains an increasing displacement at a constant zero load. When the new Electrostatic Force Constant is chosen, it is adjusted in the Transducer Constants box by selecting the **Set Transducer Constants** icon in the **Load Function** window. The transducer controller load is again zeroed, if necessary, and the procedure is repeated until the air-indent results in the proper load-displacement curve.

Once the air-indent procedure has been completed the load pattern is changed to that shown in Figure 3.1. The number of data points are changed to 8,000 and the desired load is adjusted. Also, the software is set up to measure the thermal drift rate over a 5 second interval and confirm that it is less than 0.1 nm/s. If a higher drift rate is detected, the system will re-measure the thermal drift rate over repeated 5 second intervals until it is less than the user specified 0.1 nm/s. The drift rate is specified by selecting **Setup** → **Drift Correction** and *Turn On* is checked.

B.4.2 The preliminary surface scan

Prior to beginning the indentation, the TriboScanner, in conjunction with the AFM system, is used to perform a preliminary scan of the surface. This is done by re-zeroing the transducer controller load and selecting the **Engage** command icon within the AFM software at which time the instrument automatically lowers the TriboScanner to the specimen surface and begins scanning with the indenter tip once the surface is detected by the transducer. When the scanning begins, the scan size is changed to 1 μm and the **Scope Mode** command icon is selected and the **Scope Trace** is used to confirm if the tip is tracking properly. During scanning, the center pickup electrode of the transducer is adjusted to properly center it between the two outer drive plates by choosing **Motor** → **Step Motor** and selecting **Tip Down** button to slowly raise the pickup electrode, in 0.139 μm increments, until the Voltage shown in the **Scope Trace** window decreases to between -15 V to + 15 V. After a

full scan is complete and the surface quality is confirmed, the Scan Size, Integral and Proportional Gains are all set to zero causing the scanner to disengage and allow the Hysitron system to gain control of the instrument.

B.4.3 The indentation

When the Scan Size, Integral and Proportional Gains have been set to zero, the **Manual Indent** icon is selected in the **Load Function** window of the Hysitron system. At this point, the instrument applies the specified load function and performs the indentation. When the indentation is complete, the tip is secured on the AFM system by selecting the **Withdraw** command icon, within the AFM software, to automatically withdraw the indenter and secure the scanner. The Integral and Proportional gains are then set back to 2.00 and 3.00, respectively, and the specimen stage is moved 50 μm in the X-direction to the location for the next indent. The indentation .hys file is then saved.

B.4.4 Analysis of the results

Once the indentation data has been saved on the Hysitron computer, the load-displacement curve will automatically open in the **Data Analysis** window. The measured hardness H, reduced elastic modulus E_r, contact depth h_c and material stiffness S can then be obtained from the curve using the Hysitron software. For the experiments used in this study, the measured load versus displacement data were instead analyzed using the computer program, Indentation Data Analyzer (IDA), developed by M. Klopfstein [86]. This software has the advantage over the instrument's in that it allows the user the option to determine the thermal drift rate from the hold period at 10% of max load and to use this value to correct the measured data. Additionally, it incorporates correction factors to the procedure developed by Oliver and Pharr [77]. See the IDA Help file [86] for more specific information on these correction factors.

In the **Data analysis** window, the necessary steps are taken to export the data for analysis in the IDA program. First, the Drift Correction is turned off by selecting the **Edit** icon and de-selecting *Drift Correction* under **Current Parameters** within the **File Calibration Constants** window and then selecting *OK*. The data is then exported as a .txt file under the same filename by selecting the **Export Tab Delimited Text** icon in the **Data Analysis** window. The Drift Correction is then turned back under on under **Current Parameters** within the **File Calibration Constants** window.

Next, the IDA software is opened by selecting the desktop shortcut labeled *Indentation Data*

Analyzer(IDA) on the same computer system. Within the main software window, 0.00 is entered for the *Frame Compliance Cf* and the *Upper and Lower Fits* are set at 95% and 20%, respectively, as they are in the Hysitron software. The Upper and Lower Fits correspond to the portions of the unloading curve that will be analyzed. Additionally, the Berkovitch B5 indenter, used for all experiments, is selected under *Indenter*. The Advance Parameters are then specified by selecting **File → Setup More Parameters**. In the **Advance Parameters** window, if the material's Poisson's ratio is known (as in the case of the pure Au specimens) then *Gamma Correction* can be applied with the known Poisson's ratio specified. The boxes labeled *Compute drift rate* and *Calculate creep rate* are selected which will prompt the software to determine the respective values from the exported Hysitron experimental data. The drift rate was determined during the last 40 seconds of the hold period at 10% of the peak load, i.e., start (sec) = 125 and end (sec) = 165. The end time of the drift rate calculation is 5 seconds after the end of the hold period specified in the load function. This is to correct for a lag time of approximately 5 seconds added by the Hysitron software to the experimental data. All other default software functions are left unchanged. See the IDA Help file [86] for more specific information on the Advanced Parameters used in this software. Next, the load profile shown in Figure 3.1 is chosen by selecting **File → Select Loading Profile → Five segment loading**. The correct times for each segment are also specified for the five segment load profile. The exported data from the Hysitron software is then chosen as the Input File by selecting **File → Open** and choosing the appropriate input file. The output file is specified by selecting **File → Select output file name** and choosing an existing file to overwrite or writing the new output file name in the box labeled "Filename:". The data analysis is then completed by selecting **Analyze**. After the software has completed the data analysis, the calculated values are displayed on the right side of the main screen and the results are summarized in the box in the bottom right corner.

At this time, the procedures described in Sections B.4.2, B.4.3 and B.4.4 are repeated and a total of five indentations are completed at each chosen contact depth.

Appendix C

Procedure for measuring the thin film resistivity using the Four-Point Probe method

This chapter describes the procedure performed during a set of resistivity measurements using the four-point resistivity probe instrument (FPP-5000 manufactured by Veeco, Inc.) including the initial setup and performing the measurement. The operating procedures have been adapted from the FPP-5000 Four Point Resistivity Probe: Installation, Operation and Manual [87].

C.1 Initial setup

Before beginning the measurements, the instrument's platen is adjusted to ensure that the probes are at the proper distance from the specimen. To adjust the platen, the circular adjustment tool is placed onto the platen so that it is located over the probe pins and the platen aperture, as shown in Figure C.1. Next, the platen is pressed down until it reaches the stop and the adjustment screw, located at the front/center of the platen, is turned either clockwise or counterclockwise to lower or raise the platen, respectively. The adjustment is performed only until the outer probe pin makes contact with the underside of the adjustment tool.

Next, the instrument is turned on by toggling the power switch located on the left rear of the instrument. The film thickness is first stored in the instrument by pressing **SLICE**, **PGRM**, entering the thickness of the film in either units of mils or μm (the default unit is mils), pressing

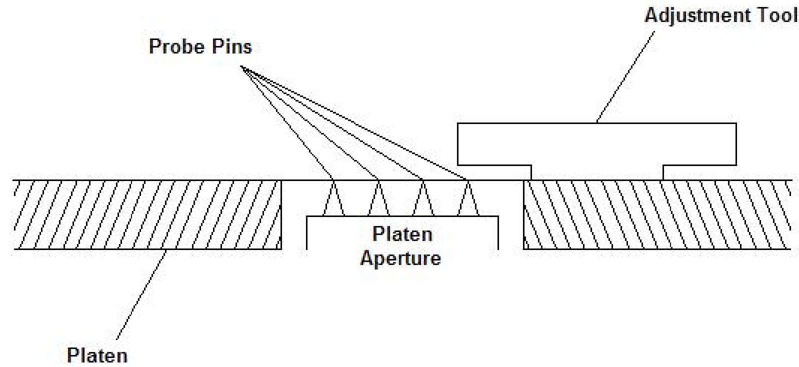

Figure C.1: Schematic showing the proper placement of the platen adjustment tool. After Reference [87].

the **STORE** button and again **PGRM** to exit. The geometric correction factor (if needed) is then stored by pressing **SHEET**, **PGRM**, entering the appropriate geometric correction factor, pressing the **STORE** button and again **PRGM** to exit. The **SLICE** button is then pressed to set the instrument in the proper mode to perform a resistivity measurement.

The instrument uses a standard 3 in. wafer holder in which to secure the specimen during measurements. All specimens used in this study were cleaved to various sizes and therefore it was necessary to mount them onto standard Si wafers using double-stick tape. The specimen and wafer are placed face down onto the black plastic wafer holder and the backing plate is placed on top with the rubber, spiral side facing down. The backing plate is divided into four quadrants labeled '2' - '5' which are used to center the wafer holder on the platen. The entire assembly is carefully placed onto the instrument platen and with the quadrant arm labeled '2' facing down, the horizontal quadrant arms labeled '3' and '5' are lined up with the white horizontal marker lines on either side of the platen. This ensures that the specimen is properly centered over the probe pins.

C.2 Performing the measurement

To measure the resistivity, the top cover is slowly closed onto the backing plate which will cause the platen to lower until the specimen makes contact with the probe pins. When contact is established, the instrument will click and the test will begin at which time the electronic display will go blank and the TEST indicator next to the display will illuminate for approximately 2 seconds. When the measurement is completed, the TEST indicator will darken and the display will read the measured resistivity. The cover is then opened and the wafer holder and backing plate are rotated until the

quadrant arm labeled ‘3’ is facing down and ‘2’ and ‘4’ are horizontal. The procedure is then repeated until the wafer holder and backing plate have rotated 360° for a total of four measurements.

VITA

Benjamin Michael Dvorak

Candidate for the Degree of

Master of Science

Thesis: INVESTIGATION OF THE NEAR SURFACE MECHANICAL PROPERTIES OF Au-Si THIN FILMS

Major Field: Mechanical Engineering

Biographical:

Personal Data: Born in Arlington, TX, USA on February 10, 1983. The son of Robert and Connie Dvorak and brother to Matthew Dvorak. Happily married to Gena Elizabeth Holt on May 22, 2005. The soon to be proud father of Sophia Claire Dvorak, born August, 2008.

Education: Graduated from Union High School, Tulsa, Oklahoma in May, 2001. Received the Bachelor of Science degree in Mechanical Engineering from Oklahoma State University, Stillwater, Oklahoma in May, 2006. Completed the requirements for the degree of Master of Science with a major in Mechanical Engineering at Oklahoma State University in July, 2008.

Experience: Graduate Research Assistant, Oklahoma State University, May 2006 - July 2008; Graduate Teaching Assistant, Oklahoma State University, August 2006 - May 2008; Undergraduate Research Assistant, Oklahoma State University, August 2004 - May 2006; Participant in the National Science Foundation Research Experience for Undergraduates Program, Oklahoma State University, Summer 2005.

Professional Memberships: American Society of Mechanical Engineers; The Honor Society of Phi Kappa Phi; Pi Tau Sigma Mechanical Engineering Honor Society; National Society of Collegiate Scholars.

Name: Benjamin Michael Dvorak Date of Degree: July, 2008

Institution: Oklahoma State University Location: Stillwater, Oklahoma

Title of Study: INVESTIGATION OF THE NEAR SURFACE MECHANICAL PROPERTIES OF Au-Si THIN FILMS

Pages in Study: 104 Candidate for the Degree of Master of Science

Major Field: Mechanical Engineering

An investigation of the material properties of polycrystalline Au films and the effect of Si content on the material properties and structure of co-evaporated Au-Si films has been performed. Atomic Force Microscopy (AFM), nanoindentation and four-point probe were utilized to investigate the surface topography, mechanical and electrical properties of these films, respectively. X-ray Diffraction (XRD) and Transmission Electron Microscopy (TEM) measurements were performed to investigate the material crystallography and structure.

The hardness of pure Au films was found to be approximately 1.2 GPa and increased by about 40 - 80% (1.64 GPa - 2.13 GPa) by the addition of 2.5 and 6 at. % Si, respectively and approximately 102% to 2.41 GPa by the addition of 21 at. % Si. The film resistivity increased nearly linearly from 5.58 - 38.15 $\mu\Omega$-cm as the Si content increased from 2.5 - 21 at. %, respectively.

XRD measurements on the Au/21 at. % Si film suggested the formation of an unknown crystalline Au-Si phase. The metastability of this phase was shown experimentally by performing a second XRD measurement on the same specimen after an 8 week room temperature storage period which indicated that the unknown Au-Si surface phase present had almost completely dissociated. The hardness and reduced elastic modulus decreased by approximately 32% from 2.41 - 1.65 GPa and 53% from 88 - 41.5 GPa, respectively.

TEM measurements, conducted on an Au/25 at. % Si specimen, showed the nanocrystalline grain structure of the Au, with an average grain size of 18 nm (consistent with the XRD measurement), with a dispersion of amorphous Si particles approximately 1 - 5 nm in diameter. From these results, the predicted hardness increase of the Au-Si film resulting from the Orowan hardening mechanism was estimated to be $H_{Orowan} \approx$ 0.05 GPa - 1.07 GPa representing approximately 4 - 88% of the overall hardness increase measured for the Au/21 at. % Si film assuming the same Si content for the TEM specimens. The estimated H_{Orowan} range suggested that additional mechanisms, such as the Hall-Petch effect, may be responsible for the measured hardness increase.

ADVISER'S APPROVAL: Don A. Lucca